Universidad de Antioquia
Facultad de Ciencias Exactas y Naturales
Instituto de Física

The late Integrated Sachs-Wolfe effect and its Detectability in Galaxy-redshift Surveys

David Ricardo Valencia-Díaz
Facultad de Ciencias Exactas y Naturales
Instituto de Física

Advisor: Juan Carlos Muñoz-Cuartas

UNIVERSIDAD DE ANTIOQUIA
FACULTAD DE CIENCIAS EXACTAS Y NATURALES
INSTITUTO DE FÍSICA

THE LATE INTEGRATED SACHS-WOLFE EFFECT AND ITS DETECTABILITY IN GALAXY-REDSHIFT SURVEYS

David Ricardo Valencia-Díaz
Facultad de Ciencias Exactas y Naturales
Instituto de Física
Advisor: Juan Carlos Muñoz-Cuartas

Medellín, 2017

The late Integrated Sachs-Wolfe effect and its Detectability in Galaxy-redshift Surveys
Author: David Ricardo Valencia Díaz
Advisor: Juan Carlos Muñoz Cuartas

Printed in Medellín, Colombia
First edition, 2017

To my family: my mother, my sister and my girlfriend, who have been always by my side

Abstract

The Cosmic Microwave Background (CMB) is a microwave radiation field that permeates the Universe. In principle, this radiation should be homogeneous, but due to several physical processes, the CMB photons underwent perturbations that induced the formation of several anisotropies. The study of some of those CMB anisotropies may lead to evidence of the existence of the dark energy, which is associated with the current accelerated expansion of the Universe. In that context, one of those CMB anisotropies is the late Integrated Sachs-Wolfe (ISW) effect. The ISW is an effect that the CMB photons experience when they pass through non-stationary overdense or underdense regions, changing their wavelength and energies. Such perturbation in the CMB is associated to the evolution in time of the gravitational potential wells of dark matter structures that form the Large Scale Structures (LSS) and host the galaxies.

The first aim of this thesis is to study the late ISW effect in cosmological simulations in order to find constrains in the temperatures of the maps of anisotropies due to this late ISW effect, to analyse the mean behaviour of the temperature fluctuations along the lines of sight and of the cross-correlation functions and correlation-power spectrum. Three different simulations were used in the first part of this work: a small cubical simulation box of $400\ h^{-1}$Mpc and two simulations from the MultiDark project: the MultiDark 1 (MDR1) and the MultiDark-Planck (MDPL) simulation. The small simulation and the MDR1 simulation are associated to a ΛCDM -WMAP universe and the MDPL simulation is associated with a ΛCDM -Planck universe.

The second aim of this thesis is to study the ISW effect induced by the density field from a redshift galaxy survey such as the Two Micron All-Sky Survey (2MASS) and compare this signal with the theoretical expectation studied before. We use the 2MASS Final Release and a Halo-Based Method to infer the underlying dark matter density field that host the galaxies of such a survey.

This method is implemented thanks to its independence from a galaxy bias. Once the ISW estimation due to the 2MASS density field is found, comparisons between this signal and CMB observations are performed. The 9th year WMAP ILC map and the Planck SMICA map are used to study the angular cross-correlation function and correlation-power spectrum between those CMB surveys and our ISW estimation. The resolutions used allow us also to study briefly the contribution of the Rees-Sciama effect.

Finally, a brief analysis of the influence in the estimation of the time derivative of the gravitational potential is performed. As this field may be computed using an exact solution based on the peculiar velocities or a linear approximation based on the linear growth of structures, we study the effects of those approaches in the angular power spectrum.

The numerical and computational methods used to study the late Integrated Sachs-Wolfe effect in this work are based in the Fourier transform of different fields, as the density field, the gravitational potential field and its corresponding time derivative, and the interpolation and numerical integration of the time derivative of the gravitational potential $\dot{\Phi}(\mathbf{x})$. The methods used to calculate the different fields mentioned above and the maps obtained after the data processing are shown, as well as the maps of the late ISW anisotropy from the simulation boxes and from the data infered from observations.

Although the results obtained in this work using numerical cosmological simulations are consistent with the theoretical analyses [13] and an ISW signal is clearly resolved, the results we obtained with the density field infered from observations do not allow to reassert for a detection of the ISW signal, because it is too small. This issue may be due to the galaxy survey used, because this survey only allows to know information of a very local region of the Universe; so a larger survey must be used in order to find a higher signal due to more structures. In spite of this, the methods used in this work show very good and consistent results, and one of the outlooks is to use a larger galaxy survey to estimate the actual ISW contribution of the structures in our Universe.

Acknowledgments

No matter how much time you spend in science research, you will always feel it is not enough. Sometimes it tastes good, but many times it also tastes bitter. But the effort has, in any way, a reward. After these years of hard and interesting work, I first want to thank to my family: my motherCarmen Díaz Osorio, my sister Clara Isabel Valencia Díaz and my girlfriend María Alejandra Urrego Cañas, by all their support, the encouragment words and advices to overcome my own mental obstacles and keep going forward. They are my reason to continue and they are whom this work is dedicated.

My advisor also deserves my gratitude, because in spite of the large number of commitments he had, he was always ready to listen, to support and to share his knowledge with me. Even to deposit trust on me to do a research internship with this work.

Respect to this research intership, I want to thank to Colciencias, by the economical support for the first year of this project through the Joven Investigador internship number JIC-111-2014 from the 2014 announcement.

Finally, I want to thank to all the people that in one way or another have helped me in the development of this thesis: by the support, the advices not only in the technical issues of sciences but also as in the human side. I want to highlight the help from Óscar Nicolás Gómez Giraldo and from Nataly Mateus Londoño, because all the time we have shared through this Master program, learning and sharing programming skills, topics on cosmology and all the work and feedback we have done together, and without which this path would have been even harder.

Sincerely,

David Ricardo Valencia Díaz 2017

Contents

List of Figures

List of Tables

Introduction

Nowadays, the cosmological model accepted as the standard is the Λ-Cold Dark Matter (ΛCDM) cosmological model. It has been proposed as a model that fits with cosmological observations and allow them to be explained in the framework of the general relativity. In this cosmological model, the Universe is considered as homogeneous and isotropic (concepts summarized in the so-called cosmological principle) and it is composed of baryonic matter, dark matter, radiation and dark energy. The dark energy is, nowadays, the dominant component in our Universe [7].

Based on the observations of the Cosmic Microwave Background Radiation and those of the recession velocity of the galaxies, the accepted origin of the Universe is a singularity with a subsecuent expansion of the space-time metric of the Universe, called The Big Bang. After this space-time metric expansion, vacuum quantum fluctuations occured from which large amounts of matter and anti-matter were created. Both parts annihilated creating photons, and due to the large amount of energy and high temperatures, matter (such as protons, electrons, and so on) and radiation were tightly coupled. With the expansion of the Universe, the temperature decreases and matter and radiation were able to decouple, allowing radiation to travel free in the Universe, filling it completely in an isotropical way. This isotropic radiation field contains a lot of information about the initial conditions of the Universe at the time were matter and radiation decoupled [7].

Although initially this thermal bath, called Cosmic Microwave Background (CMB), was isotropic in the whole Universe, it underwent perturbations in its spatial distribution due to effects as the Baryonic Accoustic Oscillations (BAO) before the *surface of last scattering*, generating what is known as the primordial anisotropies in the CMB. Those anisotropies are temperature fluctuations in the CMB that deviate from the mean temperature of a black-body that the CMB photons must have. Furthermore, this *surface of last scattering* is considered as the set of points in the space at a certain distance, such that today we receive the photons from the CMB that were scattered by the last time at decoupling epoch [7].

Apart from this primordial anisotropies in the CMB generated before and in the surface of last scattering, there exist another kind of anisotropies. Time after some important phenomena occured in the Universe such as the inflationary epoch, the decoupling time and the collapse of dark matter, then the first protogalaxies and galaxies were formed inside dark matter haloes. With the formation of those objects, the Large-Scale Structures (LSS) that we observe in the Universe began to take shape. Photons from CMB began to undergo perturbations due to the interaction with such matter structures, generating the late anisotropies of the CMB. Those late anisotropies have a lower signal amplitude when compared with the amplitud of the primordial ones, making the late anisotropies more difficult to be detected [10].

In the study of the CMB anisotropies it is possible to find evidences that allow to study the nature of the cosmological constant [2], [16]. This cosmological constant is introduced in Einstein's field equations, and observations of the accelerated expansion of the Universe fit very well with this model. In the ΛCDM cosmological model, the cosmological constant is associated with the Dark Energy (DE).

One of late anisotropies of the CMB is due to the late Integrated Sachs-Wolfe (ISW) Effect. This is an effect that CMB photons underwent when they pass through overdense regions (associated with the LSS) or underdense regions (also called voids), generating a change in the wavelength and in the energy of those photons. Those perturbations in the CMB are due to to temporal evolution of the gravitational potential wells of Dark Matter that form the LSS and host the galaxies. This time evolution may be associated to the accelerated expansion of the Universe, due to the presence of Dark Energy. The ISW effect, as a late anisotropy, has a lower signal than the primordial anisotropies, making it also difficult to be detected [10].

To date, authors have tried to detect the ISW effect when searching correlations between the CMB maps and the matter density field maps in the Universe, which are related with the local gravitational potential wells. As the primordial anisotropies are not correlated with the matter density field at the present time, it is possible to find the weak correlations associated to the late ISW and the density field [10]. Works from diverse groups of authors have tried to find such correlations between CMB maps and matter density field maps, with detection significances between 2-3σ [5], [10], using the data from the Wilkinson Microwave Anisotropy Probe (WMAP) survey and samples of galaxy surveys such as the Sloan Digital Sky Survey (SDSS). Results found by those authors are consistent with the standard cosmological model, in spite of its low significance [27]. Furthermore, using techniques to obtain 3-dimensional projections of the density field, instead of the 2-dimensional density profiles, it has been achieved a significance of around 4.4σ in the detection, being the largest significance related with the ISW effect found until now [12]. Even in a recent study, the same group of authors using data from the same SDSS survey have shown that there is no evidence of cold or hot spots in the scale of degrees, associated with large structure as supervoids or superclusters; although they found, based on simulations, that the measurement of the ISW effect is a factor of ~ 2.1 above the expected measurement in a ΛCDM universe [13]. On the other hand, some authors have found anticorrelations between the CMB maps (from WMAP survey) and a catalogue with more than 1.5 million galaxies from the SDSS, rejecting the ΛCDM model [32]. Other authors have even rejected the hypothesis of the existence of the late ISW effect, when using photometric measurements in galaxy-redshift surveys such as the Two Micron All-Sky Survey (2MASS) [9].

By those exposed reasons, the detectability of the ISW effect has been a great challenge, because even the same group of authors using the same data set have obtained different and somewhat contradictory results. Besides and in general, there is no full criterion about the detection of the ISW effect. Even when comparing the ISW effect signal from observations with the expected values from ΛCDM model using mock catalogues, the obtained analysis from observational data show a signal above the expected value. In our case, we found a somewhat opposite results, because the possible detection from our observational data sample is below the theoretical expectation we computed from cosmological simulations. These fact leads to more confusion in the topic of the ISW detection.

A possible explanation about such systematic errors is the so-called *galaxy bias*. This *galaxy bias* in an observational sample is obtained when comparing the clustering of observed galaxies with the clustering of dark matter. The dark matter's clustering is inferred from cosmological simulations and depends on the cosmological model that was used [21], becoming the *galaxy bias* in an important parameter in the model and in turn, of great importance in the detection of the ISW effect.

Since direct observation of small anisotropies in the CMB temperature due to the ISW effect is so complicated, the search of this effect has been concentrated, as mentioned before, in find correlations between CMB temperature maps and matter density field maps, which account from the local gravitational potential fields. With the purpose of perform such a study, it is necessary to understand basic concepts such as the standard cosmological model, the CMB and its anisotropies and the formation of the LSS.In this work we focus on the aformentioned problems about the existence of the ISW effect, its detectability from observational data and we treat the question about the inconsistencies in the ISW signal amplitude between theoretical ΛCDM expectation and the signal that may be obtained from observations. Those three problems will be boarded while asking some questions:

- The largest structures in our Universe are considered to evolve in a linear way. Is this linear approximation in a ΛCDM universe responsible of the temperature fluctuation associated to the ISW effect? Or should it be necessary to use a more detailed and exact model of the evolution of such largest structures?
- In computational cosmology it is necessary to use the concept of Mass-Assignment Schemes (MAS) in order to smooth the dark-matter density fields and interpolate their values on a grid. May the use of a MAS in cosmological simulations have a kind of spurious contribution in the estimated temperature fluctuation associated with ISW effect?
- Is it indeed possible to find an ISW signal in a ΛCDM universe?
- The small-scale analogous of the ISW effect is the so called Rees-Sciama effect, in which photons would be perturbed due to local and small gravitational potential wells. So, is it possible to detect the ISW and Rees-Sciama effects in galaxy redshift surveys as 2MASS when cross-correlating with CMB maps?

This work is organized in the following way. In chapter 1, the theoretical basis to understand the origin of the ISW effect are exposed. The chapter 2 is comprised by a study focused on the description of our work methods and their application on cosmological simulations. As the density field is the base field of our work, a MAS will be used to estimate this field and then, compute other important fields such as the gravitational potential and its time derivative. Furthermore, the linearity or non-linearity on the evolution of the structures are also taken into account in this chapter in order to conclude about the existence of a temperature fluctuation due to ISW in ΛCDM universes. In chapter 3, we show the estimation of the ISW effect using the fields obtained in chapter 2 as raw material. Again, the linear and non-linear models for the structure evolution will play an important role in the answering of the previous questions, alongside with the possible effects that mass-assignment schemes would have on the estimation of this effect. In chapter 4, we describe the method used to infer the underlying dark-matter density field from 2MASS galaxy survey. As in observations of LSS it is mandatory to assume a linear evolution of structures, we study the ISW contribution from this 2MASS density field constrained to this approximation. In this chapter, cross-correlations and angular power spectra between the 2MASS-induced ISW effect and CMB surveys such as WMAP and

Planck are analysed. In chapter 5 the discussion about the linearity and non-linearity is boarded again. Some analysis about the effect of each approximation and the comparison with observational CMB surveys through angular power spectra are perfomed in this chapter. Finally, chapter 6 contains a summary of the main results through a brief discussion in order to draw conclusions of the present work.

CHAPTER

1

Theoretical Framework

This chapter will describe the theoretical framework in which the origin of the late Integrated Sachs-Wolfe effect is based. A brief introduction about the standard ΛCDM cosmological model and the formation of structures will be discussed first. Then, a more deep description on the Cosmic Microwave Background Radiation and its anisotropies in the concordance model will be studied, alongside with the late ISW effect.

1.1 Cosmological Context and ΛCDM Cosmological Model

Nowadays, the accepted as standard cosmological model is the Λ-Cold Dark Matter cosmological model also known as ΛCDM standard model. In this model, the Universe is composed of radiation, baryonic matter, Dark Matter (DM) and Dark Energy (DE). At present, such dark energy dominates over the other components and governs the dynamics of the Universe [7], [23]. DE is also associated to the cosmological constant of the Einstein's field equations and is interpreted as an entity with constant energy density which composes the major contribution to the total energy density of the Universe. Moreover, observations of the structure at larger scales in our Universe fit very well to a cosmological model of the Universe that includes such cosmological constant.

The current cosmological model is justified in the observations that show an homogeneous and isotropic universe at large scales, with a flat geometry and which dynamics is ruled by the relation that exists between the components of the Universe [7], [23].

In general, an homogeneous and isotropic universe is well described by a Friedmann-Lemaître-Robertson-Walker (FLRW) metric [7]:

$$\mathrm{d}s^2 = -c^2\mathrm{d}t^2 + a^2(t)\left(\frac{\mathrm{d}x^2}{1-k\,x^2} + x^2\mathrm{d}\theta^2 + x^2\sin^2\theta\mathrm{d}\phi^2\right), \tag{1.1}$$

where $a(t)$ is the scale factor that accounts for the expansion of the Universe, while x is the comoving position, i.e. the position on a coordinate system that moves with the Hubble flow. The dynamics of such Universe is studied through the Friedmann equations, which are obtained from this metric and the Einstein's equations:

$$\frac{\dot{a}^2 + kc^2}{a^2} = \frac{8\pi G\rho + \Lambda c^2}{3}, \tag{1.2}$$

$$\frac{\ddot{a}}{a} = -\frac{4\pi G}{3}\left(\rho + \frac{3P}{c^2} + \frac{\Lambda c^2}{3}\right). \tag{1.3}$$

The first equation may be rewritten as

$$\frac{H^2}{H_0^2} = \Omega_r a^{-4} + \Omega_m a^{-3} + \Omega_k a^{-2} + \Omega_\Lambda, \tag{1.4}$$

where $H(t) = \dot{a}/a$ is the Hubble parameter and each Ω_i as the density parameter associated with each of the constituents of the Universe that contribute to the stress-energy tensor: radiation $(i = r)$, matter $(i = m)$, space-time curvature $(i = k)$, and cosmological constant $(i = \Lambda)$. These density parameters allow to relate the density of each constituent at a certain time t with the critical density of the universe at the same time, i.e., $\Omega_i = \rho_i(t)/\rho_c(t)$ with $\rho_c(t) = \frac{3H^2(t)}{8\pi G}$. Those equations could be considered as the basis of cosmology.

1.2 Formation of Structures

The ΛCDM model assumes that the structures we observe today in the Universe grew from perturbations in the density field in a hierarchical way, i.e. that the first structures to be formed were the small ones and through gravitational interactions and mergers of these small structures, the bigger ones were formed [26]. In general, it is possible to define a density contrast function, that allows to measure the density of matter $\rho(x)$ in a certain position relative to the mean density $\overline{\rho}$ of the whole Universe:

$$\delta(x) = \frac{\rho(x) - \overline{\rho}}{\overline{\rho}}. \tag{1.5}$$

The Large-Scale Structures (LSS) come from overdensities in the dark matter's density field, generated by primordial fluctuations in such field allowing the formation of the gravitational potential wells called dark matter haloes. In those haloes, baryonic matter collapses gravitationally and the first stars and protogalaxies may be formed. Those objects evolve through collisions in a hierarchical formation scenario to form larger structures [26], [23]. The evolution of the density field (measured from the density contrast) can be obtained from the equation of conservation of mass, the Euler's equation and the Poisson's equation [23]:

$$\frac{\mathrm{d}\rho(\mathbf{r},t)}{\mathrm{d}t} + \nabla \cdot [\rho(\mathbf{r},t)\mathbf{v}] = 0, \tag{1.6}$$

$$\frac{\mathrm{d}\mathbf{v}}{\mathrm{d}t} + (\mathbf{v} \cdot \nabla)\,\mathbf{v} = -\frac{\nabla P}{\rho} - \nabla\Phi, \tag{1.7}$$

$$\nabla^2\Phi = 4\pi G\rho, \tag{1.8}$$

where Equation 1.6 is the continuity equation, in which ρ represents the density in a certain point $\mathbf{r}$, and $\mathbf{v}$ is the peculiar velocity of the density distribution at this point. Equation 1.7 is the Euler's equation for the motion of an element of a fluid; here P is the pressure and Φ is the gravitational potential. Finally, Equation 1.8 is the gravitational Poisson's equation.

Manipulating those equations in a perturbative approach using Equation 1.5 and assuming that perturbations are linear while using comoving coordinates (i.e., passing from physical coordinates $\mathbf{r}$ to comoving ones with the relation $\mathbf{r} = a\mathbf{x}$), it is possible to obtain the following set of equations:

$$\frac{\mathrm{d}\delta}{\mathrm{d}t} = -\frac{1}{a}\nabla \cdot \delta\mathbf{u}, \tag{1.9}$$

$$\frac{\mathrm{d}\mathbf{u}}{\mathrm{d}t} + \frac{\dot{a}}{a} = -\frac{\nabla\delta P}{a\overline{\rho}} - \frac{1}{a}\nabla\delta\Phi, \tag{1.10}$$

$$\nabla^2\delta\Phi = 4\pi G a^2 \delta\overline{\rho}, \tag{1.11}$$

where Equation 1.9 is the perturbed continuity equation in which δ is the density contrast from Equation 1.5 and $\mathbf{u}$ is the perturbed peculiar velocity. Equation 1.10 is the perturbed Euler's equation, in which $\overline{\rho}$ is the unperturbed density. Equation 1.11 is the perturbed Poisson's equation with $\delta\Phi$ as the perturbation in the gravitational potential. It is worth to remember that those last three equations are described in a background space-time that is expanding, but as they are in a comoving coordinate system, this expansion does not affect the coordinates theirselves; the expansion is described in the scale factor a. With those last three equations, it is possible to find a general equation that describes the time evolution of the density contrast:

$$\frac{\mathrm{d}^2\delta}{\mathrm{d}t^2} + 2\left(\frac{\dot{a}}{a}\right)\frac{\mathrm{d}\delta}{\mathrm{d}t} - 4\pi G\overline{\rho}\delta = 0. \tag{1.12}$$

Solving this equation, it is possible to find the growth and decaying rates of the density fluctuation. In general, the decaying rate has a negligible conribution to the growth of structures, so we only concern about the growth rate $D(a)$:

$$D(a) = \frac{5}{2}\left(\frac{\Omega_{m,0}}{\Omega_{\Lambda,0}}\right)^{1/3}\frac{\sqrt{1+y^3}}{y^{3/2}}\int_0^y \frac{y'^{3/2}}{[1+y'^3]^{3/2}}\,\mathrm{d}y', \tag{1.13}$$

$$y \equiv a\left(\frac{\Omega_{\Lambda,0}}{\Omega_{m,0}}\right)^{1/3}, \tag{1.14}$$

with $\Omega_{m,0}$ and $\Omega_{\Lambda,0}$ the density parameters corresponding to matter and to the cosmological constant, respectively, and evaluated at present time. The growth rate $D(a)$ is used to define the linear regime for the growth of structures, valid at large scales.

1.3 Cosmic Microwave Background and its Anisotropies

In 1964 the engineers Arno Penzias and Robert Wilson, worked at the Bell Laboratories in Holdmdel, New Jersey, with a radiometer used to comunicate with the Telstar satellite. In their work, they found a hiss in the signal that came from all directions, and deducted that this interference was produced by a Black-Body radiation field with a temperature near to the 3 K. This Black-Body radiation that filled completely the Universe, was in the region of the microwaves of the electromagnetic spectrum, with a peak wavelength of $\lambda_{\text{max}} = 1.06$ mm and it is known as the Cosmic Microwave Background Radiation (CMBR or simply CMB). Nowadays it is known that the peak temperature in the spectrum of this black-body radiation is near to 2.72548 ± 0.00057 K [7], and has been measured with high precision by surveys such as COBE, WMAP and more recently, Planck.

This radiation field is isotropic in the whole Universe, but due to effects such as the movement of the observers or the presence of matter in the Universe, this radiation may present anisotropies. The first kind of anisotropies are the so-called primordial anisotropies, which are effects produced before the *surface last scattering*, such as the Baryonic Acoustic Oscillations (BAO). Those primordial anisotropies were developed in the first moments of the history of the Universe, i.e. at high redshift, z.

The other type of anisotropies are the late anisotropies, induced as the photons propagate through the Universe and interact with matter [33]. One of such anisotropies is the Doppler effect due to the peculiar velocity that each observer has with respect to the Hubble flow (see middle panel of Figure 1.1). This anisotropy causes that an observer measures a lower temperature if looks backwards (in the opposite direction of its velocity) and a higher temperature if looks forwards (in the same direction as its velocity) [7].

Other late anisotropies have a much lower amplitude than the primordial anisotropies in the CMB spectrum. Some of them are the Sunyaev-Zel'dovich effect. This effect is related with the inverse Compton effect when photons of the CMB pass through regions of ionized hot intracluster gas, which allows the high energies of the electrons of the gas to be transferred to the photons, increasing the energy and temperature of photons. With this effect, the black-body spectrum of the CMB changes its shape, moving towards higher frequencies, generating a change in the temperature with respect to the mean CMB temperature [7]

The late Integrated Sachs-Wolfe effect (ISW) is another late anisotropy, produced by the gravitational redshift of the photons when they pass through the gravitational potential wells that evolve with time. In the case in which matter dominates the Universe, the gravitational potential wells will not evolve in time; but due to the presence of a cosmological constant (or even by the same space-time curvature) the potential wells will present a time evolution, generating a gravitational redshift fluctuation in the CMB temperature at low redshift [31]. The late ISW effect occurs mainly at $z < 2$ when photons pass through overdense or underdense regions, changing its energy and its temperature. The temperature fluctuation $\Delta T(\hat{\mathbf{n}})$ along the direction $\hat{\mathbf{n}}$ can be written as an integral of the time derivative of the gravitational potential $\dot{\Phi}$, from the surface of last scattering to the present time [31]:

$$\Delta T(\hat{\mathbf{n}}) = \frac{2}{c^2}\overline{T}_0 \int_{t_0}^{t_L} \dot{\Phi}(t, \hat{\mathbf{n}})\mathrm{d}t, \tag{1.15}$$

where t is the cosmic time, t_L is the age of the Universe at the surface of last scattering, t_0 is the present age of the Universe, $\dot{\Phi}$ is the time derivative of the gravitational potential, $\overline{T}_0$ is the mean CMB temperature we observe today and c the speed of light. Equation 1.15 can be equivalently written as an integral over radial comoving distance x_r according to [6]:

$$\Delta T(\hat{\mathbf{n}}) = \frac{2}{c^3}\overline{T}_0 \int_{0}^{x_{r,L}} \dot{\Phi}(x_r, \hat{\mathbf{n}})\, a\, \mathrm{d}x_r, \tag{1.16}$$

where $\hat{\mathbf{n}}$ is the unitary vector that points along the Line-Of-Sight (LOS), $x_{r,L}$ is the comoving radial distance to the surface of last scattering, a is the scale factor of the Universe, $\Phi(x_r, \hat{\mathbf{n}})$ is the gravitational potential differentiated respect to the conformal time, τ, along the photon's geodesic. This equation gives the amplitude of the signal to be detected [27].

With more detail, the ISW effect may be understood as follows: it is know that the Universe is well described by the ΛCDM cosmological model as proved by observations. By the presence of the cosmological constant, Λ, the Universe will expand at an accelerated rate, making the scale factor a to grow accelerated. Thus, the expansion of the Universe, driven by the cosmological constant makes the gravitational potential wells to decay as $\Phi \propto -1/a$ [6]. The ISW effect is underwent by the CMB photons when they pass through overdense or underdense regions in the Universe: when the photons pass through an overdense or cluster region, they will gain more energy falling into the potential well than the ammount they will loose when they climb out of the evolved shallower gravitational potential well. This is translated in an increase in the temperature of those photons, and can be seen as hot spots in CMB maps [6]. If the photons pass through underdense or void regions, then the photons first climb up the hill while losing energy and regain some energy when it descend the hill. Then, the photons decrease their temperature, and cold spots appear in CMB maps [6].

1.3.1 Perturbative General Relativity in ΛCDM and the Boltzmann Equation

With the goal to find the temperature fluctuation induced by the late ISW effect, it is necessary to study perturbative methods in the general relativity, applied to the cosmological model ΛCDM . In particular, it is necessary to apply perturbations over the FLRW metric (Equation 1.1), which describes a flat, homogeneous and isotropic universe. Thus, the general metric may be written as a perturbed FLRW metric (very near to an homogeneous and isotropic FLRW metric) and a FLRW background metric, without perturbations [20]:

$$g_{\mu\nu} = \overline{g}_{\mu\nu} + \delta g_{\mu\nu}, \tag{1.17}$$

where $\overline{g}_{\mu\nu}$ is the background metric shown in Equation 1.1 and $\delta g_{\mu\nu}$ is the perturbation to the metric. In the same way, it is possible to perform perturbations to the Einstein's field equations and with the help of the Friedmann equations such a problem may be studied. For a more detailed procedure, please see reference [20].

As metric perturbations may be scalar, vectorial and tensorial, it is only necessary to us to pay attention to the scalar perturbations in order to obtain the following line element [20]:

$$\mathrm{d}s^2 = a^2(\tau)\left[-(1-2\Phi)\mathrm{d}\tau^2 + (1-2\Psi)\delta_{ij}\mathrm{d}x^i\mathrm{d}x^j\right], \tag{1.18}$$

which is obtained in the Newtonian gauge. Here, τ is the conformal time and Φ y Ψ are the Bardeen potentials, which are Gauge invariant. When studying the photon's trajectory in this universe, and assuming that $|\Phi| \approx |\Psi|$ it is possible to obtain the temperature fluctuation of a photon that passes through a potential well that varies in time:

$$\Delta T(\hat{\mathbf{n}}) = \frac{2}{c^3}\overline{T}_0 \int_0^{x_{r,L}} \frac{\partial \Phi(x_r, \hat{\mathbf{n}})}{\partial \tau}\mathrm{d}x_r, \tag{1.19}$$

which is the same Equation 1.16, explained before. The assumption that $|\Phi| \approx |\Psi|$ is only possible in the Newtonian gauge and allows to assume that the gravitational potential have a classical behavior [20].

1.3.1.1 **Boltzmann Equation and Brightness Function**

This section presents a brief description of the Boltzmann equation for photons in the Newtonian gauge and will serve as basis to understand the CMB anisotropies. A more detailed discussion can be found in [23]. In general, the gauge choices to work with in the perturbed general relativity are physically equivalent, but it is necessary to choose a convenient gauge to describe and interpret the perturbed quantities; as shown before in Equation 1.18, the conformal Newtonian gauge is choosen. This gauge, although has a simple metric, is only valid for scalar perturbations. In this gauge, in order to describe the evolution of the perturbations in photons and neutrinos or the interactions between photons and baryons it is necessary to specify the evolution of a full distribution function $f(\mathbf{x}, \mathbf{p}, \tau)$, which gives the number density of particles in phase-space:

$$\mathrm{d}N = f(\mathbf{x}, \mathbf{p}, \tau)\mathrm{d}^3\mathbf{x}\ \mathrm{d}^3\mathbf{p}, \tag{1.20}$$

where the distribution function f is a invariant scalar under canonical transformations. When studying the geodesic equation of a free particle from the action principle and using a convenient set of non-canonical energy-momentum variables, E_q and q, respectively, it is possible to find a conservation law for the distribution function, known as the Boltzmann equation. For more details, please see the section 4.2.4 of [23]. The Boltzmann equation is then given by:

$$\frac{\partial f}{\partial \tau} + \frac{\mathrm{d}x^i}{\mathrm{d}\tau}\frac{\partial f}{\partial x^i} + \frac{\mathrm{d}q}{\mathrm{d}\tau}\frac{\partial f}{\partial q} = \left(\frac{\partial f}{\partial \tau}\right)_c, \tag{1.21}$$

where a term of second order in perturbed quantities is neglected. The term in the right hand side of Equation 1.21 is called collisional term, and describes the change of the distribution function due to collisions, i.e. interacions between photons and matter. Furthermore, to study the perturbation of the distribution function it is possible to write:

$$f = f_0 + f_1 \tag{1.22}$$

where f_0 is the unperturbed distribution function and f_1 is the perturbation. This unperturbed term f_0 may be a Fermi-Dirac distribution for fermions or a Bose-Einstein distribution for bosons with non-canonical momentum q. For the first order in the perturbed quantities, Equation 1.21 yields to the following equation for f_1 in Fourier space:

$$f_1' + \mathrm{i}k\mu\frac{q}{E_q}f_1 - \frac{q}{4}\frac{\partial f_0}{\partial q}\Psi_q = \left(\frac{\partial f_1}{\partial \tau}\right)_c, \tag{1.23}$$

with

$$\Psi_q \equiv -4\left[\Phi' - \mathrm{i}k\left(\frac{E_q}{q}\mu\Psi\right)\right] \quad \text{and} \quad \mu \equiv \frac{\mathbf{k}\cdot\mathbf{q}}{|\mathbf{k}||\mathbf{q}|}, \tag{1.24}$$

with Φ and Ψ as the Bardeen potentials shown in the metric of Equation 1.18 and the primes are derivatives with respect to the conformal time τ. For photons we have $E_q = q$, and is convenient to consider the brightness perturbation:

$$\Delta(k, q, \mu, \tau) = -f_1\left(\frac{q}{4}\frac{\partial f_0}{\partial q}\right)^{-1}. \tag{1.25}$$

For a Planck distribution, which is the case of CMB photons, the brightness perturbation function is related to the temperature perturbation as:

$$\Delta = 4\Theta \quad \text{with} \quad \Theta \equiv \frac{\Delta T}{T}. \tag{1.26}$$

In terms of the brightness perturbation function, Equation 1.23 becomes:

$$\Delta' + \mathrm{i}k\mu\Delta + \Psi_q = \left(\frac{\partial \Delta}{\partial \tau}\right)_c. \tag{1.27}$$

If we assume a coupling between baryons and photons in the form of a Thomson or Compton scattering interaction, which is the case before recombination, the collisional term will be:

$$\left(\frac{\partial \Delta}{\partial \tau}\right)_c = \sigma_{\mathrm{T}} n_e\, a(\delta_\gamma + 4\mathbf{v}_e\cdot\hat{\mathbf{q}} - \Delta), \tag{1.28}$$

where σ_T is the Thomson cross-section, n_e is the electron density, $\mathbf{v}_e$ is the peculiar velocity of electrons in proper units, $\hat{\mathbf{q}} = \mathbf{q}/|\mathbf{q}|$ and δ_γ is the perturbation to the density field of photons.

Equation 1.27 may be solved through and expansion of the μ-dependence of $\Delta(k, q, \mu, \tau)$ in Legendre polynomials:

$$\Delta(k, q, \mu, \tau) = \sum_{\ell=0}^{\infty} (-\mathrm{i})^{\ell} (2\ell + 1) \Delta_\ell(k, q, \tau) \mathscr{P}_\ell(\mu), \tag{1.29}$$

where the two relations

$$\Delta_0 = \frac{1}{2}\int_{-1}^{1} \Delta \, \mathrm{d}\mu = \delta_\gamma \quad \text{and} \quad \Delta_1 = \frac{1}{2}\int_{-1}^{1} \mathrm{i}\Delta\mu \, \mathrm{d}\mu = \frac{4}{3k}\theta_\gamma, \tag{1.30}$$

are important in order to solve the Equation 1.27 recursively. In those relations, θ_γ is the source function for the velocity field of photons.

1.3.2 Fluctuations in the CMB

In this section, we will talk about the observational quantities of the CMB: the temperature fluctuation and the Angular Power Spectrum. After that, we will discuss about the contribution of some anisotropies to the Angular Power Spectrum, focusing on the Integrated Sachs-Wolfe effect.

1.3.2.1 Angular Power Spectrum of the CMB

As aforementioned, the observed properties of the CMB are very well explained in the base of the standard ΛCDM cosmological model. Since the early Universe was so dense, hot and ionized, photons were absorbed and re-emited many times by electrons, establishing a black-body spectrum for the photons in the early Universe. As the Universe expanded and cooled, photons were scattered with lower frequency and they could propagate freely in the Universe, inheriting this black-body spectrum [23].

In 1989, the Cosmic Background Explorer (COBE) was launched by NASA in order to perform accurate measurements of the properties of the CMB in the entire sky. The Far InfraRed Absolute Spectrophotometer (FIRAS) on board COBE showed that the CMB has a spectrum perfectly consistent with a black-body spectrum, with a temperature $T = 2.728 \pm 0.002$K. But COBE was also able to measure for the first time an anisotropy in the CMB. The Differential Microwave Radiometers (DMR) also on board COBE showed that, although the CMB temperature distribution is highly isotropic over the sky, it has also small temperature fluctuations. The observed temperature map contains a component of anisotropy on very large angular scales well described by a dipole distribution [23], [7]:

$$T(\alpha) = \overline{T}_0 \left(1 + \frac{v}{c}\cos\alpha\right), \tag{1.31}$$

being α the angle of the line-of-sight (LOS) relative to a specific direction. This component is explained as a Doppler effect caused by the motion of the Earth with a velocity $v = 369 \pm 3$ km s^{-1} towards the direction $(l, b) = (264.31° \pm 0.20°, 48.05° \pm 0.10°)$ in Galactic coodinates. Once the mean temperature and the dipole anisotropy due to Doppler effect are substracted, the resulting map will present fluctuations in the temperature of the CMB of the order of $\Delta T/\overline{T} \sim 2 \times 10^{-5}$ and emission from the Milky Way disk, as shown in the lower panel of Figure 1.1 [23]. Following the detection by COBE, there have been a large number of experiments to measure small-scale CMB anisotropies, suchs as balloon-borne experiments or modern surveys as the Wilkinson Microwave Anisotropy Probe (WMAP) and Planck which have provided us with more detailed and accurate maps of the CMB anisotropies.

In order to quantify the observed temperature fluctuations, it is often common to expand the fluctuation temperature field in spherical harmonics:

$$\frac{\Delta T(\hat{\mathbf{n}})}{\overline{T}} \equiv \frac{T(\hat{\mathbf{n}}) - \overline{T}}{\overline{T}} = \sum_{\ell,m} a_{\ell m} Y_{\ell,m}(\vartheta, \varphi);\ a_{\ell m} \in \mathbb{C}, \tag{1.32}$$

where $\hat{\mathbf{n}} = (\vartheta, \varphi)$ is a direction on the sky and $\overline{T}$ is the mean CMB temperature. The values of $a_{\ell m}$ can be determined by observing the CMB and making measurements of $\Delta T/\overline{T}$ in all directions. Furthermore, the term $\ell = 1$ is the dipole anisotropy through space relative to the Hubble flow, i.e., the Doppler effect.

The observed CMB sky should be considered as one realization of a cosmic random process, where the expectation values of the square of the harmonic coefficients $a_{\ell m}$ give the angular power spectrum of the temperature fluctuations [23]:

$$C_\ell = \langle |a_{\ell m}|^2 \rangle \simeq \frac{1}{2\ell + 1} \sum_m |a_{\ell m}|^2, \tag{1.33}$$

which is an ensemble average with spherical symmetry, or an angular average over the $2\ell+1$ values of m in order to avoid the effect of an arbitrary choice of $\varphi = 0$. Equivalently, it is possible to define an auto-correlation function of the temperature fluctuations as [23]:

$$C(\vartheta) = \left\langle \frac{\Delta T(\mathbf{n_1})}{\overline{T}} \frac{\Delta T(\mathbf{n_2})}{\overline{T}} \right\rangle, \tag{1.34}$$

$$= \frac{1}{4\pi} \sum_\ell (2\ell + 1) C_\ell \mathscr{P}_\ell(\cos\vartheta); \quad \text{with} \quad \mathbf{n_1} \cdot \mathbf{n_2} = \cos\vartheta. \tag{1.35}$$

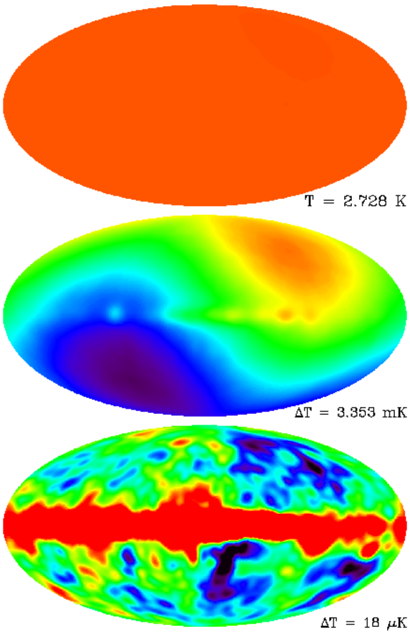

Figure 1.1: Temperature maps of the CMB in galactics coordinates. The upper panel shows the near-uniformity of the CMB brightness; the middle panel is the map after substraction of the mean brightness, showing the dipole component due to the motion of the Earth respect to the background; the bottom panel shows the temperature fluctuations after substraction of the dipole component. Emision from the Milky Way is evident in the bottom image [23]. Image taken from `http://lambda.gsfc.nasa.gov/product/cobe/dmr_image.cfm`

The last line in Equation 1.35 gives the relation between the auto-correlation function and the angular power spectrum through the Legendre polynomials $\mathscr{P}_\ell(\cos\vartheta)$. Also, when using the orthogonality properties of the Legendre polynomials, the inverse relation could be found [15]:

$$C_\ell = 2\pi \int_0^\pi C(\vartheta)\mathscr{P}_\ell(\cos\vartheta)\sin\vartheta \mathrm{d}\vartheta. \tag{1.36}$$

The values of C_ℓ contain much information about the physical conditions and constituents of the early Universe. From Equation 1.33, we can define the angular power spectrum to be $\ell(\ell+1)C_\ell/2\pi$. Every term in the summation is ≥ 0, so both positive and negative temperature fluctuations contribute to the angular power spectrum withouth cancelling each other. We will see more about the angular power spectrum in the following: from Equation 1.32, we can define the expansion coefficients $a_{\ell m}$ as [15]:

$$a_{\ell m} = \int \frac{\Delta T}{T}\, Y^*_{\ell m}(\vartheta,\varphi)\,\mathrm{d}\Omega. \tag{1.37}$$

Thus, we can take an ensemble average:

$$\langle a_{\ell m}\, a^*_{\ell' m'} \rangle = \iint \mathrm{d}\Omega_1\, \mathrm{d}\Omega_2\, Y^*_{\ell m}(\mathbf{n_1})\, Y_{\ell' m'}(\mathbf{n_2}) \left\langle \frac{\Delta T(\mathbf{n_1})}{\overline{T}}\, \frac{\Delta T(\mathbf{n_2})}{\overline{T}} \right\rangle. \tag{1.38}$$

Assuming spherical symmetry, the autocorrelation function $\langle \Delta T(\mathbf{n_1})/\overline{T}\ \Delta T(\mathbf{n_2})/\overline{T} \rangle$ can only depend on ϑ_{12}, where $\cos\vartheta_{12} = \mathbf{n_1} \cdot \mathbf{n_2}$. Expanding the autocorrelation function in Legendre polynomials $\mathscr{P}_n$:

$$\left\langle \frac{\Delta T(\mathbf{n_1})}{\overline{T}}\, \frac{\Delta T(\mathbf{n_2})}{\overline{T}} \right\rangle = \sum_n k_n\, \mathscr{P}_n(\cos\vartheta_{12}), \tag{1.39}$$

where k_n are constant coefficients, and with the addition theorem of spherical harmonics:

$$\sum_j Y_{nj}(\mathbf{n_1})\, Y^*_{nj}(\mathbf{n_2}) = \frac{2n+1}{4\pi}\, \mathscr{P}_n(\cos\vartheta_{12}). \tag{1.40}$$

Using Equation 1.39 and Equation 1.40 in Equation 1.38, renaming $C_n = 4\pi k_n/(2n+1)$ and applying some properties of the spherical harmonics, we can obtain the equality in Equation 1.33. Hence:

$$C_\ell = \int \mathrm{d}\Omega_1 \int \mathrm{d}\Omega_2\, Y^*_{\ell m}(\mathbf{n_1})\, Y_{\ell m}(\mathbf{n_2}) \left\langle \frac{\Delta T(\mathbf{n_1})}{\overline{T}}\, \frac{\Delta T(\mathbf{n_2})}{\overline{T}} \right\rangle. \tag{1.41}$$

Summing Equation 1.41 over m, produces a factor of $2\ell+1$ on the left, while on the right using Equation 1.40, we have:

$$\sum_{m=-\ell}^{\ell} C_\ell = (2\ell+1)C_\ell = \frac{2\ell+1}{4\pi} \int \mathrm{d}\Omega_1 \int \mathrm{d}\Omega_2\, \mathscr{P}_\ell(\cos\vartheta) \left\langle \frac{\Delta T(\mathbf{n_1})}{\overline{T}}\, \frac{\Delta T(\mathbf{n_2})}{\overline{T}} \right\rangle. \tag{1.42}$$

From Figure 1.2, the integration over Ω_2 in Equation 1.42 is performed first using spherical coordinates in the $x'y'z'$-frame at fixed $\mathbf{n_1}$. In this frame the coordinates of $\mathbf{n_2}$ are ϑ_{12} and φ_{12}. Because the integrand is axially symmetric around the z'-axis, we have:

$$\int \mathrm{d}\Omega_2 = 2\pi \sin\vartheta_{12} \mathrm{d}\vartheta_{12}. \tag{1.43}$$

Spherical symmetry renders the remaining integrand independent of $\mathbf{n_1}$, so that $\int \mathrm{d}\Omega_1$ produces just a factor of 4π. Then:

$$C_\ell = \frac{1}{4\pi} \int \mathrm{d}\Omega_1 \int_0^\pi 2\pi\ \sin\vartheta_{12} \mathrm{d}\vartheta_{12} \left\langle \frac{\Delta T(\mathbf{n_1})}{\overline{T}}\, \frac{\Delta T(\mathbf{n_2})}{\overline{T}} \right\rangle \quad \text{with} \quad \mathbf{n_1} \cdot \mathbf{n_2} = \cos\vartheta_{12}, \tag{1.44}$$

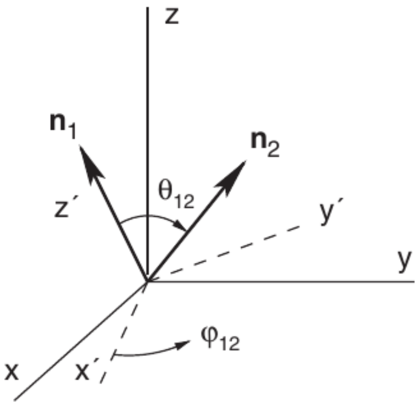

Figure 1.2: The integration over Ω_2 in Equation 1.42 is performed first, using spherical coordinates in the $x'y'z'$-frame at fixed $\mathbf{n}_1$. In this frame the coordinates of $\mathbf{n}_2$ are $\vartheta_{12},\ \varphi_{12}$. Because the integrand is axially symmetric around the z'-axis we have the expression of Equation 1.43, and the result is Equation 1.44. Spherical symmetry renders the remaining integrand independent of $\mathbf{n}_1$, so that $\int \mathrm{d}\Omega_1$ produces just a factor 4π. Image taken from [15].

$$C_\ell = \frac{4\pi}{2} \int_0^\pi C(\vartheta)\ \mathscr{P}_\ell(\cos\vartheta)\ \sin\vartheta\, \mathrm{d}\vartheta, \tag{1.45}$$

where we have changed $\vartheta_{12} \to \vartheta$ and applied Equation 1.34. This last equation is Equation 1.36. Now, expanding $C(\vartheta)$ in Legendre polynomials:

$$C(\vartheta) = \sum_n A_n\ \mathscr{P}_n(\cos\vartheta). \tag{1.46}$$

Inserting this last equation in Equation 1.45, and using:

$$\int_{-1}^{1} \mathscr{P}_n(x)\ \mathscr{P}_m(x)\, \mathrm{d}x = \frac{2}{2n+1}\delta^K_{nm}, \tag{1.47}$$

we obtain:

$$C_\ell = 2\pi \int_0^\pi A_n\ \mathscr{P}_n(\cos\vartheta)\ \mathscr{P}_\ell(\cos\vartheta)\ \sin\vartheta\, \mathrm{d}\vartheta \tag{1.48}$$

$$\Rightarrow A_\ell = \frac{(2\ell+1)\ C_\ell}{4\pi}. \tag{1.49}$$

Finally, replacing A_n in the expansion in Legendre polynomials for $C(\vartheta)$ and changing $n \to \ell$:

$$C(\vartheta) = \sum_\ell \frac{(2\ell+1)\ C_\ell}{4\pi}\ \mathscr{P}_\ell(\cos\vartheta), \tag{1.50}$$

which is Equation 1.35. The angular power spectrum given by

$$\Delta_T = \ell(\ell+1)C_\ell/2\pi, \tag{1.51}$$

from Equation 1.33 is shown in Figure 1.3. In this power spectrum, we speak of an angular frequency called the multipole moment ℓ. The reciprocal of ℓ corresponds to the angular scale. For example, $\ell = 10$ corresponds to roughly 10° on the sky, and $\ell = 100$ corresponds to roughly 1° on the sky[1].

The angular power spectrum of the anisotropy of the CMB contains information about the formation of the structures in the Universe and its current contents. This angular power spectrum is a plot of how much the temperature varies from point to point on the sky (the y-axis variable) $vs.$ the angular frequency ℓ[2]. In other words, this gives information about the amount of "power" that anisotropies would have according to its angular scale.

The power spectrum shows a flat plain at small values of ℓ, a fundamental peak around $\ell \simeq 200$, which corresponds to an angular size of about 1° on the sky, and a few harmonic peaks whose heights decline as ℓ approaches 1000; those peaks are called acoustic peaks. A detailed analysis shows that the location of the first peak is sensitive to the value of Ω_0, given by $\ell \simeq 200/\sqrt{\Omega_0}$. This angular power spectrum can be seen in Figure 1.3 where it is shown the best fit of the ΛCDM model, and in Figure 1.4, where we can see the relation between the different anisotropies and the angular power spectrum, as we will explain briefly later in subsubsection 1.3.2.2.

1.3.2.2 Contribution of the CMB Fluctuations to the Angular Power Spectrum

Given a cosmological model, it is possible to calculate the expected temperature fluctuations in the CMB. The temperature perturbation, at a space-time point $(\mathbf{x}, t)$, for photons propagating in a direction $\hat{\mathbf{q}}$ is related to the radiation brightness function Δ by Equation 1.26, [23] that can be re-written as:

$$\Theta(\hat{\mathbf{q}}, \mathbf{x}, t) \equiv \frac{\Delta T}{T}(\hat{\mathbf{q}}, \mathbf{x}, t) = \frac{\Delta(\hat{\mathbf{q}}, \mathbf{x}, t)}{4}. \tag{1.52}$$

It is possible to use the linearized Boltzmann equation (given by Equation 1.23) to write, for a perturbation mode $\mathbf{k}$ [23]:

$$(\Theta + \Psi)' + \mathrm{i}k\mu(\Theta + \Psi) = (\Phi + \Psi)' + \left(\frac{\Theta}{\tau}\right)_c \quad (\mu \equiv \hat{\mathbf{q}} \cdot \mathbf{k}), \tag{1.53}$$

---

[1] see `http://background.uchicago.edu/~whu/intermediate/map5.html`

[2] see `http://www.astro.ucla.edu/~wright/CMB-DT.html`

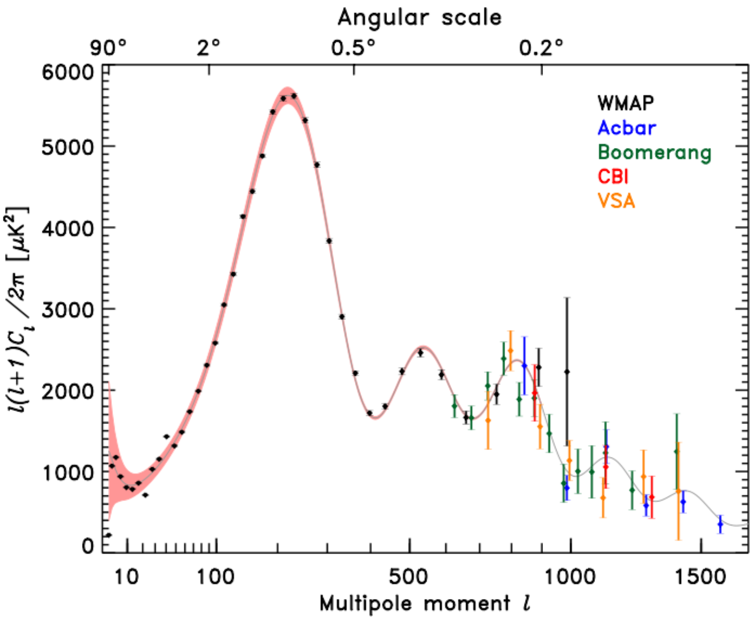

Figure 1.3: The angular power spectrum of the temperature fluctuations in the CMB. The solid line is the best-fit ΛCDM model.

being Φ and Ψ the metric perturbations in the conformal Newtonian gauge (Bardeen potentials of the perturbed metric given in Equation 1.18), the prime denoting a derivative with respect to conformal time $\tau = \int \mathrm{d}t/a(t)$, and the collisional term as a sum of the collisional term correspoding to a Compton interaction (Equation 1.28) plus a polarization term:

$$\left(\frac{\partial\Theta}{\partial\tau}\right)_c = \sigma_{\mathrm{T}} n_e\, a \left(\frac{\delta_\gamma}{4} + \mathbf{v}_e \cdot \hat{\mathbf{q}} - \Theta + \text{polarization term}\right). \tag{1.54}$$

Integrating Equation 1.53 it is possible to find a relation between the temperature fluctuations we observe today (at τ_0) with those on the surface of last-scattering (at τ_*) by [23]:

$$\begin{aligned}[\Theta + \Psi](k,\mu,\tau_0) =& [\Theta + \Psi](k,\mu,\tau_*) e^{ik\mu(\tau_* - \tau_0)} \\ &+ \int_{\tau_*}^{\tau_0} \left[(\Phi+\Psi)' + \left(\frac{\partial\Theta}{\partial\tau}\right)_c\right]_\tau e^{ik\mu(\tau-\tau_0)}\mathrm{d}\tau,\end{aligned} \tag{1.55}$$

where the exponential factors describe the phase shifts of the perturbation mode in question. The first term on the right-hand side is due to intrinsic fluctuation in the surface of last-scattering, while the term containing $(\Phi + \Psi)'$ in the integral is the contribution from the change of the gravitational potential along the path of the photon. The collisional term accounts for possible non-gravitational interaction of the CMB photons with

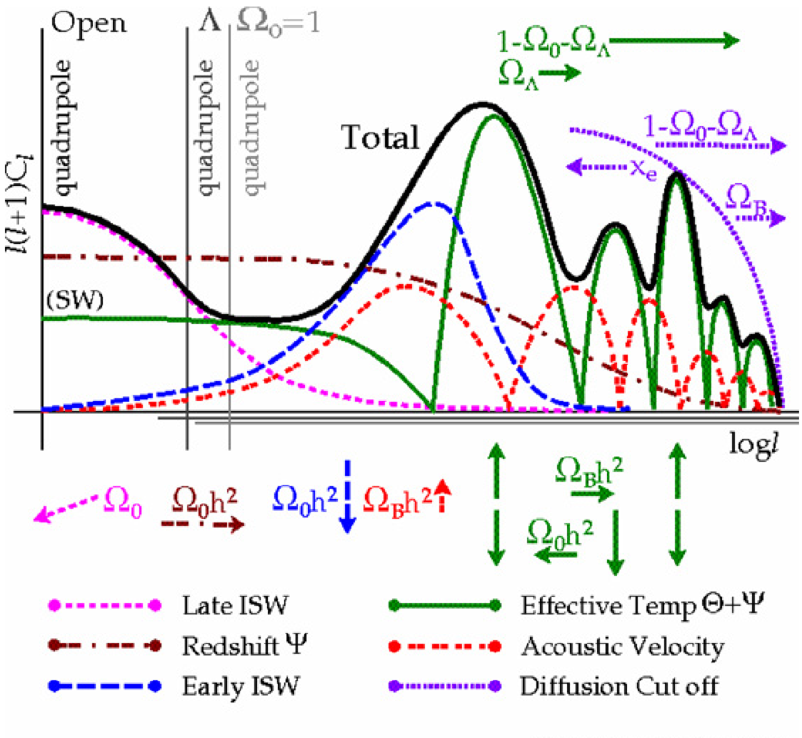

Hu, Sugiyama, & Silk (1995)

Figure 1.4: Anisotropies in the angular power spectrum of the CMB. We can see the contributions of the Early SW effect, which is produced in the surface of last scattering and the contribution of the Late ISW effect which is the effect we are studying in this work. The Late ISW effect contributes only for small multipole moment ℓ which means that it can be detected only in large scales. Effective temperature is divided in a Non-integrated SW effect and baryonic acoustic oscillations (both represented by the green curve), which account for the peaks of the power spectrum, while the acoustic velocity of the BAOs (red curve) accounts for the valleys between peaks.

baryons after decoupling [23]. This equation can be integrated once the time dependence of the perturbation quantities is solved, and again, the μ dependence can be expanded in harmonics to obtain the angular power spectrum C_ℓ. Also, almost all cosmological parameters ($\Omega_{m,0}$, $\Omega_{\Lambda,0}$ $\Omega_{b,0}$ h) and the power spectrum $P(k)$ can affect the pattern of the predicted CMB anisotropies, as shown in Figure 1.4. In the following, we will see some of those anisotropies and their corresponding contribution to the angular power spectrum.

(a) Sachs-Wolfe Effect (Large-Scale Fluctuation): The CMB radiation comes to us from the surface of last-scattering at redshift $z_{\rm dec} \approx 1100$. A physical event at $z = z_{\rm dec}$, characterized by a length scale l in comoving units, subtends an angle:

$$\vartheta(l) = \frac{l}{d_{\rm A}(z_{\rm dec})(1+z_{\rm dec})}, \tag{1.56}$$

where $d_{\mathrm{A}}(z) = a_0 x(z)/(1+z)$ is the angular-diameter distance to redshift z and $a_0 = 1$ is the scale factor at present time. For a flat Universe with $\Omega_{m,0} + \Omega_{\Lambda,0} = 1$ we have $x(z) \approx 2(2H_0^2\, a_0^2\, \Omega_{m,0})^{-1/2}$. Furthermore, the Hubble radius, in proper units at $z \gg 1$, which defines a causally conected region is given by $d_{\mathrm{H}}(z) = cH^{-1}(z)$. With those definitions, we have that a causally conected region at the time of decoupling subtends an angular scale (for an universe with $\Omega_{m,0} + \Omega_{\Lambda,0} = 1$):

$$\vartheta_{\mathrm{d}} \equiv \vartheta_{\mathrm{H}}(z_{\mathrm{dec}}) \approx 0.87^\circ \left(\frac{z_{\mathrm{dec}}}{1100}\right)^{-1/2}. \tag{1.57}$$

On scales larger than ϑ_{d}, the observed temperature fluctuations are entirely due to super-horizon perturbation in space-time, while on scales smaller than ϑ_{d} evolutionary effects may be relevant. Since the angular scale corresponding to harmonic ℓ is roughly given by $\vartheta_\ell \approx \pi/\ell$, the Hubble radius at decoupling corresponds to $\ell \sim 200$, for an universe with $\Omega_{m,0} + \Omega_{\Lambda,0} = 1$. Then, for angular scales $\vartheta \gg \vartheta_{\mathrm{d}}$, the density perturbations responsible for the temperature fluctuations have $k \ll 2\pi a/(c\, t_{\mathrm{dec}})$, i.e. their scale sizes are much larger than the Hubble radius at z_{dec}. In this case, the collisional term of Equation 1.55 can be neglected and, expanding the μ dependence of $\Theta(k, \mu, \tau_*)$ in Legendre polynomials to the two lowest order components (obtained with the help of Equation 1.29), we have

$$[\Theta + \Psi](k, \mu, \tau_0) = \left[\Psi + \frac{\delta_\gamma}{4} + \Theta_v\right](k, \tau_*) e^{\mathrm{i}k\mu(\tau_* - \tau_0)} + \int_{\tau_*}^{\tau_0} (\Phi' + \Psi') e^{\mathrm{i}k\mu(\tau - \tau_0)} \mathrm{d}\tau \tag{1.58}$$

with $\Theta_0 = \delta_\gamma/4$ and $\Theta_v = -3\mathrm{i}\Theta_1\mu = -\mathrm{i}\theta_\gamma\mu/k = \mathbf{v}\cdot\hat{\mathbf{q}}$.

In the case in which Φ and Ψ do not explicitly depend on time, the integral in Equation 1.58 is zero and the observed temperature fluctuations are caused by the intrinsic fluctuations of the photon density $\delta_\gamma(\tau_*)$ at the surface of last-scattering, a Doppler shift $(\mathbf{v}\cdot\hat{\mathbf{q}})(\tau_*)$ due to the motion of the surface of last-scattering, and the potential difference between the observer and the surface of last-scattering $\Psi(\tau_*)$. The temperature fluctuations due to intrinsic and potential fluctuations together, also denominated effective temperature, are called the Sachs-Wolfe effect. This decomponision of the Sachs-Wolfe effect into the intrinsic and potential parts is defined in the Newtonian gauge; if another gauge is used, the Sachs-Wolfe effect may correspond to a different combination of perturbation quantities [23]. In Figure 1.4, the Sachs-Wolfe effect, or effective temperature is shown as the green-solid line, that at low multipoles ℓ (or larger scales) generates what is known as the Sachs-Wolfe plateau. This effective temperature also has a modulation due to Baryonic Acoustic Oscillations, as we will show later and its amplitude and positions of the peaks depend on the values of $\Omega_{m,0}$ and $\Omega_{b,0}$.

It is also possible to relate the Sachs-Wolfe effect with initial perturbations. Assuming that at the time of the surface of last scattering the universe is matter dominated, and also assuming that initial perturbations are isentropic in the long wavelength limit:

$$\Psi(\mathbf{k},\tau_*) = \Phi(\mathbf{k},\tau_*) = \frac{9A(\mathbf{k})}{10} \quad \text{with} \quad A(\mathbf{k}) = \Psi(\mathbf{k},\tau\to 0), \tag{1.59}$$

$$\delta_\gamma(\mathbf{k},\tau_*) = -\frac{8}{3}\Psi(\mathbf{k},\tau_*), \tag{1.60}$$

then

$$\Theta^{\text{SW}}(k,\mu,\tau_0) = \frac{1}{3}\Psi(\mathbf{k},\tau_*)e^{\text{i}k\mu(\tau_*-\tau_0)}. \tag{1.61}$$

When expanding $\Theta^{\text{SW}}(k,\mu,\tau_0)$ in Legendre polynomials in a similar way as in Equation 1.29, it is possible to find:

$$C_\ell = \langle|a_{\ell m}|^2\rangle = \frac{2V_{\text{u}}}{\pi}\int_0^\infty \langle|\Theta_\ell^{\text{SW}}(k,\tau_0)|^2\rangle k^2 \text{d}k \tag{1.62}$$

$$\propto \int_0^\infty \frac{P_{\text{i}}(k)}{k^2} j_\ell^2(k\tau_0)\text{d}k, \tag{1.63}$$

where V_{u} is a convenient integration volume, $j_\ell(k\tau_0)$ are the spherical Bessel functions and $P_{\text{i}}(k) = k^4\langle|A(\mathbf{k})|^2\rangle$ is the initial power spectrum. For a power-law spectrum $P_{\text{i}}(k) \propto k^n$, Equation 1.63 gives [23]:

$$C_\ell = C_2\frac{\Gamma\left[\ell + \left(\frac{n-1}{2}\right)\right]\Gamma\left[\frac{9-n}{2}\right]}{\Gamma\left[\ell + \left(\frac{5-n}{2}\right)\right]\Gamma\left[\frac{3+n}{2}\right]}; \tag{1.64}$$

and in the special case of a scale-invariant power spectrum $P_{\text{i}}(k) \propto k$ [23]:

$$C_\ell = \frac{1}{2\ell(\ell+1)}. \tag{1.65}$$

Then, for an scale-invariant power spectrum we have that $\ell(\ell+1)C_\ell$ is independent of ℓ.

(b) The Integrated Sachs-Wolfe Effect: If $\Phi + \Psi$ is time-dependent in Equation 1.58, there is an additional contribution to the temperature fluctuations due to the integral term. Such a contribution is denominated Integrated Sachs-Wolfe (ISW) effect [23]. There are two possibilities to generate this ISW effect in the linear regime:

- First, in an open universe, or in flat universes with a cosmological constant, the linear gravitational potential decays with time. Because this kind of potential decay occurs only at later times when the curvature or the cosmological constant dominates the dynamics of such kind of universe, this effect on the CMB is referred as the late ISW effect, which is the effect we are studying in this work.

  In Figure 1.4, the late ISW effect is shown as a pink short-dashed line that has a contribution only at very low multipole ℓ values. This feature present before the Sachs-Wolfe plateau is also known as ISW Rise. As the contribution of this effect to the Angular Power Spectrum is at low ℓ, this gives rise to the difficulty to measure and detect the late ISW effect, because this region of low multipole values suffers from a large cosmic variance, as can be seen in Figure 1.3 at low ℓ.

- Second, since the Universe is not completely matter dominated at the decoupling time, the density perturbations grow (Equation 1.13) with time more slowly than the scale factor, according to [23];

  $$D \propto 1 + \frac{3}{2}\zeta \quad \text{with} \quad \zeta = \frac{a}{a_{\text{eq}}} \tag{1.66}$$

  being a_{eq} the value of the scale factor at the epoch of equivalence between radiation and matter. This slow growth causes the potential to decay until the Universe becomes fully matter dominated. The temperature fluctuations caused by this potential decay are referred as the early ISW effect, because they were produced close to decoupling. The contribution of this early ISW effect is shown in Figure 1.4 as the blue-dashed line. The amplitude of this effect depends on the value of $\Omega_{m,0}$ and has a contribution to the width and amplitude of the first acoustic peak.

From Equation 1.58, it is possible to expand again in Legendre polynomials and find that the contribution of the ISW effect can be written as:

$$\Theta_\ell^{\text{ISW}}(k,\tau_0) = \int_{\tau_*}^{\tau_0} (\Phi+\Psi)' j_\ell[k(\tau_0-\tau)]\mathrm{d}\tau. \tag{1.67}$$

As the Bessel function j_ℓ peaks at $k(\tau_0 - \tau) \sim \ell$, and the potential evolution is important for modes within the horizon, the largest effect is typically for modes with $\ell \sim \ell_c \sim (\tau_0 - \tau_c)/\tau_c$ [23], with τ_c the time when the potential starts to evolve significantly, although all modes with $\ell > \ell_c$ can be affected. The early ISW effect is expected to peak roughly at the scale corresponding to the horizon size at decoupling, i.e. at $\ell \sim 200$ in a flat universe.

For a flat ΛCDM universe, the cosmological constant starts to dominate the energy content at $z \sim (\Omega_{\Lambda,0}/\Omega_{m,0})^{1/3} - 1$; then, the late ISW effect is expected to peak roughly at the present horizon scale, i.e. at very low ℓ [23].

(c) **Acoustic Peaks:** On angular scales $\vartheta \lesssim \vartheta_{\mathrm{d}}$ (Equation 1.57), the CMB can be affected by non-gravitational effects. For example, at decoupling time the Jeans length is larger than the horizon size; then, all baryonic perturbations that may have come through the horizon before decoupling oscillate as acoustic waves in the tightly coupled photon-baryon fluid. This gives rise to an oscillatory pattern in the CMB power spectrum at angular scales $\vartheta < \vartheta_c \sim 1^\circ$.

The evolution of the baryonic content of the Universe may have an acoustic wave solution. Due to the coupling with photons, it is also possible to understand the qualitative behavior of the acoustic pattern in the CMB through this solution. As the photon-baryon fluid is tightly coupled, we have that the acoustic wave solution takes the form [23]:

$$\Theta_0(\tau) + \Psi = [\Theta_0(0) + (1+\mathscr{R})\Psi]\cos(kc_s\tau) + \frac{1}{kc_s}\Theta_0'(0)\sin(kc_s\tau) - \mathscr{R}\Psi, \tag{1.68}$$

with c_s as the speed of sound, $\mathscr{R} \equiv (3\overline{\rho}_b)/(4\overline{\rho}_\gamma) \approx 27\Omega_{b,0}h^2\,[1100/(1+z_{\mathrm{dec}})]$ and where $\Theta_0(0)$ and $\Theta_0'(0)$ are determined by the initial conditions. This solution is only valid if the potential Ψ is constant, which is true only in a matter dominated era. Here, $\Theta_0 \equiv \delta_\gamma/4 = \delta_b/3$ is the temperature fluctuation due to the isotropic part of the perturbation in photon number density. However, the observed temperature fluctuation is the sum of the effective temperature $\Theta_0 + \Psi$ and the Doppler term due to acoustic velocity [23]:

$$\Theta_v(\tau) = -\frac{3\mu}{k}\Theta_0' = \sqrt{3}c_s[\Theta_0(0) + (1+\mathscr{R})\Psi]\sin(kc_s\tau) - \frac{\sqrt{3}}{k}\Theta_0'(0)\cos(kc_s\tau). \tag{1.69}$$

The form of the acoustic oscillation is governed by the two initial conditions $\Theta_0(0)$ and $\Theta_0'(0)$. The cosine part in Equation 1.68 represents an isentropic mode, since it is driven by the initial metric perturbations (given by Ψ). Meanwhile, the sine part in Equation 1.68 represents the isocurvature mode, because it corresponds to zero initial metric perturbations [23]. It is very difficult to construct a pure isocurvature model that match the observed CMB power spectrum; thus, we are going to concentrate only in the isentropic part of the model, that allows to explain the observations.

As the fluctuations in the effective temperature on super-horizon scales are due to the Sachs-Wolfe effect, it is possible to consider $\Psi = \Phi$ as constants for those super-horizon perturbations, and then the initial condition for perturbations which come through the horizon in the matter dominated era may be written as $(\Theta_0 + \Psi)(0) = \Psi/3$. The acoustic waves at the decoupling time may be written as:

$$\Theta_0(\tau_*) + \Psi = \frac{\Psi}{3}(1 + 3\mathscr{R}) \cos{(kl_s)} - \mathscr{R}\Psi, \tag{1.70}$$

where l_s is the size of the sound horizon at decoupling. If the initial perturbation spectrum does not oscillate significantly for $k \gtrsim 1/l_s$, then the modes of the effective temperature fluctuations with $k = m\pi/l_s$ (with $m = 1, 2, 3, ...$) have extremal amplitudes:

$$|\Theta_0(\tau_*) + \Psi| = \begin{cases} |\Psi|\frac{1+6\mathscr{R}}{3} & (m \quad = \text{odd}), \\ \frac{|\Psi|}{3} & (m \quad = \text{even}). \end{cases} \tag{1.71}$$

Hence the amplitude of an $m =$ odd mode is enhanced by a factor of $1+6\mathscr{R}$ relative to that of an $m =$ even mode. Since each k is associated with a characterisctic scale on the surface of last-scattering, these extrema correspond to peaks in the CMB power spectrum C_ℓ. Those periodic peaks can be seen in Figure 1.4 as part of the effective temperature along with the Sachs-Wolfe effect, i.e. it appears as the solid green-line but for higher values of ℓ.

The Doppler effect for the same isentropic initial condition is given by:

$$\Theta_v(\tau_*) = \frac{c_s}{\sqrt{3}}\Psi(1 + 3\mathscr{R}) \sin{(kl_s)}. \tag{1.72}$$

This Doppler effect due to acoustic velocity also produces peaks in the CMB, but with a phase shift of $\pi/2$ relative to $\Theta_0(\tau_*) + \Psi$. Since $\mathscr{R}$ at decoupling is not much smaller than 1, the peaks given by Θ_v are lower than those given by $\Theta_0(\tau_*) + \Psi$ and so, in C_ℓ, they fill the valleys between the peaks of $\Theta_0(\tau_*) + \Psi$ rather than appearing as peaks. This feature can be seen as the double-dashed red-line in Figure 1.4.

The positions of the acoustic peaks in the C_ℓ are determined by the physical size of the sound horizon at decoupling, l_s, and the angular-diameter distance of the surface of last-scattering. For an universe with $\Omega_{m,0} + \Omega_{\Lambda,0} = 1$, this position is given by:

$$\ell_m \approx \frac{m\pi(1+z_{\rm dec})d_{\rm A}(z_{\rm dec})}{l_s} \approx 200m(1+\mathscr{R})^{1/2}. \tag{1.73}$$

It is possible to see how the position of the peaks depend on $\Omega_{b,0}$ through the $\mathscr{R}$ dependence. From Equation 1.71, the heights of the odd peaks increase with $\Omega_{b,0}$ but it does not affect the even peaks. Since the contributions from acoustic velocities increase with $\mathscr{R}$, the depths of the valleys depend also son $\Omega_{b,0}$.

Furthermore, the heights of the acoustic peaks may be affected by $\Omega_{m,0}$. This dependence comes from the fact that potentials are time dependent in realistic models, and also, for perturbations inside the horizon the time evolution in the mass component can induce a potential evolution through the Poisson equation, and so potentials must respond to the acoustic oscilation in the photon-baryon fluid. As the change in the potential is in resonance with the acoustic oscillation, this leads to a boost in the amplitude of the acoustic oscillation. For isentropic modes, the boost is larger for smaller $\Omega_{m,0}h^2$, and for acoustic perturbations which come through the horizon at higher z, i.e., peaks with larger ℓ [23].

Finally, the damping effect in the acoustic peaks, given by the dotted purple-line in Figure 1.4, may be due to several factors. One of those factors is the imperfect coupling between baryons and photons during decoupling, causing a damping in δ_γ on scales smaller than some damping scale $l_{\rm d}$. This damping suppresses the temperature fluctuations on scales correponding to $l \gtrsim 2000$ [23]. Another important damping of the temperature fluctuations on small scales comes from the fact that the surface of last-scattering has a finit thickness. As the width in redshift of the surface of last-scattering is $\Delta z \approx 80$, the observed temperature fluctuation is a superposition of the temperature fluctuations distributed within this finite width [23].

1.4 Cosmological Simulations of Formation of Structures

In the hierarchical picture of structure formation, small objects collapse first and then merge to form larger and larger structures in a complex way. This formation process is evident in the intricate structure of galaxy clusters, whose properties depend on how the thousands of smaller objects that the cluster accretes are destroyed or survive within the cluster gravitational potential. These merging events are source of processes such as shocks, turbulence and acceleration of relativistic particles in the intracluster medium. In order to model these processes realistically, we need to resort to numerical simulations which are capable of resolving and following correctly the highly non-linear dynamics. Numerical simulations started in the 60s (Aarseth 1963) and 70s (Peebles 1970; Press & Schechter 1974) with simple N-body problems solved using N-body codes with a few hundred particles. Later the Particle-Particle (PP) code, or direct summation of all two-body forces, was polished and brought to the state-of-art (Aarseth 1985). From this moment, problems such a more realistic density profile and the generation of initial conditions were solved with the help of different approximations to the structure-formation models and the implementation of a variety of new numerical methods and codes which allows to find more resolution in the forces calculation and particle's positions. Some methods are described in the following sections.

1.4.1 N-body Simulations and Equations of Evolution of Fluctuations in Expanding Universe

Usually the problem of the formation and dynamics of cosmological objects is formulated as N-body problem: for N point-like objects with given initial positions and velocities find their positions and velocities at any later moment. Over most of the cosmic time of interest for structure formation, the Universe is dominated by dark matter. The most favourable model turned out to be the so-called Cold Dark Matter (CDM) model. The CDM can be described as a collisionless, non-relativistic fluid of particles of mass m, comoving coordinate position $\mathbf{x}$ and momentum $\mathbf{p}$. In general, if we neglect the baryonic component, the system is described by the distribution functions $f_i(\mathbf{x}, \mathbf{p}, t)$; for a simple CDM model we have only one component. The phase-space distribution function of the dark-matter fluid (CDM) can be described by the collisionless Boltzmann equation (CBE or Vlasov equation) coupled to the Poisson equation:

$$\frac{\partial f}{\partial t} + \frac{\mathbf{p}}{ma^2}\nabla f - m\nabla\Phi\frac{\partial f}{\partial \mathbf{p}} = 0; \text{ where } \mathbf{p} = ma^2\dot{\mathbf{x}}, \tag{1.74}$$

$$\nabla^2\Phi(\mathbf{x}, t) = 4\pi G a^2[\rho(\mathbf{x}, t) - \overline{\rho}(t)]. \tag{1.75}$$

Here the proper mass density can be inferred by integrating the distribution function over the momenta $\mathbf{p}$.

$$\rho(\mathbf{x}, t) = \int f(\mathbf{x}, \mathbf{p}, t)\, \mathrm{d}^3p. \tag{1.76}$$

This set of equations represents a high-dimensional problem. The solution of the CBE equation can be written in terms of equations of characteristics, which *look* like equations of particle motion:

$$\frac{\mathrm{d}\mathbf{p}}{\mathrm{d}t} = -m\nabla\Phi, \tag{1.77}$$

$$\frac{\mathrm{d}\mathbf{x}}{\mathrm{d}t} = \frac{\mathbf{p}}{ma^2}. \tag{1.78}$$

These equations can be written in other form when using the proper peculiar velocity $\mathbf{v} = a\dot{\mathbf{x}}$:

$$\frac{\mathrm{d}\mathbf{v}}{\mathrm{d}t} + \mathbf{v}\frac{\dot{a}}{a} = -\frac{\nabla\Phi}{a}, \tag{1.79}$$

where the time derivative of the scale factor $\dot{a}$, can be obtained from the Friedmann equation as:

$$\dot{a} = H_0\sqrt{1 + \Omega_{m,0}(a^{-1} - 1) + \Omega_\Lambda(a^2 - 1)}. \tag{1.80}$$

One of the most famous N-body simulation is the Millennium simulation performed by the Virgo Consortium in 2005. With the help of the Max Planck Society's Supercomputing Centre in Garching, Germany, they traced the evolution of the matter distribution in a cubic region of the Universe over 2 thousand million light-years on a side of 2160^3 particles, where each particle represents approximately a thousand million solar masses of dark matter. They have been able to recreate the evolutionary histories both for 20 million galaxies which populate this volume and for the supermassive black holes which occasionally power quasars at their hearts. By comparing such simulated data to large observational surveys, they can clarify the physical processes underlying the buildup of real galaxies an black holes[1]. A picture with some results is shown in Figure 1.5.

1.4.2 Codes and Methods

There are many different numerical techniques to follow the evolution of a system of many particles. Most of the methods for cosmological applications take some ideas from three techniques: Particle Mesh (PM) code, direct summation of Particle-Partilce code, and the TREE code. All methods have their advantages and disadvantages.

---

[1] see `http://www.mpa-garching.mpg.de/galform/virgo/millennium/`

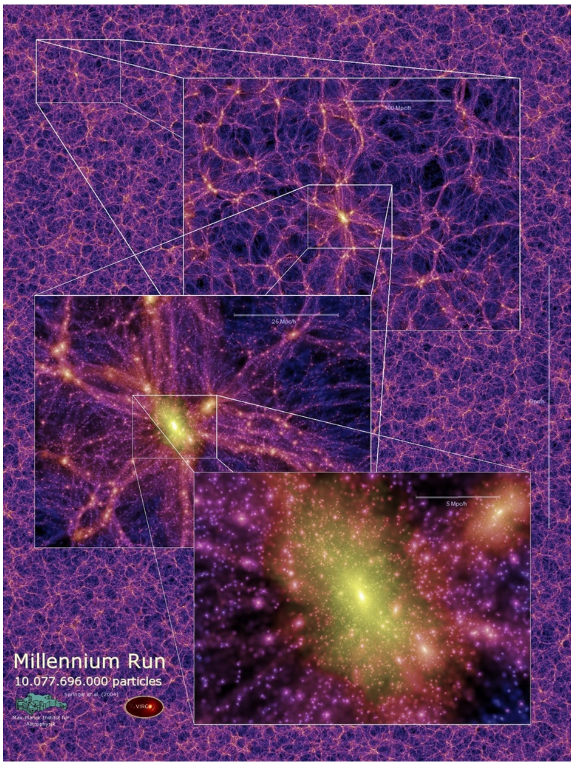

Figure 1.5: Results from the Millenium Project, 2005. The results of this simulation show us filaments and other structures also detected in the observations. Taken from `http://www.mpa-garching.mpg.de/galform/virgo/millennium/`.

Direct Sum: The most direct way to solve the N-body problem is to sum directly the contributions of all the individual particles to the gravitational potential $\Phi(\mathbf{r})$:

$$\Phi(\mathbf{r}) = -G \sum_j \frac{m_j}{(|\mathbf{r} - \mathbf{r}_j|^2 + \epsilon^2)^{1/2}}, \tag{1.81}$$

where G is the gravitational constant, m_j is the mass of j-ith particle, $\mathbf{r}_j$ its corresponding position and ϵ is a gravitational softening. In principle, this sum would represent the exact (Newtonian) potential which generates the particle's acceleration. In a collisionless models close encounters between individual particles are irrelevant to the physical problem under considerations, but in such N-body simulations, close encounters could occur, leading to numerical inconsistencies, then the gravitational force between two particles must be smoothed by introducing the gravitational softening ϵ. This softening reduces the spurious two-body relaxation which occurs when the number of particles in the simulation is not large enough to represent correctly a collisionless fluid. This situation however is unavoidable, because the number of dark matter particles in real systems is orders of magnitude larger than the number that can be handled in a numerical simulation. Typically, ϵ is chosen to be $1/20 - 1/50$ of the mean inter-particle separation within the simulation. In general, this direct-sum approach is considered to be the most accurate technique, and is used for problems where superior precision is needed. However this method has the disadvantage of being already quite CPU intensive for even a moderate number of particles, because the computing time is $\propto O(N^2)$, where N is the total number of particles.

PM Code: This method uses a mesh to produce density and potential. As the result, its resolution is limited by the size of the mesh. There are two advantages of the method: (1) it is fast, because it has the smallest number of operations per particle per time step of all the other methods, (2) it typically uses very large number of particles.

The PM method treats the force as a field by computing it on a mesh. Differential operators, such as the Laplacian, are replaced by finite difference approximations Potentials and forces at particle positions are obtained by interpolation on the array of mesh-defined values. Typically, such an algorithm is performed in three steps. First, the density on the mesh point is computed by assigning densities to the mesh from the particle positions. Second, the density field is transformed to Fourier space, where the Poisson's equation is solved. Alternatively, the potential can be determied by solving Poisson's equation iteratively with relaxation methods. In a third step the forces for the individual particles are obtained by interpolating the derivatives of the potential of the particle positions. Typically, the amount of mesh cells N_g used is lower respect to the number of particles in the simulation, so that when structures form, one can have large numbers of particles within individual mesh cells, which immediately illustrates the shortcoming of this method: its limited resolution. On the other hand, the calculation of the Fourier transform via a Fast Fourier Tranform (FFT) is extremely fast, as it only needs of order $O\left(N_g \log\left(N_g\right)\right)$ operations, which is the advantage of this method.

There are many schemes to assign the mass density of the mesh. The simplest method is the "Nearest-Grid-Point" (NGP). Here, each particle is assigned to the closest mesh point, and the density at each mesh point is the total mass assigned to the point divided by the cell volume. One of its drawbacks is that it gives forces that are discontinuous. The "Cloud-in-a-Cell" (CIC) scheme is a better approximation to the force: it distributes every particle over the nearest 8 grid cells, and then weigths them by the overlapping volume, which is obtained by assuming the particle to have a cubic shape of the same volume as the mesh cells. The CIC method gives continuous forces, but discontinuous first derivatives of the forces. A more accurate scheme is the "Triangular-Shaped-Cloud" (TSC) method. This scheme has an assignment interpolation function that is piecewise quadratic.

The advantage of such PM methods is the speed, because the number of operations scales with $N + N_g \log(N_g)$, where N is the number of particles and N_g the number of mesh points. However, the disadvantage is that the dynamical range is limited by N_g, which is usually limited by the available memory. An sketch of a PM code can be seen in Figure 1.6.

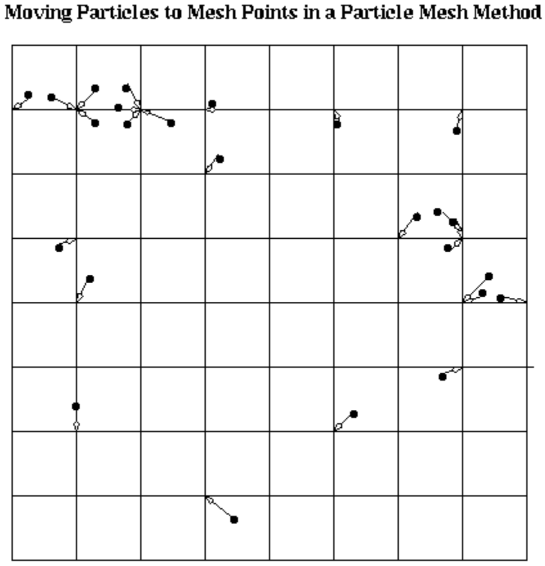

Figure 1.6: Particle-Mesh method. This method superimposes a regular grid over the set of particles, and creates an approximation of the original problem by moving particles to the nearest grid points. Taken from `http://www.cs.berkeley.edu/~demmel/cs267/lecture16/lecture16.html`.

P^{3}M Code: This method has two parts: A PM part which takes care of large-scale forces, and a PP part, which adds small-scale particle-particle contribution. Because of strong clustering at late stages of evolution, PP part becomes prohibitively expensive once large objects start to form in large numbers. One of the major problems for these codes is the correct splitting of the force into a short-range and long-range part. The PM method is only able to produce reliable inter particle forces down to a minimum of at least two grid cells. For smaller separations the force can no longer be represented on the grid and therefore it is necessary to introduce a cut-off radius r_e (larger than two grid cells), where for $r < r_e$ the force should smoothly go to zero. The parameter r_e defines the chaining-mesh and for distances smaller than this cut-off radius a contribution from the direct PP summation needs to be added to the total force acting on each particle. This PP force should smoothly go to zero for very small distances in order to avoid unphysical particle-particle scattering. This cut-off of the PP force determines the overall force resolution of a P^{3}M code. An sketch of this P^{3}M method is shown in Figure 1.7 .

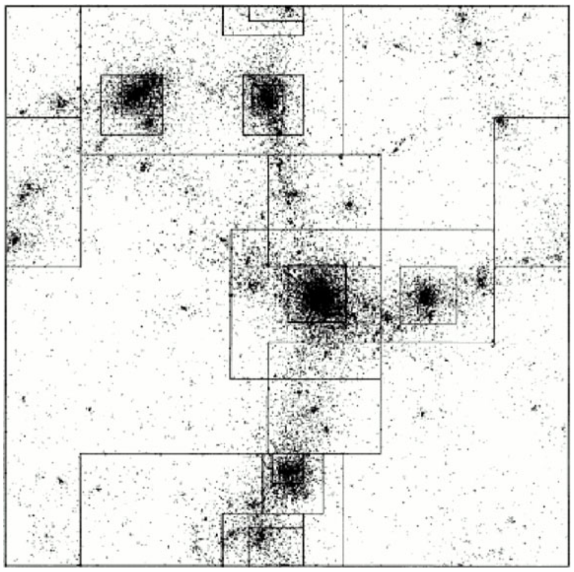

Figure 1.7: Distribution of grid refinements placed with a particular kind of P^3M method. Taken from `http://www.cs.berkeley.edu/~demmel/cs267/lecture16/lecture16.html`.

TREE Code: It is the most flexible code in the sense of the choice of boundary contidions. It is also more expensive than PM: it takes 10-50 times more operations. The method of the tree algorithm consist in solving the N-body problem with a hierarchical multipole expansion. This method groups distant particles into larger cells, allowing their gravity to be accounted for by means of a single or many multipole force terms. Instead of requiring $N-1$ partial force evaluations per particle, as needed in a direct-summtion approach, the gravitational force on a single particle can be computed with substantially fewer operations, because distant groups are treated as “macro” particles in the sum. In this manner the sum usually reduces to $N\log(N)$ operations.This scaling is only true for homogeneous particle distributions. An schematic illustrations of a tree code is shown in Figure 1.8.

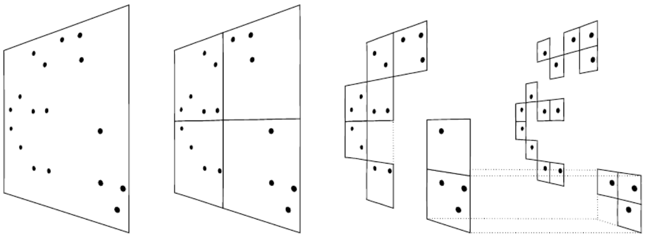

Figure 1.8: Schematic illustration of a kind of Tree code, called Barnes and Hut approximation. The particles are first enclosed in a square (root node). This square is then iteratively subdivided into four squares of half the size, until exactly one particle is left in each final square (leaves of the tree). In the resulting tree structure, each square can be the progenitor of up to four siblings. Taken from [8].

CHAPTER

2

Computational Methods and Construction of the Maps of $\delta(\mathbf{x})$ and $\dot{\Phi}(\mathbf{x})$

This chapter includes a description of the computational methods developed throughout the work with the aim to obtain, from a discrete particle distribution of points, the corresponding density field using Mass-assigment schemes (MAS). Then, with the use of Fast Fourier Transforms (FFT), the underlying gravitational potential and its time derivative are computed. To compute the time derivative of the potential the following two approaches are used: an exact solution that takes into account the peculiar velocities, which is associated with a local and small-scale evolution of the hosted structures, and a linear approximation based on the linear evolution of the Large-Scale Structures (LSS). We point to solve the question about if the use of different MAS to compute the density field may induce larger differences in the other estimated field (potential and time derivative) that may lead to a spurious signal in the ISW effect. In particular, as the estimated time derivative of the potential is used to compute the ISW effect, a bad estimation of this field may affect the signal of the ISW temperature fluctuation. Another important aspect that will be treated here is comprised by the resolution effects in the estimation of the potential and time derivative fields. Although only first results are presented in this chapter, the most important results about the influence of the resolution on the estimated ISW signal will be treated in the next chapter. In addition, results from this chapter will give an insight of the order of magnitude of the temperatures and temperature ranges that the ISW effect should have in generic ΛCDM universes, i.e. this will be our theoretical expectation about this effect.

2.1 Mass-Assignment Schemes and Window Functions

In order to solve the Poisson's equation (given by Equation 1.11) with data from a cosmological simulation, given by the mass and positions of synthetic particles, it is necessary to smooth the mass distribution of particles in a grid. Such a grid surrounds the box of the cosmological simulation and its divided in cells. As the most common geometry for a cosmological simulation is a cubic box, the grid has the same number of cells per axis. The mass distribution of the particles from the cosmological simulation is smoothed and assigned to the cells of the grid. The most used Mass-Assignment Schemes (MAS) are the Nearest-Grid-Point (NGP), Cloud-In-Cell (CIC) and Triangular-Shaped-Cloud (TSC) [14].

For a given assigment scheme, it is possible to associate a *shape function*, which quantifies how a property (number, mass, charge, etc.) of a particle is distributed in the grid. After this process, the particle (or mass) distribution is not a mere sampling of the underlying density field, but a sample convolved with the *window function* of the assignment scheme [18], [14]. Let us consider N_p particles (as dark matter particles in a cosmological simulation) in a cubical simulation box with each side of length L. The particle number density is given by [18]:

$$n_0(\mathbf{x}) = \sum_{l=1}^{N_p} \delta^D(\mathbf{x} - \mathbf{x}_l), \tag{2.1}$$

with $\mathbf{x}_l$ the position of particle l. The mass density field is given by the multiplication of Equation 2.1 times the mass m_l of each particle. In our case, the individual masses for each particle are the same, $m_l = m \,\forall\, l$, then:

$$\rho(\mathbf{x}) = m \sum_{l=1}^{N_p} \delta^D(\mathbf{x} - \mathbf{x}_l). \tag{2.2}$$

Then, the mass assignment in the grid can be formulated by the convolution:

$$\rho_g(\mathbf{x}) = \int_V \mathrm{d}^3x' \, \rho(\mathbf{x}') \, W(\mathbf{x} - \mathbf{x}'), \tag{2.3}$$

where $W(\mathbf{x})$ is the window function that quantifies how much mass density is assigned to a grid point at $\mathbf{x}$ from a density distribution at $\mathbf{x}'$. Sampling the continuous mass density

$\rho(\mathbf{x})$ by a regular grid with N cells per axis (for a total of N^3 cells in the whole cube of side-length L), we obtain:

$$\rho_g(\mathbf{x}_{ijk}) = \int_V \mathrm{d}^3x \, \rho(\mathbf{x}') \, W(\mathbf{x}_{ijk} - \mathbf{x}'), \tag{2.4}$$

where the subscripts ijk stands for the triplet of integer indices that characterizes the position of each cell in each direction x, y, z, respectively. This means that the position of a given cell in the x axis is given by $x_i = i\, L/N = iH$ and in the three directions the vector is given by:

$$\mathbf{x}_{ijk} = \left(i\,\frac{L}{N}, j\,\frac{L}{N}, k\,\frac{L}{N}\right) = H\,(i, j, k)\,, \tag{2.5}$$

where $H = L/N$ is the length of the sides of each cell. The sampled density contrast is

$$\delta_g(\mathbf{x}_{ijk}) = \frac{\rho_g(\mathbf{x}_{ijk})}{\overline{\rho}} - 1; \text{ with } \overline{\rho} = \frac{N_p m}{V_{\text{Sim}}}, \tag{2.6}$$

where $V_{\text{Sim}} = L^3$. This discretized density field is then given by the convolution of the real density contrast and the window function:

$$\delta_g(\mathbf{x}) = [\delta * W]\,(\mathbf{x}). \tag{2.7}$$

The discretized values of the density contrast in the grid are represented by $\delta_g(\mathbf{x})$ which is the field used to compute the following quantities, needed to infer the Integrated Sachs-Wolfe effect. As we will show in section 2.2 , it is necessary to perform a Fourier transform to Equation 2.7, and the density contrast values in the grid will have the following expression:

$$\delta_g(\mathbf{k}) = \delta(\mathbf{k})\, W(\mathbf{k}), \tag{2.8}$$

where by easiness with the notation, all quantities in Fourier space differ from their representation in coordinate space only in the functional dependence, in other words, $\delta_g(\mathbf{x})$ is the representation in coordinate-space of the density contrast function δ_g while $\delta_g(\mathbf{k})$ is the same function δ_g represented in Fourier-space. The same convention applies for all the quantities that we work with henceforth.

Now, we are going to talk about the window function in a general way, in other words, for any MAS such as the aformentioned NGP, CIC and TSC. We have used the CIC and TSC MASs.

From the distribution of points representing any physical quantity, in our case mass, we may obtain the density field as in Equation 1.5. In this work, these points were obtained from data of N-body cosmological simulations or from the reconstruction of the density field of observational data using the Halo Based Method. As in both cases what we obtain is a set of point particles, each one in a given point of the space and with given mass, it is necessary to smooth the density mass distribution with the help of a MAS in a grid. Depending on the choosen scheme the distribution of mass in the grid could be interpreted in different ways, as shown in [14] and [18].

2.1.1 **NGP**

In the Nearest Grid Point (NGP), the mass of each particle is assigned to the nearest grid point, and the number density changes discontinuously when particles cross cell boundaries [18]. In Figure 2.1 it is shown a sketch of a grid in 2 dimensions with one particle. A particle has a position marked with an ×, and all its mass will be assigned to its nearest grid point (with position marked with the blue point), as indicated by the arrow.

In one dimension, the window function for the NGP is proportional to a top-hat function:

$$W_{\text{NGP}}(x) = \begin{cases} 1/H & \text{if} \quad x < H \\ 1/(2H) & \text{if} \quad x = H \\ 0 & \text{otherwise} \end{cases} \tag{2.9}$$

The Fourier transform of the top-hat function is a sinc function, then, for the NGP assignment scheme, we have:

$$W_{\text{NGP}}(k) = \frac{\sin\left(Hk/2\right)}{Hk/2} = \text{sinc}\left(\frac{Hk}{2}\right) = \text{sinc}\left(\frac{\pi k}{2k_N}\right), \tag{2.10}$$

where $k_N = \pi/H$ is the Nyquist frequency.

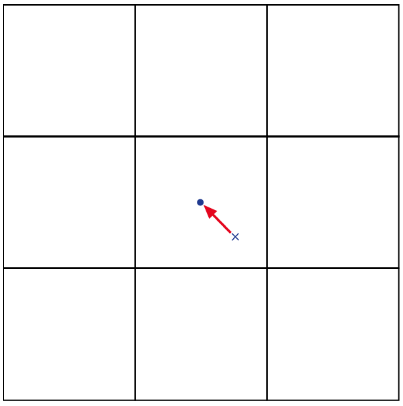

Figure 2.1: Nearest Grid Point assignment scheme: The particle's position is marked with ×, while the position of the grid-point is given by the blue point. All the mass of the particle will be assigned to such grid point, as indicated by the arrow.

2.1.2 CIC

The Cloud-In-Cell (CIC) assignment scheme is the first order distribution scheme which uniformly distributes the particle with a top-hat spreading function [18]. This means that each particle is assumed to have the same shape and size as the cell in which the particles is contained, as shown in Figure 2.2. Given that the particle is not assumed as a point-particle anymore but with a defined shape, this particele will not be contained only in the cell that encloses it, but the it will be “shared” by the neighbouring cells, allowing that the mass of the particles will be distributed and a smoother density field may be achieved compared with the density field obtained with the NGP scheme.

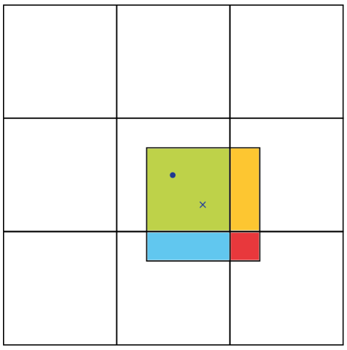

Figure 2.2: Cloud-In-Cell (CIC) mass assigment scheme. The particles is shown as a cross ($\times$), while the cell in which the particle is contained has its centre in the blue point. In the CIC, the assumed shape of the particle is an square of the same size as the grid cell. Given the fact that the particle is not completely centered with respect to the container cell, the square of the particles overlaps the neighbouring cells. This overlaping means that the mass of the particle is distributed in the neighbouring cells.

The CIC mass assignment scheme may be developed from the window function which in the case of a 1-dimensional CIC is given by the following expression [14], [18]:

$$W_{\text{CIC}}(x) = \begin{cases} 1 - |x|/H & \text{si} \quad x \leq H \\ 0 & \text{si} \quad x > H, \end{cases} \tag{2.11}$$

with $H = L/N$ is, again as the cell size. The Fourier Transfom of the window function is given by:

$$W_{\text{CIC}}(k) = W^2_{\text{NGP}}(k) = \text{sinc}^2\left(\frac{\pi k}{2k_N}\right). \tag{2.12}$$

2.1.3 TSC

The Triangular-Shaped-Cloud (TSC) assignment scheme, is a second order distribution scheme, with a window function given by the following expression in one dimension:

$$W_{\text{TSC}}(x) = \begin{cases} \frac{3}{4} - \left(\frac{|x|}{H}\right)^2 & \text{if} \quad |x| \leq \frac{H}{2} \\ \frac{1}{2}\left(\frac{3}{2} - \frac{|x|}{H}\right)^2 & \text{if} \quad \frac{H}{2} < |x| \leq \frac{3H}{2} \\ 0 & \text{otherwise} \end{cases} \tag{2.13}$$

The Fourier transform is given by:

$$W_{\text{TSC}}(k) = W^3_{\text{NGP}}(k) = \text{sinc}^3\left(\frac{\pi k}{2k_{Ny}}\right). \tag{2.14}$$

2.1.4 3D Window function

In 3 dimensions, the window function for all the three assigment schemes shown before takes the following expression (in both, coordinates and Fourier space):

$$W(x) = W(x_1)\, W(x_2)\, W(x_3), \tag{2.15}$$

$$W(k) = W(k_1)\, W(k_2)\, W(k_3). \tag{2.16}$$

Once the window function is known, it is possible to find the enclosed mass in the cells $m_g(x)$ as:

$$m_g(x) = m_p W(x). \tag{2.17}$$

being m_p the mass of each particle. With that, it is possible to find the density fluctuation field $\delta_g(x)$ given by Equation 2.7 in the cells.

2.2 Estimation of $\Phi(\mathbf{x})$ and $\dot{\Phi}(\mathbf{x})$ as Grid Quantities

Once the density field is computed, it is possible to solve the Poisson equation to find the gravitational potential. In comoving coordinates, we have:

$$\nabla^2\Phi(\mathbf{x}, t) = 4\pi G\overline{\rho}(t)\delta(\mathbf{x}, t)a^2(t). \tag{2.18}$$

To solve this equation, we have made use of Fourier methods. A Fourier Transform allows to rewrite Equation 2.18 in Fourier space as follows [33]:

$$\begin{aligned} \Phi(\mathbf{k}, t) &= -4\pi G\overline{\rho}(t)a^2(t)k^{-2}\delta(\mathbf{k}, t) \\ &= -\frac{3}{2}\Omega_{m,0}H_0^2k^{-2}\frac{\delta(\mathbf{k}, t)}{a(t)}. \end{aligned} \tag{2.19}$$

In this point, it is necessary to take into account that the value of $\delta(\mathbf{k}, t)$ is not precisely the Fourier Transform of the density field $\delta_g(x)$ found with the MAS. When computing the Fourier Transform of the density field in the grid, $\delta_g(x)$, it is necessary to perform a deconvolution with the Fourier Transform of the window function to obtain the true value $\delta(\mathbf{k}, t)$ as in Equation 2.7. Making use of the properties of the Fourier transform, such deconvolution may become a division, as follows [33]:

$$\delta(\mathbf{k}) = \frac{\delta_g(\mathbf{k})}{W(\mathbf{k})}, \tag{2.20}$$

where $\delta_g(\mathbf{k})$ is the Fourier transform of the density field in the grid, $\delta_g(\mathbf{x})$, and $W(\mathbf{k})$ is given by Equation 2.16. In general, the deconvolution with the window function will depend on the MAS. This deconvolved field is the one used to estimate the gravitational potential in Equation 2.19, which may be differentiated respect to time to obtain [33]:

$$\dot{\Phi}(\mathbf{k}, t) = \frac{3}{2}\Omega_{m,0} H_0^2 k^{-2} \left[\frac{H(t)}{a(t)} \delta(\mathbf{k}, t) - \frac{\dot{\delta}(\mathbf{k}, t)}{a(t)} \right], \tag{2.21}$$

where its has been taken into account that $\overline{\rho}(t)a^3(t) = \overline{\rho}_0$ is the mean matter density in the Universe at present time and is time independent. H_0 is the present value of the Hubble parameter ($H(t) = \dot{a}\, a^{-1}$) and $\Omega_{m,0}$ is the present value of the matter density parameter. $\Omega_{m,0}$ can be related with $\overline{\rho}_0$ by means of $\Omega_{m,0}\, \rho_{c,0} = \overline{\rho}_0$, been $\rho_{c,0}$ the present value of the critical density, $\rho_{c,0} = (3H_0^2)/(8\pi G)$.

From here, two approaches can be studied in order to find the value of $\dot{\delta}(\mathbf{k}, t)$. First, is what we call the exact solution of $\dot{\Phi}(\mathbf{k}, t)$ which is obtained using the continuity equation in the Fourier space in order to relate the density field $\dot{\delta}(\mathbf{k}, t)$ with the Fourier transform of the momentum field $\mathbf{p}(\mathbf{k}, t)$ [33]. The continuity equation can be written as:

$$\nabla \cdot [1 + \delta(\mathbf{x}, t)]\, \mathbf{v}_p(\mathbf{x}, t) = -a(t)\dot{\delta}(\mathbf{x}, t), \tag{2.22}$$

where $\mathbf{v}_p(\mathbf{x}, t)$. Defining the pseudo-peculiar momentum field:

$$\mathbf{p}(\mathbf{x}, t) = [1 + \delta(\mathbf{x}, t)]\, \mathbf{v}_p(\mathbf{x}, t). \tag{2.23}$$

Replacing in the continuity equation and taking a Fourier transform:

$$\mathrm{i}\mathbf{k} \cdot \mathbf{p}(\mathbf{k}, t) = -a(t)\dot{\delta}(\mathbf{k}, t). \tag{2.24}$$

It is important to take into account that our convention with the Fourier transform has sign -1 in the exponential to the Fourier transform from position space to k-space, while sign

+1 for the inverse transform. Replacing $\dot{\delta}(\mathbf{k},t)$ from Equation 2.24 into Equation 2.21 and with our convention in the signs of the Fourier transform, we obtain [33], [6]:

$$\dot{\Phi}(\mathbf{k},t) = \frac{3}{2}\Omega_{m,0}H_0^2k^{-2}\left[\frac{H(t)}{a(t)}\delta(\mathbf{k},t) + \frac{\mathrm{i}\mathbf{k}\cdot\mathbf{p}(\mathbf{k},t)}{a(t)}\right]. \tag{2.25}$$

Once the density field $\delta(\mathbf{k},t)$ and momentum field $\mathbf{p}(\mathbf{k},t)$ in Fourier space are known, it is possible to compute $\dot{\Phi}(\mathbf{k},t)$. With an Inverse Fourier Tranform (IFT) in Equation 2.25, one can find the integrand of Equation 1.16.

In the case in which the momentum field $\mathbf{p}(\mathbf{k},t)$ cannot be known, it is possible to perform and approximation, associated with the linear growth of the structure to estimate the analytical form of $\dot{\Phi}(\mathbf{k},t)$. From linear theory, it is possible to find the linear growth factor $D(t)$, which gives the time evolution of the density contrast as $\dot{\delta}(\mathbf{k},t) = \dot{D}(t)\delta(\mathbf{k},z=0)$ [6]. This linear growth factor $D(t)$ is obtained when solving the equation that describes the evolution of the density field $\delta(x)$ in the linear regime (Equation 1.12), i.e., assuming that such fluctuations are first-order perturbations in the mean density field $\overline{\rho}$ of the Universe.

Substituting $\dot{\delta}(\mathbf{k},t)$ in Equation 2.21 and using the definition for the linear growth rate $f(t) = \mathrm{d}\ln D(t)/\mathrm{d}\ln a$, yields [6]:

$$\dot{\Phi}(\mathbf{k},t) = \frac{3}{2}H_0^2k^{-2}\Omega_{m,0}\frac{H(t)}{a(t)}\delta(\mathbf{k},t)[1-f(t)]. \tag{2.26}$$

This equation uses only information from the density field. This can also be seen as assuming that the velocity field is related with the density field by the linear approximation [6]:

$$\begin{aligned}\mathbf{p}(\mathbf{k},t) &= \mathrm{i}\dot{\delta}(\mathbf{k},t)\frac{\mathbf{k}}{k^2}\\ &\approx \mathrm{i}f(t)\,\delta(\mathbf{k},t)H(t)\frac{\mathbf{k}}{k^2}.\end{aligned} \tag{2.27}$$

In the linear approximation, the density field δ determines completely the potential field Φ and its time derivative $\dot{\Phi}$. Then, overdense regions ($\delta > 0$) correspond to regions with positive values of $\dot{\Phi}$ and underdense regions ($\delta < 0$) are related to negative values of $\dot{\Phi}$ [6]. Both Equation 2.25 and Equation 2.26 may be used as integrands in Equation 1.16 allowing to make a comparison between the contribution of the ISW effect in both regimes.

Finally, an important annotation that must be taken into account when computing the $\dot{\Phi}$ field with Equation 2.25 and Equation 2.26. Those equations come from the Poisson equation in Fourier space (Equation 2.19) in which to perform the Fourier tranform, we assume that the laplacian operator in Fourier space can be expressed as $\nabla^2 \rightarrow -k^2$, or more formally, when solving the Poisson equation through a Green function, we obtain that the continuous Green function of a point source is given by:

$$G(k) = -\frac{1}{k^2}. \tag{2.28}$$

This is the same k^{-2} present in Equation 2.25 and Equation 2.26. This result is valid only when solving these equations in the continuum case; as we have a discrete grid, the Green function changes according to the discretization and is given by [14]:

$$G_d(k) = -\frac{(H/2)^2}{\sin^2(k_x H/2) + \sin^2(k_y H/2) + \sin^2(k_z H/2)}. \tag{2.29}$$

This new form for the Green function does not depend on the MAS. So, in Equation 2.25 and Equation 2.26 instead of using the typical form of the Fourier transform of the laplacian operator, or the Green function given by Equation 2.28, it is necessary to use Equation 2.29. According to this requirement, the exact solution to $\dot{\Phi}$ given by Equation 2.25 becomes:

$$\dot{\Phi}(\mathbf{k}, t) = -\frac{3}{2}\Omega_{m,0}H_0^2\, G_d(k) \left[\frac{H(t)}{a(t)}\delta(\mathbf{k}, t) + \frac{\mathrm{i}\mathbf{k}\cdot\mathbf{p}(\mathbf{k}, t)}{a(t)}\right], \tag{2.30}$$

and the solution in the linear approximation given by Equation 2.26 becomes:

$$\dot{\Phi}(\mathbf{k}, t) = -\frac{3}{2}\Omega_{m,0}H_0^2\, G_d(k)\, \frac{H(t)}{a(t)}\delta(\mathbf{k}, t)[1 - f(t)]. \tag{2.31}$$

Those two final equations are the ones we are going to use of now in ahead in our work and we will refer to those them frequently. Now, we are going to show the way each equation of $\dot{\Phi}$ was modeled.

2.2.1 Exact Solution of $\dot{\Phi}$

With the aim to compute the exact solution of Equation 2.30 in the grid, it is also necessary to know the velocity field or the momentum field of the particles in the simulation and perform an assigment scheme to this velocity or momentum field. The pseudo-momentum field can be estimated as shown before as [33]:

$$\mathbf{p} = [1 + \delta(\mathbf{x})]\, \mathbf{u}(\mathbf{x}) a(t), \tag{2.32}$$

where $\mathbf{u}(\mathbf{x}) = \mathbf{v}_p/a$ is the comoving peculiar velocity field. Using Equation 2.6, it is possible to write:

$$\begin{aligned} 1+\delta(\mathbf{x}) &= \frac{1}{N_p}\frac{V_{\text{Sim}}}{V_W}\sum_l^{N_p} W(\mathbf{x}_{ijk}-\mathbf{x}_l) \\ &= \frac{N^3}{N_p}\sum_l^{N_p} W(\mathbf{x}_{ijk}-\mathbf{x}_l), \end{aligned} \tag{2.33}$$

with $N^3 = V_{\text{Sim}}/V_W$ as the total number of cells in the grid. Then, the right hand side of Equation 2.32 can be written as:

$$\left[(1+\delta)\mathbf{u}\right](\mathbf{x}) = \frac{V_{\text{Sim}}}{N_p}\sum_l^{N_p} \delta^D(\mathbf{x}-\mathbf{x})\mathbf{u}_l. \tag{2.34}$$

Convolving with the window function of the mass-assignment scheme, the mesh-averaged quantity becomes:

$$\left[(1+\delta)\mathbf{u}\right](\mathbf{x}_{ijk}) = \frac{1}{N_p}\frac{V_{\text{Sim}}}{V_W}\sum_l^{N_p} \mathbf{u}_l\, W(\mathbf{x}_{ijk}-\mathbf{x}_l). \tag{2.35}$$

Then, the estimated pseudo-momentum field will be given by:

$$\mathbf{p}(\mathbf{x}_{ijk}) = a(t)\frac{N^3}{N_p}\sum_l^{N_p} \mathbf{u}_l W(\mathbf{x}_{ijk}-\mathbf{x}_l). \tag{2.36}$$

This is the pseudo-momentum field used in Equation 2.30. As it is also necessary to know the wavenumber-vector k, we used the FFTW convention to define them, due to the fact that this is the library we use to perform Fourier Transforms. For example, in the direction of the x-axis, with N_x cells in this axis, one has that the k vector has the form[1]:

$$k_x(i) = \begin{cases} \frac{2\pi}{L} i & \text{if} \quad i = 0, \cdots, \frac{N_x-1}{2}, \\ \frac{2\pi}{L}(-N_x+i) & \text{if} \quad i = \frac{N_x}{2}, \cdots, N_x-1. \end{cases} \tag{2.37}$$

And in the same way for the y and z axes, and taking into account a 0-based indexing for the index i, which is related with the position of the cell in the grid. Using Equation 2.36 and Equation 2.37, it is possible to find the value of $\dot{\Phi}(\mathbf{k})$ in each cell. Performing an inverse Fourier transform allows to find the value in the position space $\dot{\Phi}(\mathbf{x})$.

---

[1] see `http://pauli.uni-muenster.de/tp/fileadmin/lehre/NumMethoden/SoSe10/Skript/Ordening.pdf`

2.2.2 Solution of $\dot{\Phi}$ in Linear Theory

To estimate the solution in the linear regime from Equation 2.31, it is necessary to know the functional form of the linear growth rate $f(t)$. In this work, we take a functional form used in cosmological simulations, that has the form [4], [22]:

$$f(\Omega_m(a)) = \Omega_m^{5/9}(a); \text{ with } \Omega_m(a) = \frac{\Omega_{m,0}}{\Omega_{m,0} + \Omega_{\Lambda,0}a^3}. \tag{2.38}$$

Given that until now the computation of the fields $\delta(\mathbf{x})$, $\Phi(\mathbf{x})$ and $\dot{\Phi}(\mathbf{x})$ was performed over a grid, it is necessary to compute an interpolation of the function $\dot{\Phi}(\mathbf{x})$ with the goal to obtain a continuous function that may be integrated numerically and then, estimate the values of ΔT through Equation 1.16. It is worth to say that the codes used in this analysis where programmed in the ANSI C programming language with the help of the FFTW[1] library to perform the Fast Fourier Transform routines and the GSL[2] library to compute the interpolation and numerical integration. In the following, we will show the results obtained from the computation of the aformentioned fields in some cosmological simulations.

2.3 Fields from $400h^{-1}$Mpc Simulation

With the aim to study the ISW effect, we have used a N-Body cosmological simulation that consists of 512^3 particles inside a cubic box of $400h^{-1}$Mpc of length per axis in a ΛCDM cosmological model with $\Omega_{\Lambda,0} = 0.742$, $\Omega_{m,0} = 0.258$, $\Omega_{b,0} = 0.04$, $\sigma_8 = 0.796$, present value of Hubble's constant $H_0 = 100\,h$ km s^{-1} Mpc^{-1} and Hubble's parameter $h = 0.72$. These conditions were chosen according to a WMAP5 cosmology. The internal units of this simulation were chosen to make the unit of mass equal to $1 \times 10^{10}\ h^{-1}M_{\odot}$, the unit of length as $1\ h^{-1}$Mpc in order to make the gravitational constant equal to $G = 43.0071$ internal units and the unit of time as 3.08568×10^{19} s.

Only one snapshot of the cosmological simulation, with redshift $z = 0$, was taken to make the analysis of the ISW imprint due to the structures formed by the particles in the simulation at that time. Only this snapshot was used because when studying the ISW imprint due to the reconstructed density field of the 2MASS survey, the observational data used has an spherical shape with nearly $300\,h^{-1}$ Mpc of diameter and the imprint from the density field from the observational data will be compared with that obtained from this cosmological simulation. The results shown in the following come from the analysis of the simulation particles enclosed in a regular grid with a resolution of 512 cells per axis.

---

[1] `http://fftw.org/`

[2] `https://www.gnu.org/software/gsl/`

2.3.1 **Density Field**

To obtain the values of $\dot{\Phi}(\mathbf{x})$ it is necessary to know the density field from the spatial distribution of particles in the simulation. For that reason, a CIC MAS was implemented in order to compute the density field $\delta(\mathbf{x})$ as shown in section 2.1. The CIC MAS was performed with 512 cells per axis (a total of 512^3 cells), allowing to obtain the smooth density field shown in Figure 2.3, where all plots represent slices of $10\,h^{-1}$Mpc of thickness along the z axis of the simulation box. It is worth to say that in the following figures we factored out the Hubble parameter h without replacing its value; that is the way we will show all the results from now on. In Figure 2.3, we can see a yellow background that corresponds to such regions in the particle distribution with lower densities (possibly void regions), while the red filamentary structure show us the clustering of particles and, then, of matter.

2.3.2 **Gravitational Potential Field**

As we will need to solve the Poisson equation in the Fourier space, as seen in Equation 2.19, it is necessary to perform the Fourier transform of the estimated density field $\delta_g(\mathbf{x}_{ijk})$ (as shown in Equation 2.6). In order to find the field δ_d (where d stands form discrete) it is necessary to deconvolve the field δ_g with the Fourier transform of the window function, as given by Equation 2.20. In this case, this equation becomes:

$$\delta_d(\mathbf{k}, t) = \frac{\delta_g(\mathbf{k})}{W_{\text{CIC}}(\mathbf{k})}. \tag{2.39}$$

After knowing the correct value for the discrete density field in the Fourier space $\delta_d(\mathbf{k})$, we can use this field in Equation 2.19, implement the Inverse Fourier Transform and obtain the gravitational potential in position space $\Phi(\mathbf{x})$ as shown in Figure 2.4. As expected, negative regions in the gravitational potential coincide with overdense regions of the density maps in Figure 2.3. Here, we may notice that as the Poisson equation (Equation 2.19) also has a continuum Green function given by the k^{-2} factor; to be consistent we used insted the discrete form, as shown in Equation 2.29.

An unexpected behaviour was found in the potential maps of Figure 2.4, and corresponds to a larger region in which the gravitational potential is very positive (associated with a possible void). This feature is present in all maps of this simulation and may be due to the fact that this cosmological simulation box is not large enough and it will not be possible to resolve the largest modes, i.e. the greatest structures. This feature will be present also in the maps of $\dot{\Phi}(\mathbf{x})$. If the density field is smoothed in a way that small scales are completely suppresed and only the largest of the scales are seen in the density

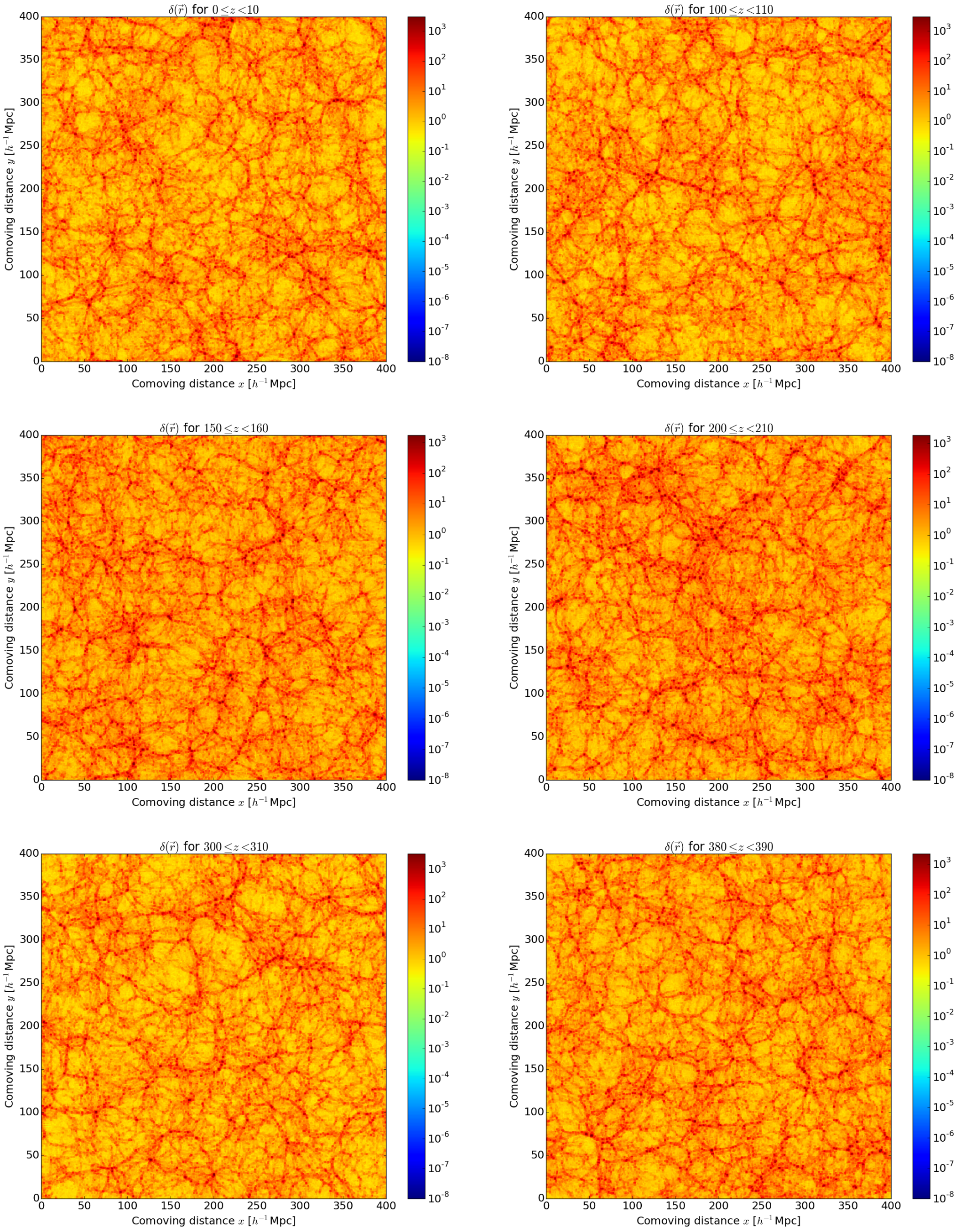

Figure 2.3: Density field maps from the cosmological simulation in logarithmic scale $\log_{10}[\delta(\mathbf{x})+1]$. Slices at different depths, from top to bottom and left to right: $0-10\,h^{-1}$ Mpc, $100-110\,h^{-1}$ Mpc, $150-160\,h^{-1}$ Mpc, $200-210\,h^{-1}$ Mpc, $300-310\,h^{-1}$ Mpc and $380-390\,h^{-1}$ Mpc.

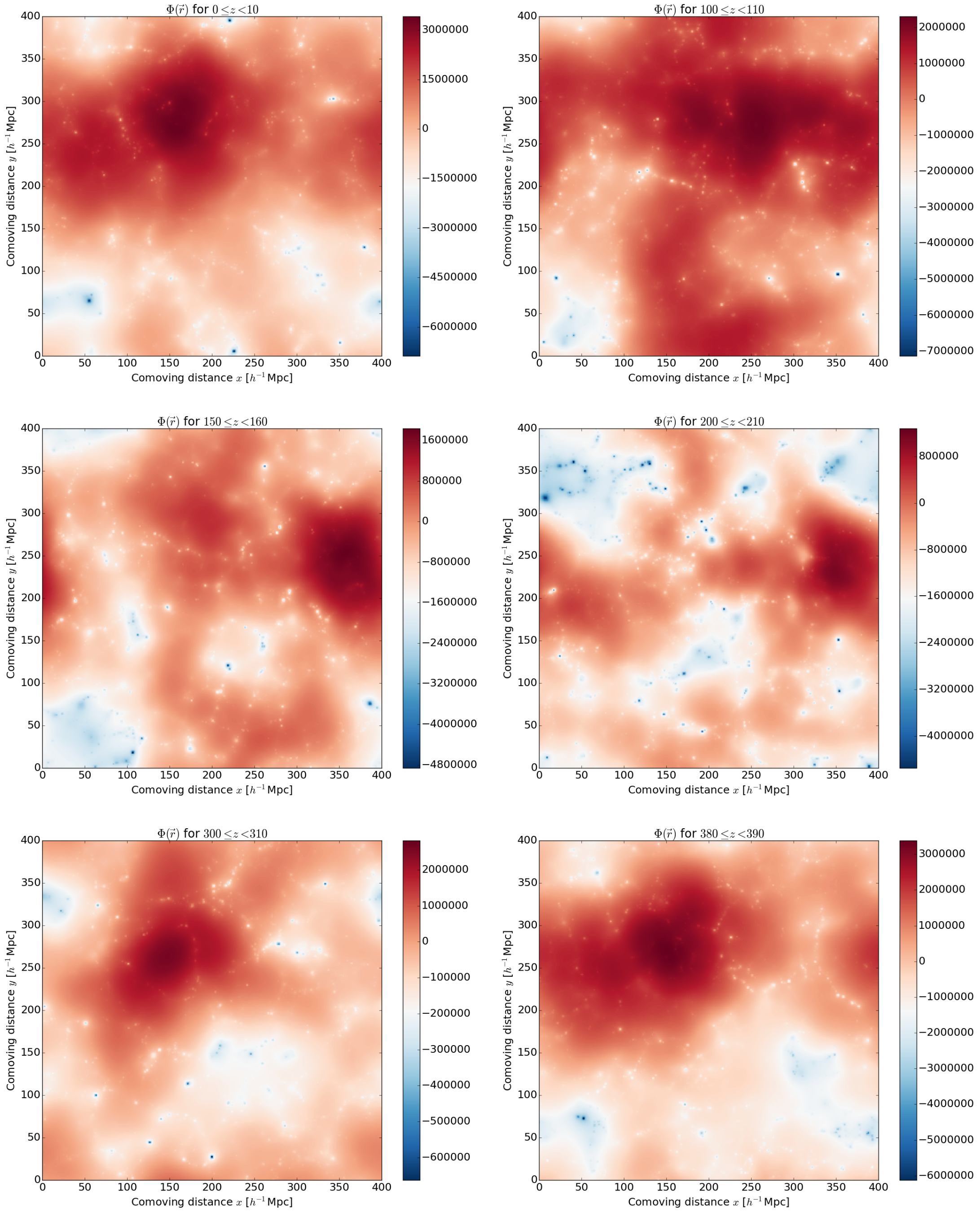

Figure 2.4: Gravitational potential maps for the cosmological simulation data. Slices at different depths, from top to bottom and left to right: $0-10\,h^{-1}$ Mpc, $100-110\,h^{-1}$ Mpc, $150-160\,h^{-1}$ Mpc, $200-210\,h^{-1}$ Mpc, $300-310\,h^{-1}$ Mpc and $380-390\,h^{-1}$ Mpc. Units $[\Phi] = h^{-2}\,\mathrm{Mpc}\ \left(10^{10} M_{\odot}\right)^{-1}\ \left(3.08568 \times 10^{19}\ \mathrm{s}\right)^{-2}$.

field map, a kind of underdense region will be present in such regions with the most positive values of the gravitational potential, giving as a result such kind of large scale mode features.

2.3.3 Time Derivative of Gravitational Potential

As aformentioned, the time derivative of the gravitational potential $\dot{\Phi}$ is computed also in the Fourier space in two regimes, an exact solution given by Equation 2.30 and the linear approximation from Equation 2.31, in which the linear growth rate function $f(t)$ is associated with the linear growth of the Large-Scale Structures (LSS). In the next two subsections the results for both regimes are shown.

2.3.3.1 Exact solution to $\dot{\Phi}$ and pseudo-momentum field

In order to use the exact approach of Equation 2.30, one needs to know the velocity field or the momentum field of the particles in the simulation. The velocity field is also assigned to the regular grid using the CIC MAS, according to Equation 2.36 and taking into account that $\mathbf{u}_l$ refers to the velocity of a certain particle l, while $\mathbf{p}(\mathbf{x}_{ijk})$ is the accumulated pseudo-momentum field in the cell of the grid that contains the lth particle. With this pseudo-momentum field and the convention for the wavenumber vector $\mathbf{k}$ of FFTW, according to Equation 2.37, we computed $\dot{\Phi}(\mathbf{k}, t)$ as given in Equation 2.30 for each cell in the grid. Again, with an Inverse Fourier Transform we found the values in the position space, $\dot{\Phi}(\mathbf{x})$. The corresponding maps in the exact solution regime are shown at the left panels in Figure 2.5.

The expected behaviour of $\dot{\Phi}(\mathbf{x})$ is that positive values are associated with the overdense regions of Figure 2.3, while negative values of $\dot{\Phi}(\mathbf{x})$ are associated with underdense regions. This is because overdense regions are contained in a deeper gravitational potential wells ($\Phi < 0$) and such potential will loose depth due to the expansion of the Universe, which is associated with $\dot{\Phi} > 0$. On the other hand, underdense regions with $\Phi > 0$ will have $\dot{\Phi} < 0$ so the potential well will evolve to have smaller values. As can be seen when comparing the left and right panels of Figure 2.4 both panels show the described behaviour: the most negative values of $\Phi(\mathbf{x})$, in which the structures should be hosted, are consistent with the most positive values of $\dot{\Phi}(\mathbf{x})$. In the case of the positive values of $\Phi(\mathbf{x})$, the $\dot{\Phi}(\mathbf{x})$ field has negative values but very near to zero.

In these maps it is also possible to see the behaviour found in the maps of gravitational potential, i.e. a large region that may be associated with an underdense region, due to the fact explained before: this cosmological simulation box is not large enough and it will

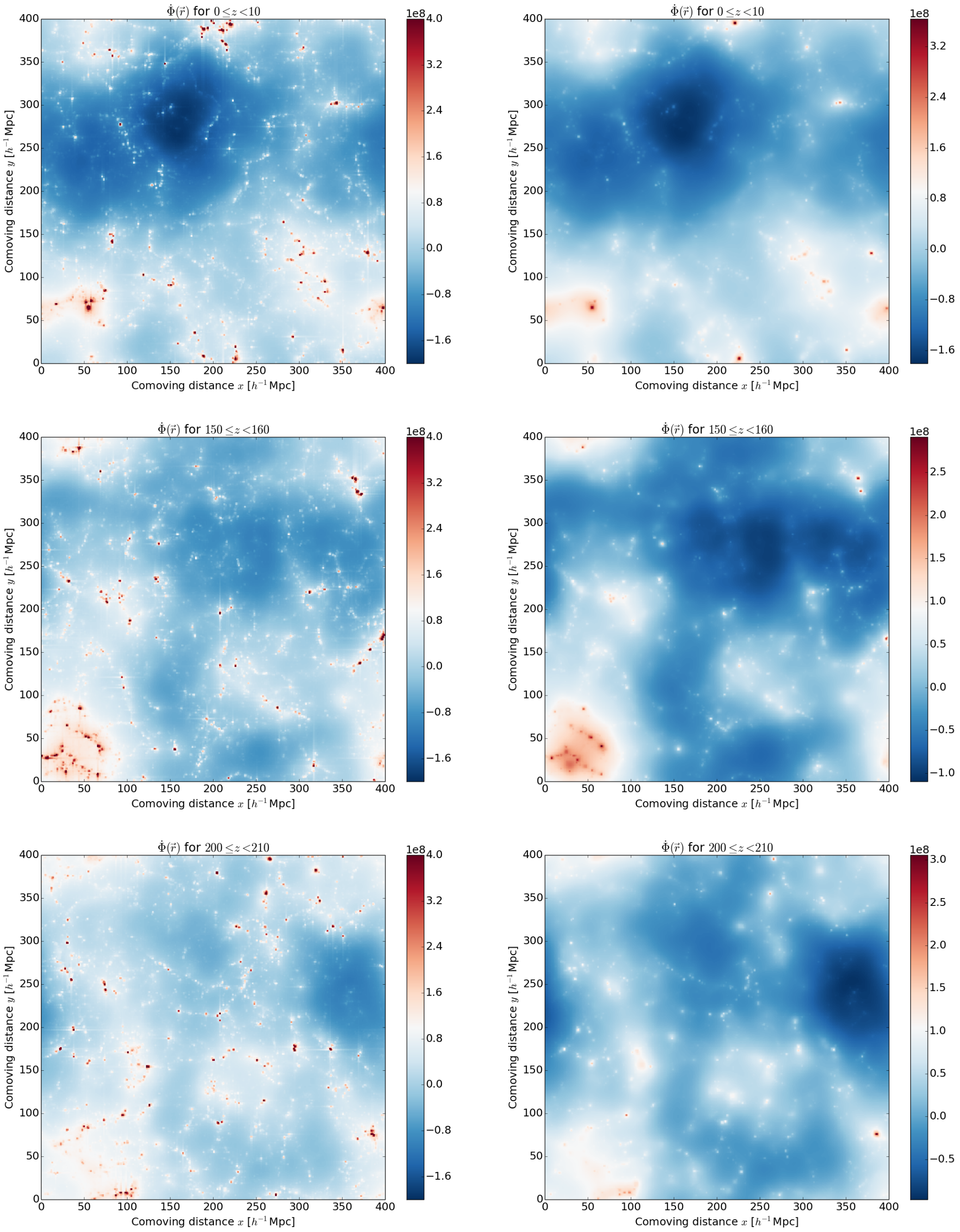

Figure 2.5: Maps of the time derivative of gravitational potential for the cosmological simulation data. Left panels correspond to the exact solution and right panels to the linear approximation. Slices at different depths, from top to bottom: $0 - 10\,h^{-1}$ Mpc, $150 - 160\,h^{-1}$ Mpc and $200 - 210\,h^{-1}$ Mpc. Units $[\dot{\Phi}(\mathbf{x})] = h^{-2}\,\mathrm{Mpc}\ \left(10^{10} M_{\odot}\right)^{-1}\ \left(3.08568 \times 10^{19}\ \mathrm{s}\right)^{-3}$.

not be possible to resolve the largest modes. Although in this case this behaviour is not as notable as in the maps of potential or as in the maps of the linear approximation of $\dot{\Phi}$, as we will see later. We verified that this large mode feature is not a defect or a mistake on the estimation of the gravitational potential or its time derivative. For this aim we performed different tests:

- First, we used a uniform distribution of points in a simulation box of the same size and applied the MAS to find the associated density constrast field. Then, the FFT algorithm was applied to compute Φ and $\dot{\Phi}$, expecting also uniform fields, which were indeed found by us.

- Second, a distribution of points distributed according to a 3-dimensional Hernquist profile were placed at the center of the simulation box. Again, we obtained the expected behaviour which consist in a very deep ($\Phi < 0$) gravitational potential at the center with the same extension as the Hernquist sphere, while the surroundings have basically a potential $\Phi \leq 0$. In the case of the $\dot{\Phi}$ at the position of the Hernquist sphere, we found $\dot{\Phi} > 0$ in the center, indicating that the potential well will loose depth, and positive but very near to zero values at the surroundings.

- Third, a set of 7 Hernquist spheres were placed in the following way: one at the center of the box, two were placed along the x-axis at positions $(L/4, L/2, L/2)$ and $(3L/4, L/2, L/2)$. The other four spheres were placed in a similar way but at the y or z axes. Once again, we obtained the expected result, which consist in 7 haloes with $\Phi < 0$ (and $\dot{\Phi} > 0$) while the surroundings of the spheres presented $\Phi \leq 0$ ($\dot{\Phi} \geq 0$).

- As a final test, we used the gravitational potential computed directly from the simulation with Gadget code. We then performed a CIC MAS to this gravitational potential and notice that the same large scale mode appeared in this solution, so it is an intrinsic feature of this cosmological simulation.

According to those tests, we clarified that no mistakes were made in the estimation of both fields; instead of that, the larger mode is, as aformentioned, a feature due the the small size of the simulation box which did not allow to resolve the largest modes, or the largest of the structures in this particular box.

2.3.3.2 Linear regime solution to $\dot{\Phi}_l(\mathbf{x})$

For the linear approximation, the functional form of the linear growth rate $f(t)$ given by Equation 2.38 was used in Equation 2.31 in order to compare the results and the order of magnitude for the induced temperature fluctuations ΔT with those obtained in the exact solution. In the majority of works about the ISW effect in a ΛCDM universe, this linear approximation is used, so we perform such a comparison to study the discrepancy between the signal amplitudes of the ISW effect in ΛCDM in both regimes (linear approximation and exact solution) and determine if the linear approximation is indeed a good approximation to estimate the temperature fluctuation signal.

Once the values in Equation 2.31 are known for the grid, an Inverse Fast Fourier Transform is performed, allowing us to obtain the values of the rate of change of the gravitational potential in each cell, i.e. to find $\dot{\Phi}_l(\mathbf{x})$ in this approximation. The corresponding maps of this linear approximation are shown at the right panels of Figure 2.5.

The structure of the maps obtained in the linear approximation looks similar to those obtained in the regime of the exact solution. It is worth to say that a difference between both maps is the order of magnitude of the values; it can be seen that the range of values with the exact solution can achieve the $\dot{\Phi} \sim \pm 2 \times 10^9$ internal units, which corresponds to a difference of one order of magnitude larger than the values obtained with the linear approximation (right panels). In the case of the exact solution and by visualization issues, the range of values is constrained to $-2 \times 10^8 < \dot{\Phi} < 4 \times 10^8$ internal units to make a proper comparison with the values obtained in the linear approximation. This issue is due to the smoothing introduced by the linear approximation, because in the exact solution the influence of the peculiar velocities will introduce a local evolution of the smallest structures, making that local gravitational potentials that host small structures would have a contribution to the $\dot{\Phi}$ field and those maps can resolve the smallest structures as can be noticed in the left panels of Figure 2.5. In the case of the linear approximation, the structures are supposed to grow in the linear regime valid only for the largest structures. Then the features associated to small scale structures cannot be resolved in this approximation. This linear regime will induce a lost of information at the smallest structures, averaging the overall behaviour of the larger structures.

2.3.4 Comparison between CIC and TSC Mass Assignment Schemes

Only for this simulation we performed a comparison between CIC and TSC mass assignment schemes (MAS) in order to quantify how the MAS would affect the estimation of the ISW effect. This is done with the aim to solve the question of the influence of the

MAS in the estimation of the ISW effect, while searching for some notable differences in the estimated underlying fields (density and time derivative of the potential) and find if such differences introduce spurious signals in the temperature fluctuation field that may originate the discrepancies associated with the detectability of the late ISW effect, as aforementioned in the Introduction chapter . For this reason, we compared the density contrast field and the time derivative of the gravitational potential obtained in both MAS. The comparison of the temperature in both MAS will be shown in the next chapter.

2.3.4.1 **Effect of the MAS in the estimation of the Density Contrast field $\delta(\mathbf{x})$**

When comparing the values of $\delta(\mathbf{x})$ obtained with CIC and TSC cell by cell, we can see in the left panel of Figure 2.6 that the values from TSC are below those obtained with CIC. This is an expected behaviour due to the fact that TSC being a second order scheme, allows to obtain a smoother field than the obtained with the CIC MAS. The x-axis shows the index which refers to the internal index of each cell in C-order. It is worth to say that we would expect two curves instead of the distribution of points shown in this figure, but this distribution is due to the fact that the internal C-order for the index of the cells does not imply a physical relationship between adjacent indeces. At the right panel of the same figure, we took the value obtained through CIC for a cell (in the x-axis) and compare it with the value from TSC for the same cell (in the y-axis). This figure shows a black line indicating $\delta_{CIC} = \delta_{TSC}$. However, TSC gives a lower values of $\delta\mathbf{x}$ than CIC, the slope of the data is smaller than 1. A color code according to the value of k (the Fourier reciprocal of position) is given in order to see if there is any correlation with the scale. Data has been sorted according to ascendent values of k. A gradient can be noticed, with the largest values of k at the smallest values of $\delta\mathbf{x}$, decreasing k with larger $\delta\mathbf{x}$, but at the largest values of density contrast it can be noticed a mix between the larger values of k with some smaller values of k.

When we compare the relative difference $|\delta(\mathbf{x})_{TSC} - \delta(\mathbf{x})_{CIC}|/|\delta(\mathbf{x})_{CIC}|$ as a function of the scale k, shown in the right panel of Figure 2.7, it looks like no clear dependence on the scale can be seen; for the majority of scales, the scatter in the values of $|\delta(\mathbf{x})_{TSC} - \delta(\mathbf{x})_{CIC}|/|\delta(\mathbf{x})_{CIC}|$ is very large. Only for the largest of the scales ($k << 1\ h\ Mpc^{-1}$) and the smallest ones ($k \sim 7\ h\ Mpc^{-1}$) in our simulation box the scatter of values looks to be below 10. This is supported by the left panel of the same figure, in which we compare $\delta(\mathbf{x})_{TSC} - \delta(\mathbf{x})_{CIC}$ as a function of the scale k. In this second figure, it is also shown a narrower dispersion of the values of $\delta(\mathbf{x})_{TSC} - \delta(\mathbf{x})_{CIC}$ for the largest scales ($k << 1\ h\ Mpc^{-1}$) and for the smallest scales ($k \sim 7\ h\ Mpc^{-1}$). For the other scales, the scatter is again so large that no kind of correlation seems to arise from this comparison.

This large scatter in the difference and relative difference may be due to the different ways in which each MAS distributes the total mass in small and median scales, but at larger scales all the mass is distributed in a very similar way.

2.3.4.2 Effect of the MAS in the estimation of the $\dot{\Phi}(\mathbf{x})$ field in the exact solution

The same experiment was performed for $\dot{\Phi}(\mathbf{x})$ in both regimes: the exact solution and in the linear approximation. In this section we will show the results obtained in the exact solution. When performing a comparison of the values of $\dot{\Phi}(\mathbf{x})$ obtained after applying Fourier Transforms to the density field found with CIC and TSC, we can see in the left panel of Figure 2.8 that the values associated to the TSC MAS are very similar, but still below, to those associated with the CIC. This is evident in the statistical properties of the distribution of each MAS, as shown in the left part of Table 2.1. In this table, it can be noticed that the ranges of values of $\dot{\Phi}(\mathbf{x})$ in the exact solution span 18 orders of magnitude (taking the maximum values minus the minimum values), and although the means have different values, they have an order of magnitude $\sim 1 \times 10^{-9}$, which is negligible compared with the complete range of values; so the means of the distribution according to the MAS are very similar, but the standard deviation associated to the CIC MAS seems to be slightly larger. Furthermore, the range of values of the CIC is also slightly larger than the associated to the TSC MAS, although the TSC have a larger upper limit.

When performing a comparison of $\dot{\Phi}(\mathbf{x})$ from CIC in the x-axis and the obtained from TSC in the y-axis, we can see that this comparison has a behaviour very near to a straight line $\dot{\Phi}_{CIC} = \dot{\Phi}_{TSC}$, as shown in the left panel of Figure 2.9. This tells us again that both schemes gives us similar values for $\dot{\Phi}$. At the behaviour according to the scale k it can be noticed that the larger values of k are more near to zero, but at the extremes the gradient in k is not so evident.

The comparisons associated with the physical scale k give analogous results than in the case of the density contrast, as can be seen in the left panel of Figure 2.10 for the comparison of the difference $\dot{\Phi}_{TSC} - \dot{\Phi}_{CIC}$ vs k. Again, at the larger scales, associated with the lower values of k, the difference between the values of TSC and CIC tends to zero, allowing us to say that in both schemes, in a general view, the evolution of the gravitational potential is very similar, although at lower scales the gravitational potential of the substructures may have a different evolution. This difference at middle and small scales may be due to the fact that, as TSC tends to present a smoother density field than the obtained through a CIC, the gravitational potential wells obtained from TSC data will also tend to be smoother than the obtained with CIC, because TSC spreads the mass more

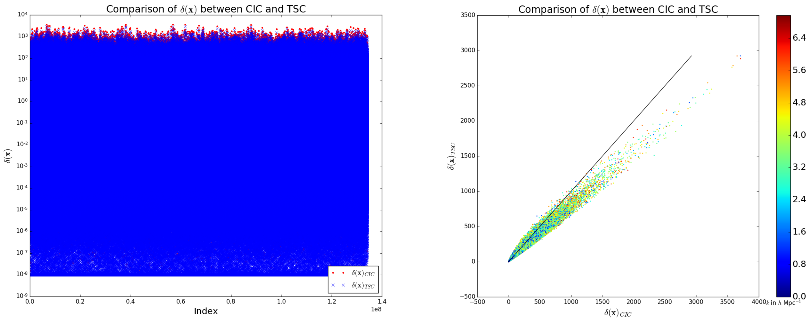

Figure 2.6: At the left panel, density contrast field obtained through the CIC MAS (red points) compared with the values from the TSC MAS (blue points) as function of the index (maximum index is 512^3). TSC values are below the CIC values, as expected. Right panel shows the density contrast field obtained through the CIC MAS (x-axis) compared with the values from the TSC MAS (y-axis) cell by cell. The black line represents $\delta_{CIC} = \delta_{TSC}$. As the data tuples have an slope lesser than 1, we can assure again that TSC values are below CIC values for each cell. The colour code is given by the associated value of k in h Mpc^{-1}.

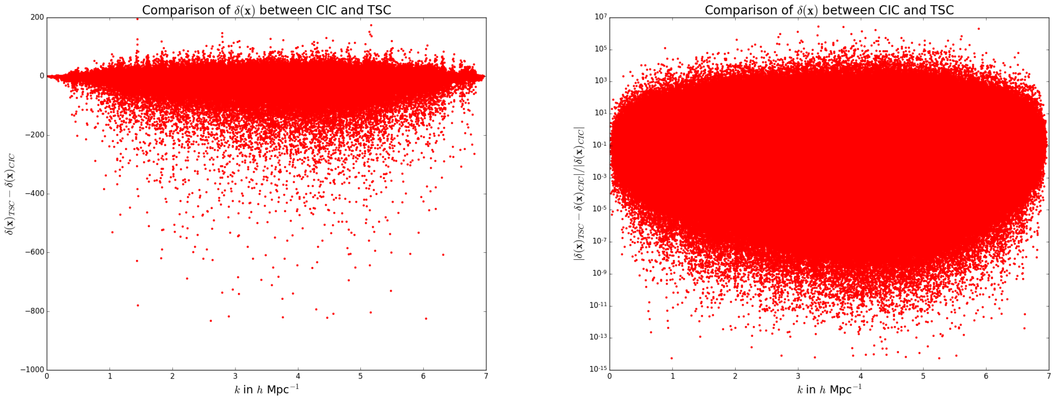

Figure 2.7: Difference $\delta(\mathbf{x})_{TSC} - \delta(\mathbf{x})_{CIC}$ and relative difference $|\delta(\mathbf{x})_{TSC} - \delta(\mathbf{x})_{CIC}|/|\delta(\mathbf{x})_{CIC}|$ as function of the scale k between both assigment schemes. Either the difference and the relative difference show a smaller scattering for the largest and smallest of the scales; in other case, the scatter is so large that no correlation seems to arise from those comparisons.

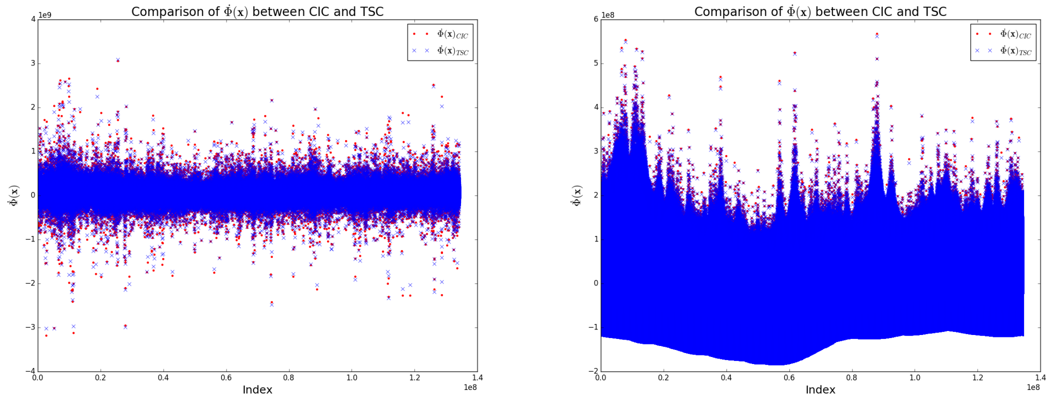

Figure 2.8: $\dot{\Phi}(\mathbf{x})$ field obtained with the exact solution (left panel) and linear approximation (right panel) through the CIC MAS (red points) compared with the values from the TSC MAS (blue points) cell by cell. TSC values have a very similar behaviour than the the CIC values, but still some below. The x-axis corresponds to the index of each cell.

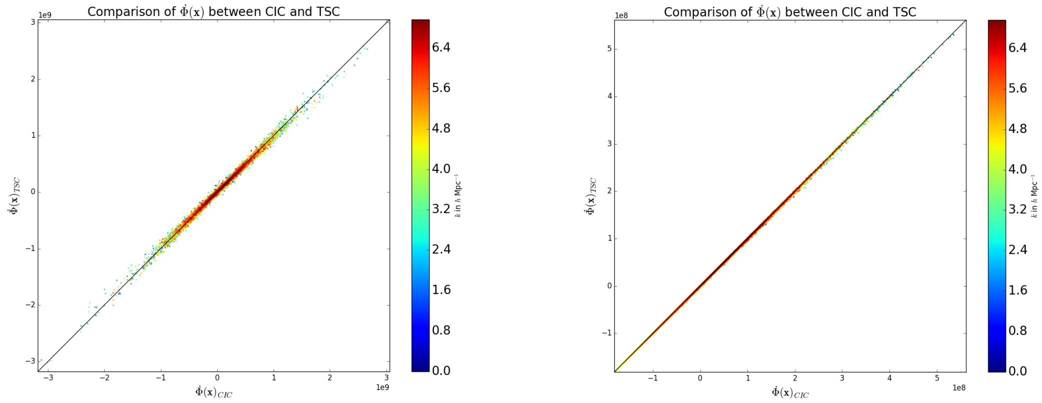

Figure 2.9: $\dot{\Phi}(\mathbf{x})$ field obtained through the CIC MAS (x-axis) compared with the values from the TSC MAS (y-axis) cell by cell. The black line representes a $y = x$ line with slope 1. Left panel is associated with the exact solution, while the right one to the linear approximation. Data tuples have an slope very near to 1, so both schemes give similar values of $\dot{\Phi}(\mathbf{x})$. The colour code is given by the associated value of k in h Mpc^{-1}.

into the neighbouring cells. In other words, with a CIC scheme we will obtain a structure that comprises fewer cells than with TSC, making the structure more overdense, and then, a deeper gravitational potential will be obtained if compared with the potential obtained through TSC. As the potential well is deeper with CIC, its time evolution will also be affected. An analogous behaviour will be obtained with underdense regions, which will be more underdense in CIC than in TSC.

The relative difference $|\dot{\Phi}(\mathbf{x})_{TSC} - \dot{\Phi}(\mathbf{x})_{CIC}|/|\dot{\Phi}(\mathbf{x})_{CIC}|$ presented in the left panel of Figure 2.11 shows an analogous behaviour than the previous figure, because it continues to be near to zero for the largest physical scales, while at mean and small scales the scattering is larger.

Statistical property	$\dot{\Phi}_{Exact}$	$\dot{\Phi}_{Linear}$
$\overline{\dot{\Phi}}_{CIC}$	1.2796×10^{-9}	3.7825×10^{-9}
σ_{CIC}	6.2566×10^{7}	6.075838×10^{7}
$b_{1,CIC}$	-0.3658	-0.2382
$g_{2,CIC}$	1.7601	-0.685
Minimum value in CIC	-3.1777×10^{9}	-1.8129×10^{8}
Maximum value in CIC	3.0571×10^{9}	5.6847×10^{8}
$\overline{\dot{\Phi}}_{TSC}$	3.5506×10^{-9}	2.9295×10^{-8}
σ_{TSC}	6.2551×10^{7}	6.075835×10^{7}
$b_{1,TSC}$	-0.3676	-0.2382
$g_{2,TSC}$	1.6434	-0.0317
Minimum value in TSC	-3.0236×10^{9}	-1.8148×10^{8}
Maximum value in TSC	3.0938×10^{9}	5.6178×10^{8}

Table 2.1: Table with the statistical properties for the distribution of $\dot{\Phi}$ for both MAS. A comparison between both solution regimes is also shown.

2.3.4.3 **Effect of the MAS in the estimation of the $\dot{\Phi}(\mathrm{x})$ field in the linear approximation**

When performing a comparison of the values of $\dot{\Phi}(\mathbf{x})$ obtained in the linear regime with CIC and TSC, we can see in the right panel of Figure 2.8 that the behaviour is very similar to that of the exact solution (left panel of the same figure), i.e. both, CIC and TSC give very similar values to $\dot{\Phi}(\mathbf{x})$ with a very small visual difference in which TSC gives the “smaller” values. This is supported again with the statistical properties summarized in the right part of Table 2.1 in which the behaviour is very similar than the described above

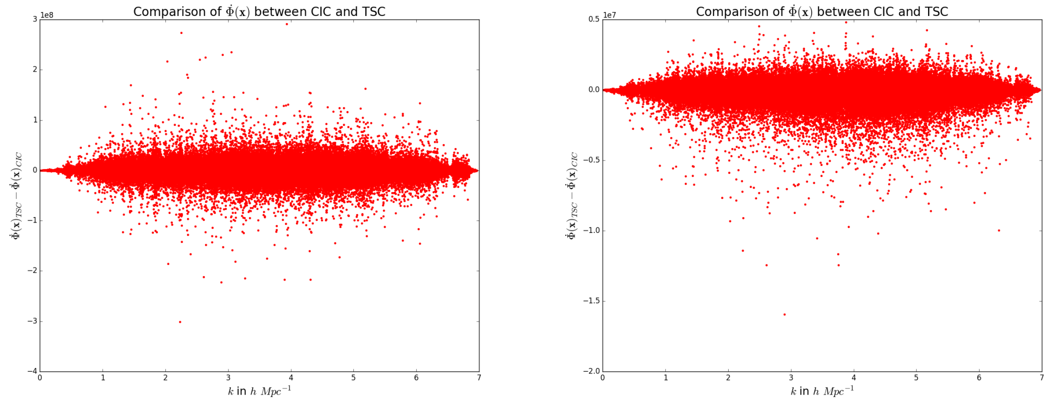

Figure 2.10: Difference between two schemes $\dot{\Phi}(\mathbf{x})_{TSC} - \dot{\Phi}(\mathbf{x})_{CIC}$ as function of the physical scale k. Left panel corresponds to the exact solution and right panel to the linear approximation. It is possible to see that at the largest scales (smallest values of k) the difference between both schemes tends to zero, allowing us to say that in both schemes, in a general view, the evolution of the gravitational potential is very similar, although at middle and some smaller scales the gravitational potential of the substructures may have a different evolution. At the smallest of the scales, this difference also tends to zero.

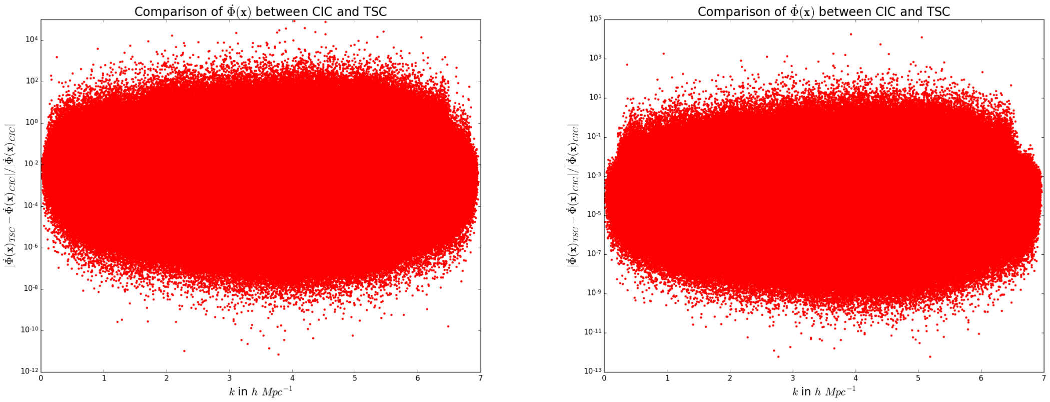

Figure 2.11: Relative difference $|\dot{\Phi}(\mathbf{x})_{TSC} - \dot{\Phi}(\mathbf{x})_{CIC}|/|\dot{\Phi}(\mathbf{x})_{CIC}|$ between both assigment schemes. Left panel is associated to exact solution and righ panel to the lienar approximation. The relative difference is very low at the largest scales (smallest values of k), while becoming more scattered at middle and some small scales. This great relative difference may be due to the different ways in which each MAS distributes the total mass in small and median scales, but at larger scales all the mass is distributed in a very similar way. For the smallest scales in the box, this relative difference also tends to zero.

for the exact solution, i.e. the larger range of values makes the means negligible and very similar and the standard deviation associated to the distribution of values from CIC is slightly larger than the standard deviation for TSC. The total range of values of the CIC MAS is also slightly larger than those from TSC.

Again, a comparison of $\dot{\Phi}(\mathbf{x})$ from CIC in the x-axis and the obtained from TSC in the y-axis, is shown in the right panel of Figure 2.9. This figure shows again that both MAS gives us similar values for $\dot{\Phi}$, because the slope of the data is very near to the slope of a straight line $\dot{\Phi}_{CIC} = \dot{\Phi}_{TSC}$ and the behaviour according to the values of k is similar to the case of the exact solution.

As in the previous case for the solution of $\dot{\Phi}$ in the exact regime, the comparisons associated with the physical scale k are shown in the right panel of Figure 2.10 for $\dot{\Phi}_{TSC} - \dot{\Phi}_{CIC}$ vs k. This figure is very similar to the left panel of the same figure, differing only in a lower range of values for the y axis, so the same conclusions of subsubsection 2.3.4.2 can be infered to the linear approximation. These same conclusions hold also in the case of the relative difference $|\dot{\Phi}(\mathbf{x})_{TSC} - \dot{\Phi}(\mathbf{x})_{CIC}|/|\dot{\Phi}(\mathbf{x})_{CIC}|$ presented in the right panel of Figure 2.11, i.e. at the largest physical scales the relative difference is very close to zero, while at mean and small scales the scattering is larger. From all these results, we may conclude that for both regimes for the solution of $\dot{\Phi}$, both CIC and TSC will give very similar results at the larger scales, which are the scales we are interested in order to study the ISW effect. This issue also tells us that the MAS used to estimate the underlying density field and the $\dot{\Phi}$ field will not affect the estimation of the ISW signal, as we will show in the next chapter.

2.4 Fields from MultiDark 1 (MDR1) Simulation

In order to make another estimate of the ISW signal in a ΛCDM cosmology, we used the *MultiDark 1* [1] cosmological simulation [29], which has the following characteristics, also corresponding to a WMAP5 cosmology: 2048^3 particles in a cubic box of $1h^{-1}$Gpc of side, $\Omega_{\Lambda,0} = 0.73$, $\Omega_{m,0} = 0.27$, $\Omega_{b,0} = 0.0469$, $\sigma_8 = 0.82$, and a Hubble parameter $h = 0.70$. We have also used the snapshot at redshift $z = 0$.

The data obtained from the CosmoSim web corresponding to the *MultiDark 1* (MDR1) simulation is the density fluctuation field $\delta(\mathbf{x})$ computed through a CIC mass-assignment scheme with 512^3 cells and smoothed with a gaussian filter. With this density field we performed the same procedure described for the simulation of $400h^{-1}$Mpc in order to compute the gravitational potential and its time derivative. Taking into account that the data obtained from CosmoSim does not have information about the velocity field, it is necessary to use the linear approximation to the growth of structures of Equation 2.31, with the functional form of the linear growth rate $f(t)$ shown in Equation 2.38.

The importance of a simulation with such scales is because as the ISW effect is due to the density field of large-scale structure, it is important to have a density field large enough to make a comparison of the signal amplitude of the actual ISW effect, in which the photons of the CMB have pass through a large amount of large-scale structures. Furthermore, the use of this simulation provides results that may be comparable to those of previous works as [6] and [33].

2.4.1 Density Field

The density field, as downloaded from the CosmoSim web is shown in Figure 2.12. The slices in this figure were built in a similar way as in the previous simulation, that means, projections along the z-axis with $10\,h^{-1}$Mpc of thickness. Again, it can be seen the overdense regions corresponding to red zones and voids to yellow zones, forming the filamentary structures.

2.4.2 Gravitational Potential Field

In order to compute the gravitational potential with Fourier methods, we need to know the density field δ in the Fourier space. In this case not only a deconvolution with the window function is necessary (as shown in Equation 2.20) but also a deconvolution with the

---

[1] `https://www.cosmosim.org/cms/simulations/multidark-project/mdr1/`

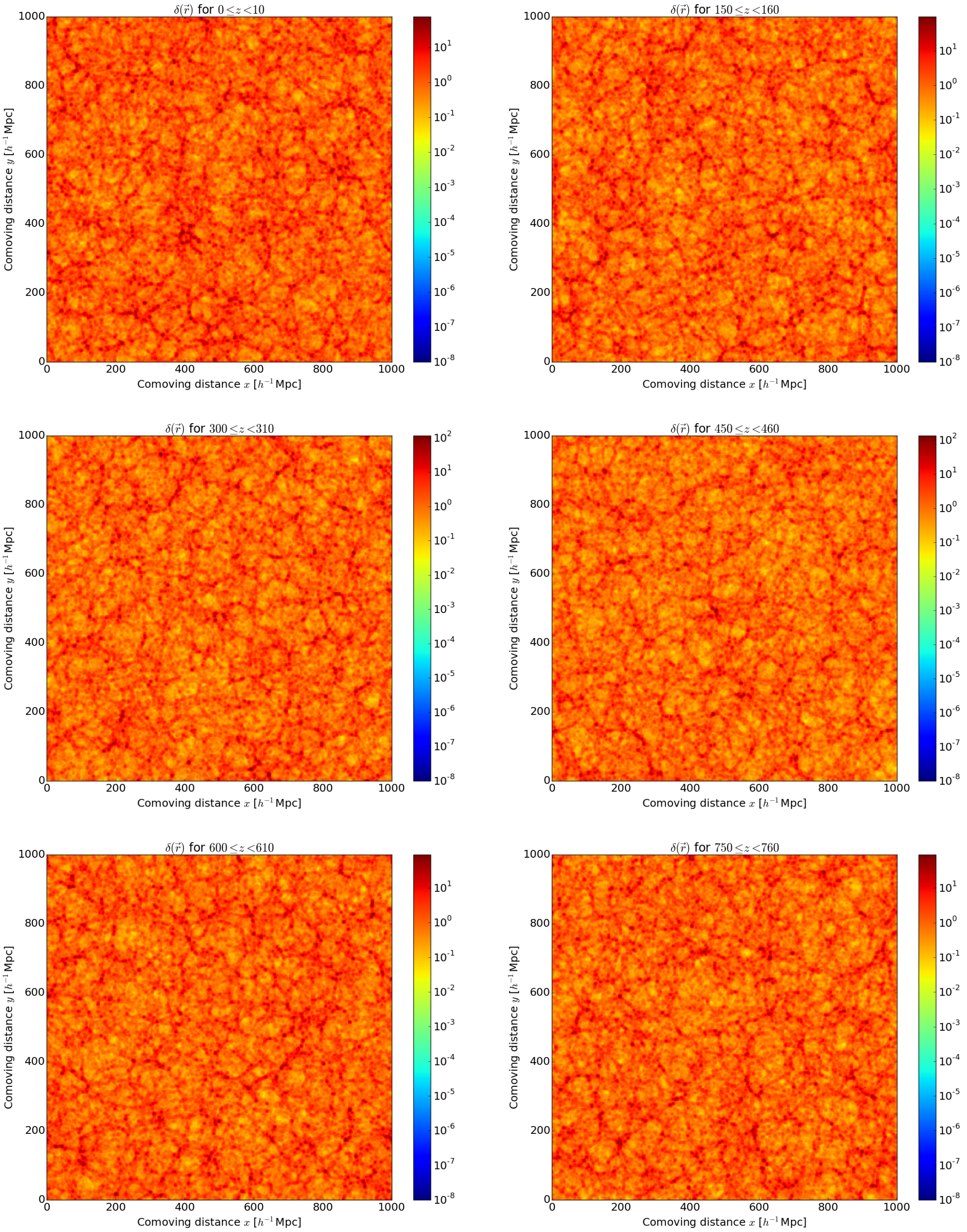

Figure 2.12: Maps of the density field of *Multidark 1* simulation in logarithmic scale: $\log_{10}[\delta(\mathbf{x})+1]$. Slices at different depths; from top to bottom and left to right: $0-10\,h^{-1}$ Mpc, $150-160\,h^{-1}$ Mpc, $300-310\,h^{-1}$ Mpc, $450-460\,h^{-1}$ Mpc, $600-610\,h^{-1}$ Mpc and $750-760\,h^{-1}$ Mpc.

Fourier transform of the smoothing gaussian filter function. Then, the total deconvolution becomes:

$$\delta(\mathbf{k}, t) = \frac{\delta_g(\mathbf{k})}{W_{\mathrm{CIC}}(\mathbf{k}) \times e^{\mathrm{i}\mu k - \frac{1}{2}\sigma^2 k^2}}, \tag{2.40}$$

where, in the deconvolution of the gaussian function, we have used the values: $\mu = 0$ and $\sigma = H$ with H the size of each cell, according to the values of the simulation. With this deconvolution performed, it is possible to compute the corresponding Fourier transforms in order to know the gravitational potential. The maps of the gravitational potential are shown in the left panel of Figure 2.13 for some chosen slices. From those maps it can be also seen the expected behaviour for the gravitational potential, that means, regions with negative values of Φ correspond to overdense regions in the density field maps, while positive values of Φ are associated with voids. Here it is also possible to observe a large region with $\Phi > 0$, which may be related with an underdense region. In this case, this large region is also a large mode (a large structure associated with a large underdensity) that may be not resolved due to the resolution of the the MAS and the Fourier transforms.

2.4.3 $\dot{\Phi}$ in Linear Regime

Using Equation 2.31, we compute the values of $\dot{\Phi}$ for the MDR1 simulation. In this case, we obtain the maps shown in the left panel of Figure 2.14 for $f(t)$ given by Equation 2.38. Again, we can see the expected behaviour for the values of $\dot{\Phi}$, which has the opposite sign than the potential. That implies that we also have the expected behaviour according to the density field: regions with positive values of $\dot{\Phi}$ are related with overdense regions, while regions with negative values of $\dot{\Phi}$ are associated with voids, as explained for the first simulation of $400h^{-1}$Mpc. Furthermore, the same large region that appears in the maps of Φ related with a large underdense regions can be seen here, and it is a feature due to the resolution used.

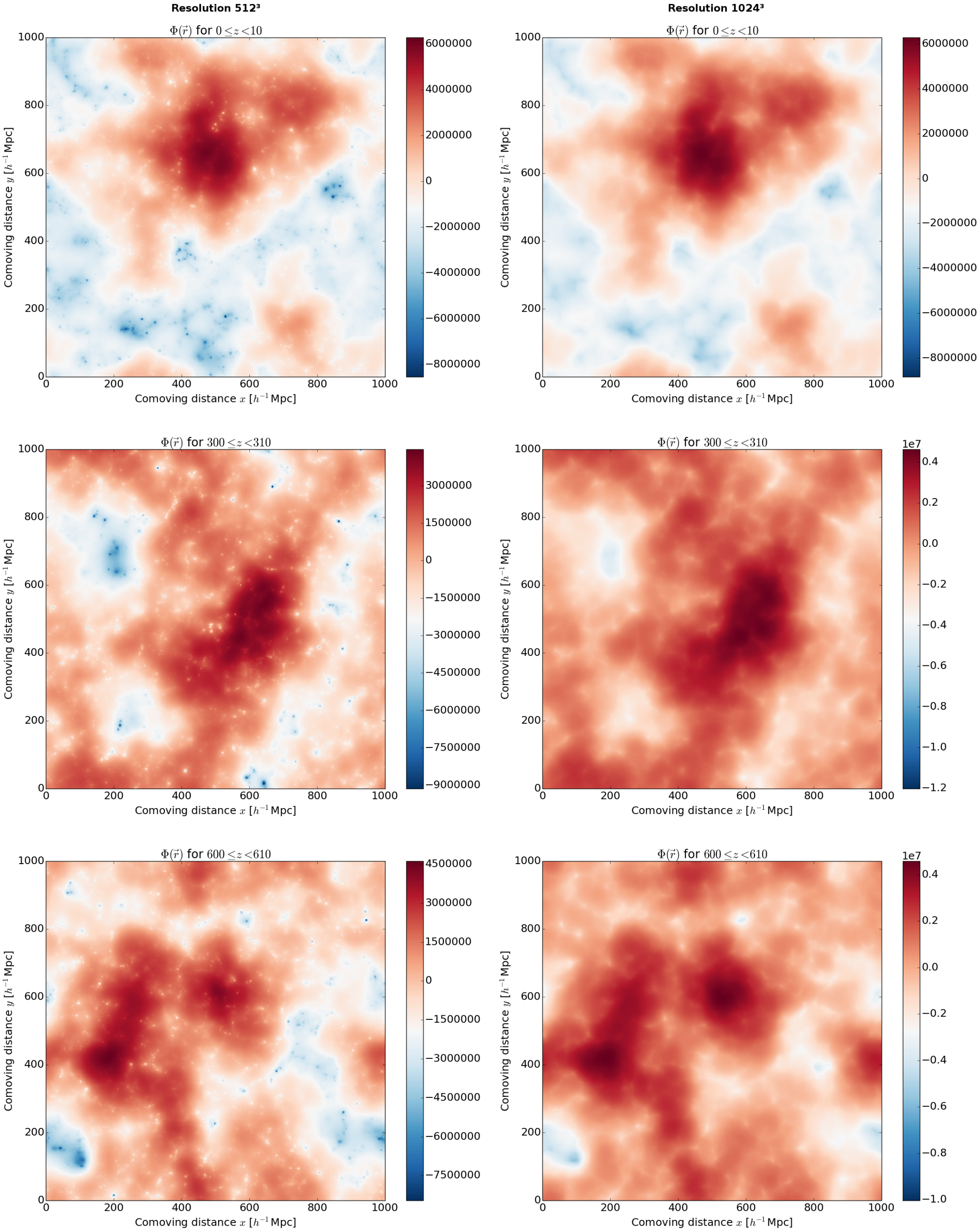

Figure 2.13: Gravitational potential maps for the *Multidark 1* simulation. Panels at the left side correspond to the resolution of 512^3 cells. At the right side, the maps correspond to the highest resolution of 1024^3 cells. From top to bottom : $0 - 10\,h^{-1}$ Mpc, $300 - 310\,h^{-1}$ Mpc and $600 - 610\,h^{-1}$ Mpc. Units $[\Phi] =$ Internal length^2 Internal time^{-2}.

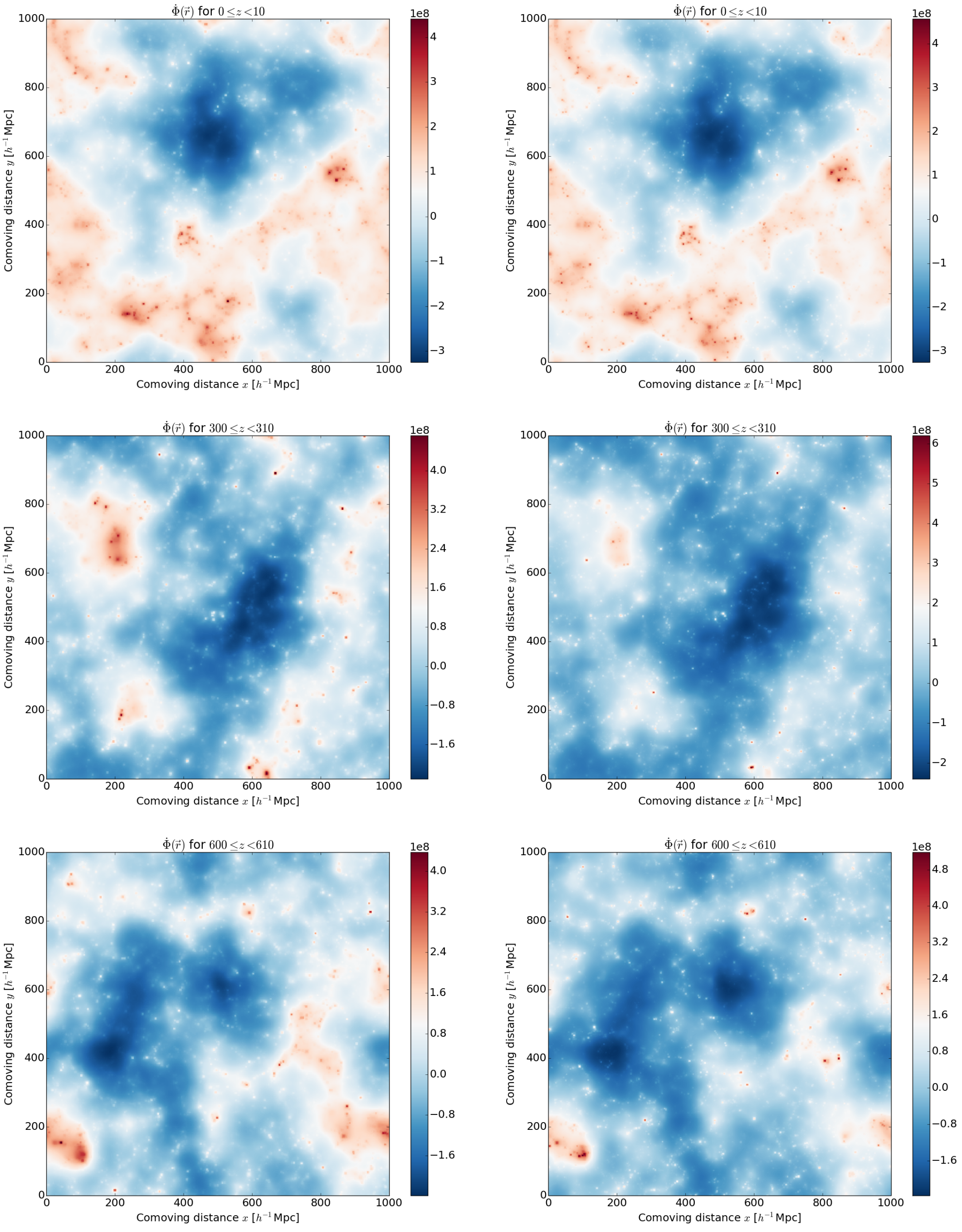

Figure 2.14: Maps of $\dot{\Phi}$ for the *Multidark 1* simulation in the linear regime. Panels at the left side correspond to the resolution of 512^3 cells. At the right side, the maps correspond to the highest resolution of 1024^3 cells. From top to bottom : $0 - 10\,h^{-1}$ Mpc, $300 - 310\,h^{-1}$ Mpc and $600 - 610\,h^{-1}$ Mpc. Units $[\dot{\Phi}]$ = Internal length^2 Internal time^{-3}.

2.5 Effects of Resolution in MDR1 Simulation

For MDR1 simulation, we also study the effects of the resolution in the estimation of the different fields and on the ISW effect. We use the same MDR1 simulation but a higher resolution of 1024 cells per axis was implemented to test the effects of the resolution on the reconstructed density field. The data obtained from the CosmoSim database is analogous as in the lower resolution case, i.e., what we obtain is the density field $\delta(\mathbf{x})$ obtained through a CIC MAS convolved with a gaussian smoothing kernel. So, to perform the Fourier transform algorithms it is necessary to apply again the corresponding deconvolution, given by Equation 2.40. In the following, we are going to see the maps obtained with our method.

2.5.1 Gravitational Potential Field for MDR1 $\times\ 1024^3$

After applying the Fourier transform algorithm with the complete deconvolution (Equation 2.40), the gravitational potential field maps obtained for this new resolution are shown in the right panel of Figure 2.13.

From this map, we see a slight difference in the structure of the maps, with a slight wider range of values for the resolution of 1024^3 cells; indeed it looks like the 512^3 resolution shows more smaller structures while the 1024^3 resolution looks smoother, but may be due to the fact that the color scales are a bit different. It would be interesting to determine the distribution of values for Φ and $\dot{\Phi}$ to see if the distribution for the lower resolution and the higher one are similar with at least similar means and standard deviations; due to our interest in the temperature field, such a comparison between distributions is done only for the temperature field, and as we will show in subsection 3.2.2. The distribution of temperatures for both resolutions have, up to normalization, the same behaviour. This allow us to conclude that resolution will not play an important role in the estimation of the ISW effect, although obviously will allow to evidence a more detailed structure alongside with a possible Rees-Sciama signal. This issue will be discussed in the next chapter.

2.5.2 $\dot{\Phi}$ in Linear Regime for MDR1 $\times\ 1024^3$

Applying the linear solution for $\dot{\Phi}$, we obtain the maps shown in the right panel of Figure 2.14.

Again, as in the case for Φ, there is no change in the structure of the field when changing the resolution. The only slight change is in the range of values that takes the $\dot{\Phi}$ field. We can assume that, according to this behaviour, the structure and ranges of values for the temperature fluctuation ΔT due to an ISW effect must be also unaffected when increasing the resolution for the MDR1 simulation. This is consistent with the results of chapter 3, in which it can be noticed that an increase in the resolution does not affect the estimated temperature fluctuation nor the fluctuation along the photon's path, i.e. the quantity $\mathrm{d}T/\mathrm{d}r$. For the ISW effect, a change in the resolution will not have a notable effect so any of the resolutions may be used, but a higher resolution may be desired in order to obtain a more detailed perspective of the temperature fluctuation induced by small scale structures, eg. the Rees-Sciama effect.

2.6 MultiDark-Planck (MDPL) Simulation

The last simulation used in this work is the *MultiDark-Planck* (MDPL)[1] simulation [19], which is an analogous project to MDR1 with more than 6 times higher mass resolution, using 3840^3 particles and with a Planck cosmology. The parameters of the simulation are the following: $\Omega_{\Lambda,0} = 0.6922885$, $\Omega_{m,0} = 0.307115$, $\Omega_{b,0} = 0.048206$, $h = 0.6777$, $n = 0.96$ and $\sigma_8 = 0.8228$. Due to the simulation's resolution and the availability of the velocity field, it is possible to resolve the smallest structures. This fact will allow not only to have a more detailed view of the underlying fields but also to obtain a contribution to the temperature fluctuation due to the smalles structures in the same way as the ISW effect, i.e. the Rees-Sciama effect. Besides, the large size of this simulation will allow to obtain and resolve very large structures, reducing the cosmic variance.

With this simulation, we will be able to use both regimes for the solution of $\dot{\Phi}$ in order to compare the two results. Due to the largest simulation box, those results will allow us to obtain a better estimation of an exact theoretical temperature amplitude for the ISW effect in a ΛCDM universe and make a detailed comparison with the amplitude obtained from the linear approximation, which is used in several works. If the difference between both amplitudes is small, the use of the linear approximation could give a good estimate of the ISW effect at the largest scales, but the use of the exact solution will bring more information about small-scale fluctuations.

For this simulation, a CIC MAS with a resolution of 1024^3 cells was also used in order to obtain both, the smooth density field δ and the velocity field to estimate the momentum field $\mathbf{p}$. As aformentioned, the importance of a simulation with such scales is because as the ISW effect is due to the density field from large-scale structures, and it is important to have a density field large enough to make a comparison of the signal amplitude of the actual ISW effect. Furthermore and as mentioned above a higher resolution is also

---

[1] `https://www.cosmosim.org/cms/simulations/mdpl/`

desirable because allows to resolve better the structures of the simulation. Although the resolution does not induce any effect on the estimation of the large-scale ISW signal, it has an important contribution to the estimation of the temperature fluctuation at smallest scales, especially in the case of the exact solution, that is also associated with the Rees-Sciama effect. The maps of the different fields for the MDPL simulation can be seen in the appendix, at chapter 7.

2.6.1 Density Field

In Figure 7.1 it is possible to see the maps of the density field from the structures in the MDPL simulation obtained through the CIC MAS. As before, the thickness of those slices is of $10\ h^{-1}$Mpc, and the depths are the same as shown for the MDR1 simulation. The color code is in the same logarithmic scale, with redder regions representing overdensities.

2.6.2 Gravitational Potential Field

After applying the Fourier transform algorithm, the result of the gravitational potential maps is shown in Figure 7.2 for the same thickness and depths. Due to the higher resolution of the CIC and the Fourier algorithms, it is possible to see that the large structures are resolved better and the regions associated with larger voids are smoother and with values of Φ not so positive. Furthermore, the overdense regions are also well resolved, allowing us to know the more local and small gravitational potential that host particular overdense structures.

2.6.3 Time Derivative of Gravitational Potential

Applying again the Fourier transform algorithm in order to compute the time derivative of the gravitational potential in both regimes for the MDPL simulation gives the results shown in the following subsections.

2.6.3.1 Exact solution to $\dot{\Phi}$

In the right panel of Figure 7.3 we can see the corresponding maps of $\dot{\Phi}$ through the exact solution using the momentum field. As in the case of the simulation box of $400\ h^{-1}$Mpc (in subsection 2.3.3), these maps have a wider range of temperatures than the obtained through the linear approximation; this range is between $-4 \times 10^9 < \dot{\Phi} < 4 \times 10^9$ internal units. Despite those differences, we continue observing that the overdense regions of the maps in Figure 7.1 correspond to those regions of $\dot{\Phi}$ with the most positive values, while underdensities are associated with small positive or negative values of $\dot{\Phi}$. Furthermore, due to the higher resolution and the use of the exact solution it is possible to see how in those maps the larger underdense features present in the previous simulations are not present here because smaller structures are better resolved.

2.6.3.2 $\dot{\Phi}$ in Linear Regime

The maps obtained after applying the linear solution are shown in the left panel of Figure 7.3. Those maps show a very similar structure to the gravitational potential maps. As in the case of the exact solution, the larger underdense features present in the previous simulations are not present here, and the maps are smooth, mainly in regions associated with underdensities, while regions associated with overdensities are clearly resolved. Those regions with $\dot{\Phi} > 0$ in this linear regime coincide with the same regions in the exact regime, as explained above.

2.7 Summary of results

The results obtained in this chapter can be summarized in three items:

- **Effects of the Mass-assigment scheme (MAS) on the estimation of underlying fields:** As it was shown in subsection 2.3.4, the MAS has important effects in the estimation of the density contrast field. The TSC MAS gives a smoother field than the obtained through the CIC MAS, so the values from TSC are slightly smaller, i.e. $\delta_{CIC} > \delta_{TSC}$. In the case of $\dot{\Phi}(\mathbf{x})$ field, it looks that the estimations are more similar, i.e. $\dot{\Phi}_{CIC} \sim \dot{\Phi}_{TSC}$, but CIC has a slightly larger standard deviation and range of values. Then, the MAS has effects on the estimation of the underlying fields, showing expected behaviours with CIC given larger ranges of values than TSC, but the distributions are similar. A further analysis becomes necessary in order to quantify how the MAS affects the estimation of the temperature fluctuation due to the ISW effect. Such an analysis is shown in the next chapter.

- **Effects of the resolution on the estimation of underlying fields:** According to results from section 2.5, the resolution has no important effects on the estimation of the Φ and $\dot{\Phi}$ fields in larger scales. Although in the figures shown in section 2.5, the smallest resolution of 512^3 looks to show more features at the smallest scales but it is a because the color bar in the maps of Φ and $\dot{\Phi}$ fields is slightly wider for the highest resolution, but the general structures and the ranges of values are basically so similar that we can assure that the resolution has no considerable effects in the estimation of such fields. Furthermore, we will show in the next chapter that resolution will neither affect the estimation of the temperature field.

- **Effects of the regime of the solution (exact or lineal) on the estimation of $\dot{\Phi}(\mathbf{x})$:** In this case, considering the discussed results from subsection 2.3.3 for the simulation box of $400\ h^{-1}$Mpc and from subsection 2.6.3 for MDPL simulation we conclude that, as expected, the exact solution will offer a better estimation of the smallest of the structures. As discussed in those subsections, the influence of the velocity field in the evolution of the smaller structures is important and will represent an important contribution in the estimation of the $\dot{\Phi}(\mathbf{x})$ for the smaller and more local regions. On the other hand and also with and expected result, the linear approximation will show a very similar general behaviour at the largest scales if compared with the exact solution; but the information of the smallest scales will be suppresed and this field at such scales will be smoothed. We conclude that in the largest scales, the use of the linear approximation will give a very good estimated of the $\dot{\Phi}(\mathbf{x})$ field if compared with the exact solution, so the expected behaviour of the temperature field will be similar, i.e. that the linear approximation and the exact solution will give the same results in the largest scales, so for an estimation of the ISW effect, the use of the linear approximation will no lead to spurious signals or bad estimations. But it is important to take into account that if the idea is to know the behaviour of the fluctuations associated with smaller scales, the use of the exact solution becomes mandatory.

CHAPTER

3

Estimation of the Late ISW Effect in Cosmological Simulations

Once we know the $\dot{\Phi}$ field, either with the exact solution or in the linear regime, an interpolation of the values of $\dot{\Phi}(\mathbf{x})$ in the grid is performed. Once interpolated, these functions are integrated according to Equation 1.16. Although until now we have shown all maps as a projection along the z-axis, in this step we perform the integration along the three coordinate axes, as different lines-of-sight (LOS), in order to have enough variance in our samples. This step is performed for all the three cosmological simulations, with the aim to compare the large scales in all simulations and the ISW signal at each scale. Having different box sizes will allow us to study the influence of the cosmic variance in each ISW estimation. Furthermore, due to the different grid resolutions used, we can compare the effects of the grid in the ISW signal. For the largest boxes with higher resolutions a Rees-Sciama effect estimation could also be obtained.

After the integration along the 3 axes to obtain the ISW imprint, we divided the total temperature by the size of the box in each axis in order to obtain the temperature fluctuation per unit of length ($\Delta T/\Delta L$) in all the three simulations. This step was made for consistency in order to compare the ranges of $\Delta T/\Delta L$ and study the change of temperature along the whole trajectory of the photons. This temperature change should be of the same order of magnitude for the three simulations if it is indeed due to an actual physical effect, and not to numerical artifacts that affect the estimation of the ISW imprint. In this chapter, we show all the ISW maps we estimated from the previously computed $\dot{\Phi}$ field. The influence of the MAS and resolution effects on the ISW signal is discussed here alongside with the study on the distribution of values of the temperature fluctuation per unit of length.

3.1 ISW Effect from Simulation of $400\ h^{-1}$Mpc

3.1.1 ISW Effect from the Exact Solution

The ISW maps for the exact solution along the three axis of the box are shown in the left side panels of Figure 3.1. In the left-bottom panel of this figure, a cold region surrounded by hotter regions can be seen. This behaviour means that along the line-of-sight (the z-axis) there is a region dominated by voids in the density field, while around this zone, there is domain of overdense regions along the LOS. This feature may correspond to the large-mode that can not be resolved well enough in this small simulation box. Along the x and y axis one can also see some cold spots surrounded by hotter regions. It is possible to see how the cold spots have a slight larger contribution to the ISW imprint than the hotter spots in this simulation, but both hot and cold temperatures are in the same orders of magnitude. It is worth to notice the size of the spots we are obtained, which have diameters of the order of $100 - 150\ h^{-1}$Mpc; even some of them can reach $200\ h^{-1}$Mpc. This is an important fact because the larger sizes of the spots indicate us that we are observing large-scale fluctuations, which are associated with a ISW signal in this simulation.

The temperature ranges obtained in this regime due to the ISW effect are smaller than those reported in literature wich is a signal of $\Delta T = 10 - 20\,\mu$K in a ΛCDM cosmology [13]. Those smaller ranges are due to the small size of the box. We expect that for larger box sizes the ISW signal will be larger, as we will show above. The range of temperatures can be seen in Table 3.4, and can be compared with the ranges of the MultiDark simulations. This table also shows the change of temperature per unit of length $\Delta T/\Delta L$ for all the three simulations. The ranges of temperatures and the ranges of $\Delta T/\Delta L$ correspond to the overall maximum and minimum values obtained from the maps along the three axes. Taking the mean of ΔT for the three coordinates axes, it can be noticed that this mean value is around $1 \times 10^{-5}\ \mu$K even for both solution regimes. In the case of the mean $\Delta T/\Delta L$ for all the three axes, it is $1 \times 10^{-8}\ \mu$K h Mpc^{-1} for both solution regimes.

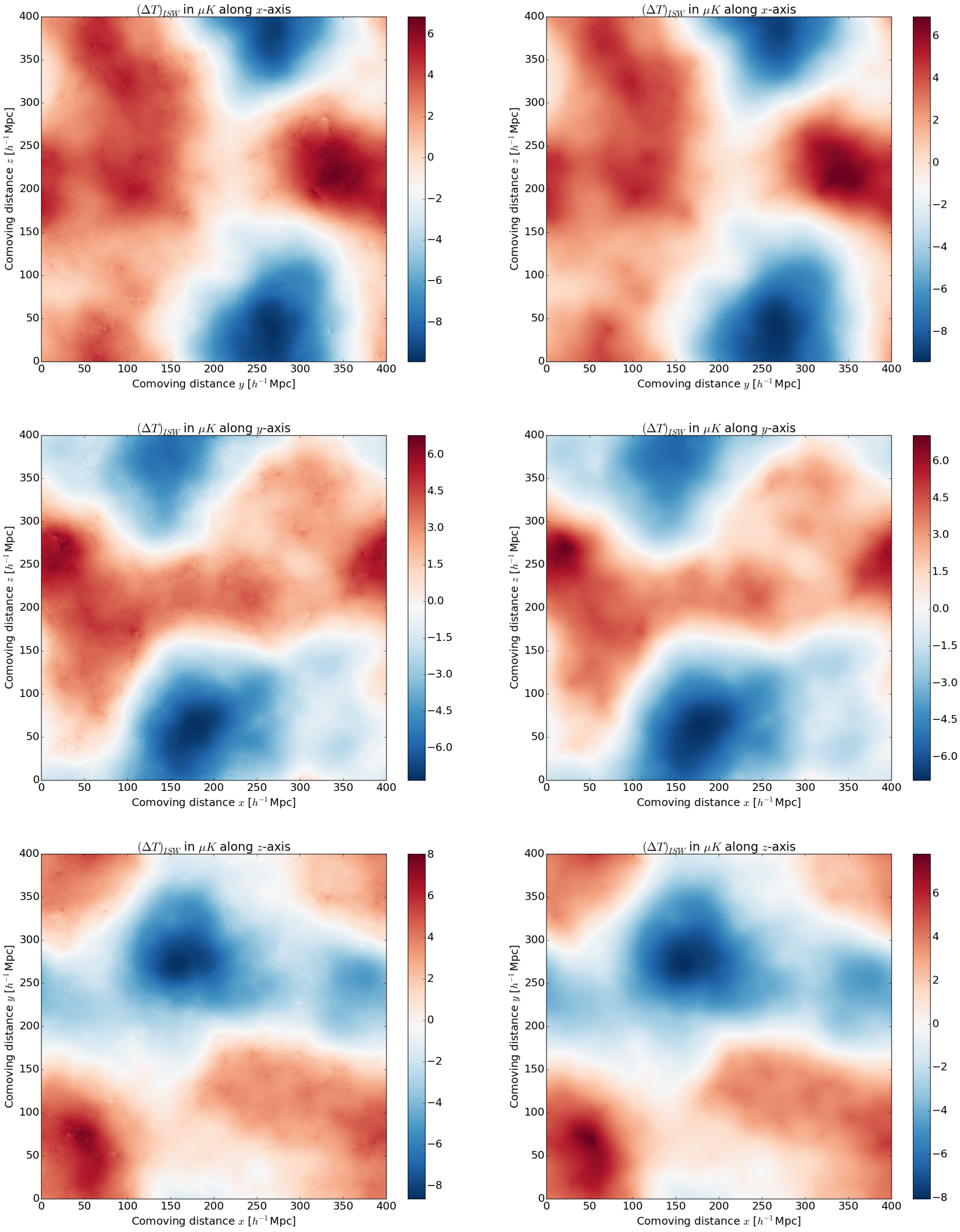

Figure 3.1: ISW maps obtained from the exact solution (left panels) and linear approximation (right panels) with the cosmological simulation data set from the box of $400\ h^{-1}$ Mpc. Upper panels correspond to the integration along the x-axis as LOS; middle panels to the integration along y-axis as LOS and bottom ones to the integration along z-axis as LOS.

3.1.2 ISW Effect in the Linear Regime

Following the same procedure described to obtain the ISW maps in the exact regime, we construct the ISW maps for the linear approximation in the three coordinates axes as different LOS. The corresponding maps are shown in the right panels of Figure 3.1.

In the linear approximation for $\dot{\Phi}$ it is possible to observe an analogue structure as the left panels shown in Figure 3.1 with the exact solution, but smoother. The details seen in the exact solution are due to the fact that in this regime the momentum field (or peculiar velocities) is used. As this field accounts for the movement of the structures at smaller scales, it may affect the growth of the structure itself; but in the linear approximation there is no use of the momentum field, so these small details disappear. The range of temperature fluctuations ΔT and the change of temperature per unit of length $\Delta T/\Delta L$ are shown in Table 3.4. Those temperature ranges are below the ones obtained using the exact solution, but the signal structure is very similar and the values do not differ too much with this exact solution. It can be noticed that although this simulation gives the smallest range of values for ΔT if compared with the values from the other simulations, the temperature per unit of length $\Delta T/\Delta L$ is in the same range and order of magnitude, so the change of temperature along the line of sight is consistent between all the simulations. As discussed before, the small size of the simulation affects the range of values for the total temperature fluctuation, ΔT, but not the temperature per unit of length. This result holds for both regimes, the exact solution and the linear approximation. Due to the resolution used, that allows to obtain for this simulation a cell size of 0.781 h^{-1}Mpc, the comparison with the other simulations is fair, so we are obtaining consistent results between slight different ΛCDM -CMB realizations for the expected behaviour of the ISW effect.

3.1.3 Effects of CIC and TSC Mass Assignment Schemes in temperature estimation

As in subsection 2.3.4 in the previous chapter, we study again the effects of the MASs in the estimation of the ISW temperature fluctuation looking for a possible spurious estimation in the ISW signal due to the precense of numerical artifacts from the MAS. In the following we will show a comparison between the temperature values obtained with a TSC MAS and those obtained through CIC. As pointed out before, this analysis between assigment schemes is done only for the 400 h^{-1}Mpc simulation box.

3.1.3.1 ΔT_{TSC} in the exact solution

As the temperature maps along each coordinate axis for the exact solution using a TSC MAS have the same temeprature range and structure, we do not show them here for brevity, but a further analysis was performed. Due to the similarity in temperatures and structure for both MAS, we conclude that although the assigment schemes produce different values of the $\dot{\Phi}(\mathbf{x})$ field, these fluctuations are compensated between them allowing to obtain the same temperatures. This fact is due to the integration performed, which makes a linear combination of the values of $\dot{\Phi}(\mathbf{x})$, allowing to compensate positive and negative contributions, so the temperature field will be the same.

The difference $\Delta T_{TSC} - \Delta T_{CIC}$ vs ΔT_{CIC} in the exact solution can be seen in Figure 3.2 at the left panels. This comparison shows that the difference $\Delta T_{TSC} - \Delta T_{CIC}$ is between 2 and 3 orders of magnitude smaller than the magnitude of values obtained with CIC. As we speak of ΔT in μK, those difference are in the order of 10^{-9}K or in the range of nano-Kelvin (nK), i.e. we can assure that $\Delta T_{TSC} \sim \Delta T_{CIC}$. Because both schemes give the same structure and the same temperature range, those differences may have no considerable effect in our estimation. So, in the estimation of the ISW effect, CIC or TSC may be used without expecting great differences, but in our work with data infered from observational surveys we will use only the TSC scheme, which is a better choice [18], [14].

A deeper comparison of the temperatures in both MAS is done when computing the corresponding histograms with their mean and standard deviation. For the exact solution, we can see those histograms at the left panel of Figure 3.3. In the legend it is shown the mean $\overline{\Delta T}$ and standard deviation σ, skewness b_1 and kurtosis g_2 for the estimated temperatures through each MAS. This information is also summarized in Table 3.1. Arguing to the CMB isotropy, which allows to assume that the behaviour of the distributions of temperature fluctuation along each coordinates axis must be similar, we study the projection only along the z-axis. We can see that the behaviour of the histograms is almost the same, maintaining the temperature ranges and basically the same statistical properties regardless of the MAS. These results support our statement concerning the fact that the MAS has no great effect in the ISW estimation, and no spurious signal on the ISW effect is observed due to the MAS.

The behaviour shown in those histograms allows us to conclude that the distribution of temperatures for the simulation box of $400\ h^{-1}$Mpc is not gaussian. The negative values for the skewness $-0.5 < b_1 < 0$ allows to conclude that this distribution is skewed to the negative values but not completely assymetrical and with a platykurtic, i.e. thinner tails, behaviour due to the negative excess of kurtosis, deviating from a gaussian distribution.

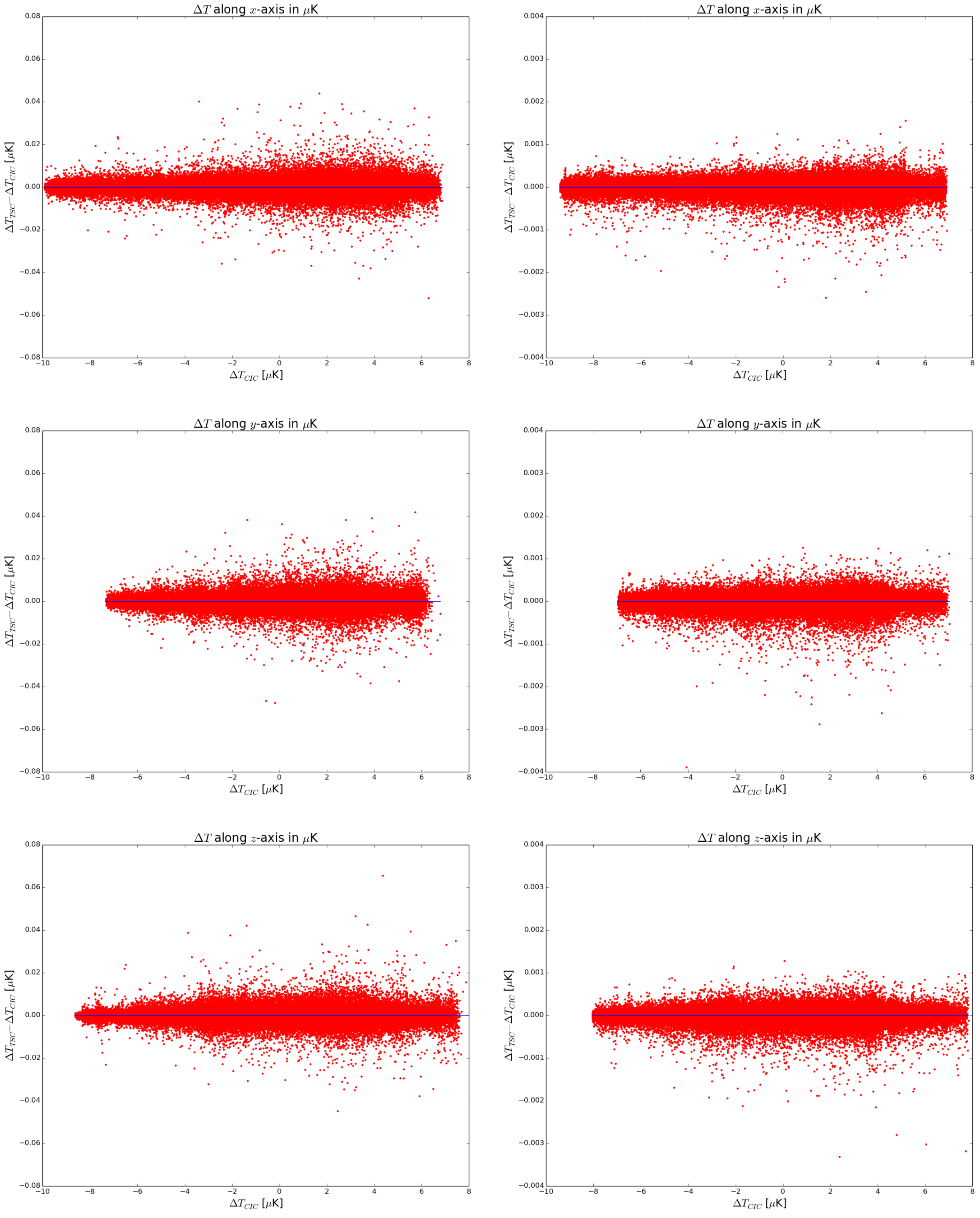

Figure 3.2: Difference $\Delta T_{TSC} - \Delta T_{CIC}$ vs ΔT_{CIC}. Left panels correspond to the estimation of temperatures with the exact solution, while right panels are those from the linear apprxomations. Upper panels are the temperature fluctuations integrated along x-axis, middle panels are those for y-axis and bottom one for z-axis. Blue lines represents a constant straigh line $y = 0$.

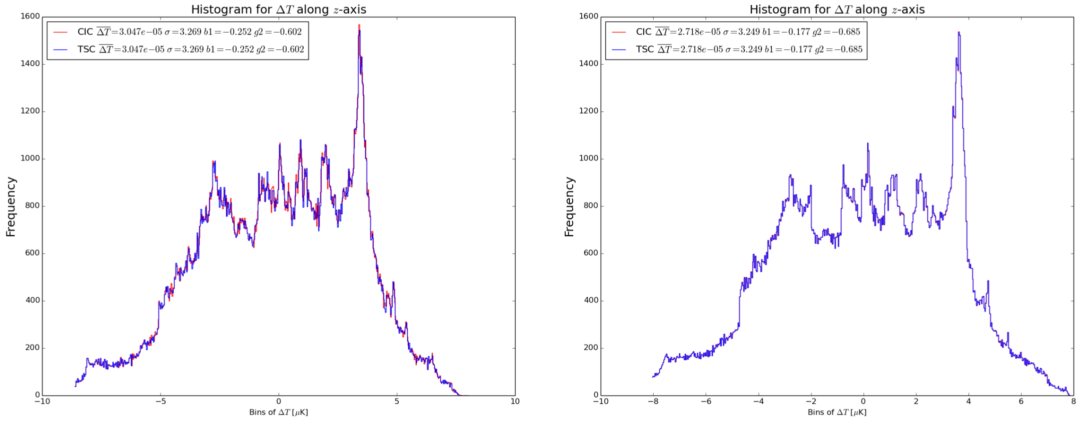

Figure 3.3: Histograms for the distribution of temperatures for both MAS. Left panel correspond to the temperature estimated through the exact solution, while right panel correspond to the linear approximation. Blue lines correspond to TSC MAS and red lines to CIC MAS. In both MAS the temperature distribution is basically the same.

Statistical property	ΔT_{Exact}	ΔT_{Linear}
$\overline{\Delta T}_{CIC}$ [μK]	3.047×10^{-5}	2.718×10^{-5}
σ_{CIC} [μK]	3.269	3.249
$b_{1,CIC}$	-0.252	-0.177
$g_{2,CIC}$	-0.602	-0.685
$\overline{\Delta T}_{TSC}$ [μK]	3.047×10^{-5}	2.718×10^{-5}
σ_{TSC} [μK]	3.269	3.249
$b_{1,TSC}$	-0.252	-0.177
$g_{2,TSC}$	-0.602	-0.685

Table 3.1: Table with the statistical properties of the distribution of temperatures for both MAS with the exact and linear solutions. It is very notable that both statistical quantities are basically the same no matter the MAS used. Differences between exact solution and linear approximation are more noticeable, but expected.

3.1.3.2 ΔT_{TSC} in the linear regime

For the linear regime and in the same way as for the exact solution, the temperature maps along each coordinate axis obtained through the TSC MAS have the same structure and temperature ranges than those obtained through a CIC MAS, so in the linear approximation we have the same conclusions than in the exact solution regime. For this reason, those maps are neither shown in this work.

The difference $\Delta T_{TSC} - \Delta T_{CIC}$ vs ΔT_{CIC} in this linear approximation is shown in the right panels of Figure 3.2. The difference $\Delta T_{TSC} - \Delta T_{CIC}$ is between 3 and 4 orders of magnitude below if compared with the values of ΔT_{CIC} in the linear approximation. This difference is then of the order of 0.1nK, one order of magnitude below the results from the exact solution, so for the linear regime we have that the statement of $\Delta T_{TSC} \sim \Delta T_{CIC}$ is even stronger than for the exact solution. As in this linear regime this difference is even smaller, again, the choice of the MAS has no considerable effect in our estimation of temperatures.

The histogram for the distribution of the temperatures in the linear regime is shown in the right panel of Figure 3.3, and the information about statistical properties is also summarized in Table 3.1. In the same way as for the exact solution, the distribution of temperatures is basically the same no matter the MAS used and the means and standard deviations show no difference. This fact allows us to maintain our conclusion that either CIC or TSC may be used to estimate the ISW effect withouth notable differences. Furthermore, it can also be noticed that the mean in the linear approximation is just slightly smaller than the mean in the exact solution, and the standard deviation of both regimes have a very similar value.

3.2 ISW Effect from MDR1 Simulation

3.2.1 ISW Effect in the Linear Regime

Once we know the values of $\dot{\Phi}$ for the linear regime, we proceed to perform the interpolation and integration of values along three LOS, in the same way as we did with the simulation box of $400\,h^{-1}$Mpc. This allows to obtain the maps shown in Figure 3.4 at the left panels for the resolution of 512^3 cells.

The feature that stands out in those maps is the cold spot observed in the map along the z-axis. This spot has very low temperature compared with the spots in the other maps and may be due to another large-mode that can not be resolved completely due to the resolution of CIC MAS. As mentioned for the maps of the previous simulation, we can infer that behind this cold spot there is a major contribution to the temperature fluctuation due to underdensities. Despite of this feature, we can notice that our ΛCDM theoretical estimation of the ISW agrees even more (compared with the previous simulation box) with the proposed expectation from [13], i.e. expected temperature ranges due to ISW of the order of $\sim 10-20\ \mu$K in a ΛCDM universe, but in our case with a slight wider range.

As aforementioned, the comparison of the temperature ranges and the ranges of $\Delta T/\Delta L$ are shown in Table 3.4. Comparing the mean ΔT and $\Delta T/\Delta L$ from this simulation with the values from the simulation box of $400\ h^{-1}$Mpc, it can be noticed that the order of magnitudes are the same, altough for MDR1 it tends more to positive values.

3.2.2 Effects of the Resolution for MDR1 Simulation in the Linear Regime

Using the results obtained with the MDR1 simulation with the higher resolution of 1024 cells per axis, we obtain the following ISW maps, after integrating along all the LOS, as shown in the right panels of Figure 3.4.

From those maps, and as mentioned in subsection 2.5.2, we can see that there is no change in the general structure of the pattern generated by the ISW effect due to the structures in the MDR1 simulation. Furthermore, the ranges of temperatures remain the same as in the lower resolution case. From those maps, we can state that for the linear approximation, there is no change in the estimation of the ISW effect if we analyze the simulation through a grid of 512^3 or 1024^3 cells. In general, we can say that resolution has no effect our estimation. To prove this statement, we compare the temperature distributions for both resolutions. The corresponding normalized histograms can be seen in Figure 3.5

with their statistical properties, which are summarized in Table 3.2. Comparing the statistical properties of both distributions, we can notice that the differences are so small, even although the mean for the resolution of 1024 is one order of magnitude below the resolution of 512, we can ensure that both resolutions share the same distribution. These results support our conclusion that resolution does not have a considerable effect in our ISW estimation for the linear approximation.

Besides, the values of skewness and kurtosis for the distribution of temperatures for MDR1 also shows that the distribution is not gaussian; even we can see a more skewed distribution to negative values than for the previous simulation.

Statistical property	MDR1$\times$512	MDR1$\times$1024
$\overline{\Delta T}$ [μK]	2.255×10^{-5}	5.295×10^{-6}
σ [μK]	12.299	12.298
b_1	-0.653	-0.652
g_2	-0.077	-0.077

Table 3.2: Table with the statistical properties of the distribution of temperatures for MDR1 simulation. It can be noticed that the statistical properties differ so slight between both resolutions that we may assert that resolution has no considerable effect in the ISW estimation.

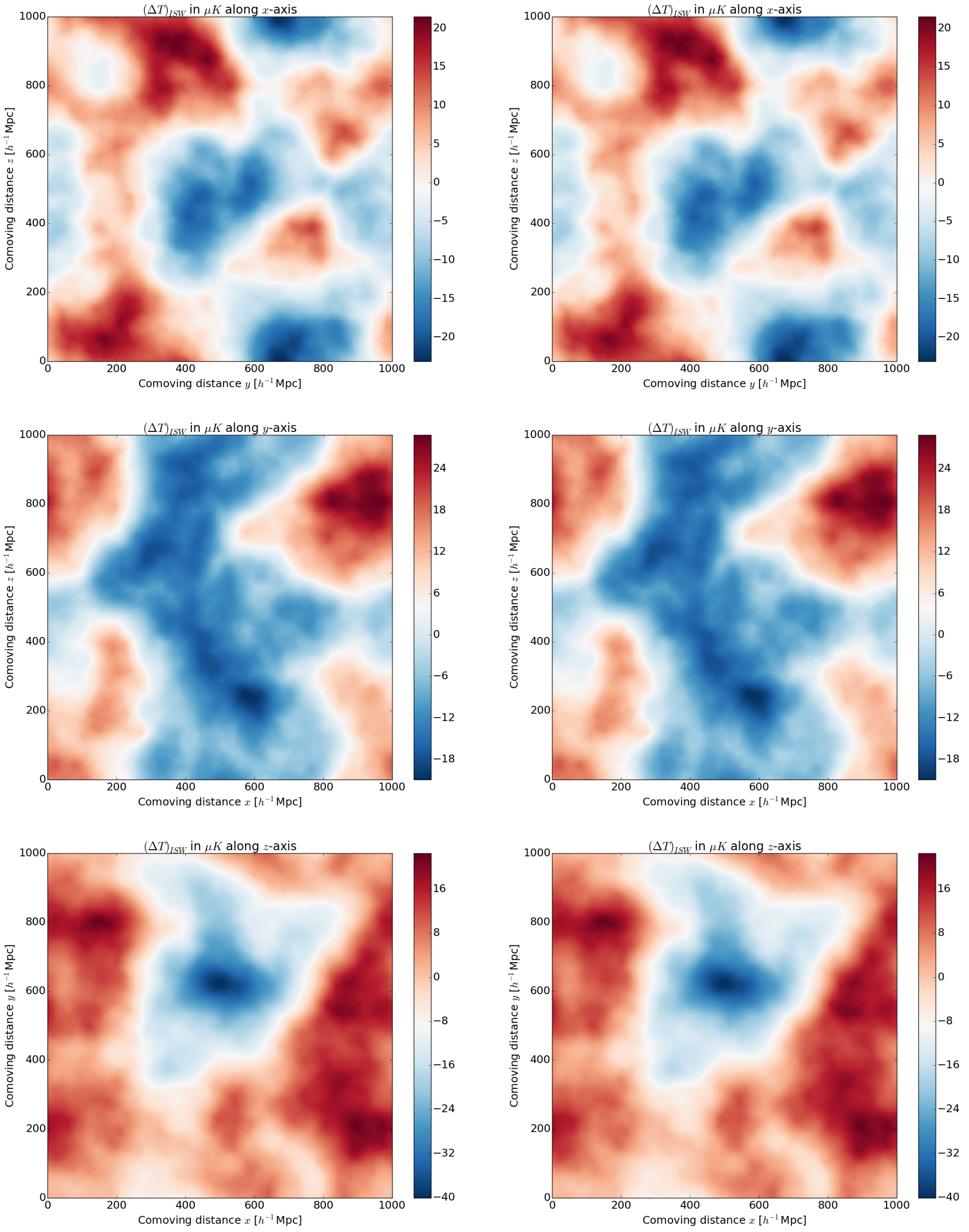

Figure 3.4: ISW effect map for *Multidark 1* simulation in the linear approximation. Left panels correspond to the lowest resolution of 512^3 cells, while right panels to the highest resolution of 1024^3 cells. Upper panels corresponds to the integration along the x-axis as LOS; middle panels to the integration along y-axis as LOS and bottom to the integration along z-axis as LOS. It can be noticed that regardless the resolution, the structure and temperature ranges remains the same.

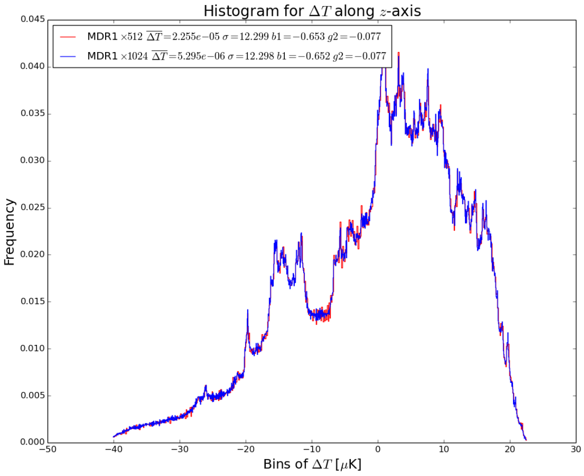

Figure 3.5: Histograms with the distribution of temperatures in the MDR1 simulation. Blue line correspond to the highest resolution of 1024 cells per axis; red line to 512 cells per axis. The blue line presents a larger amplitude, which is given by the fact that for this high resolution there is a larger ammount of points than the low resolution, but the statistical properties ensure that both distributions are the same. An appropiate normalization is performed to compare both histograms.

3.3 ISW Effect from MDPL Simulation

3.3.1 ISW Effect in the Exact Regime

Using the exact solution for $\dot{\Phi}$ in the MDPL simulation, we obtain the ISW effect maps shown in the left panels of Figure 3.6 along the three lines-of-sight from top to bottom. In this case, due to the higher resolution of the CIC and Fourier algorithms, the cold and hot spots are resolved better and the small-scale structures due to the momentum field can be seen in great detail, as in the case of the simulation box of $400\ h^{-1}$Mpc. This small scales give an insight of how the Rees-Sciama amplitude must be.

In Figure 3.7 it is possible to observe the histogram with the temperature distribution for the exact solution in red. Again, the range of temperatures for our theoretical estimation in a ΛCDM universe agrees with the expectation proposed in [13]. Contrary to the results found with the previous simulations, this distribution has a positive skewness, indicating an assymetry towards positive values, but it continues to be a platykurtic distribution. So again, the temperatures distribution differs from a gaussian distribution. The statistical properties are summarized in Table 3.3. We can notice that in this simulation, with a slight different value of Ω_Λ and a large resolution of 1024^3 the distribution looks different from the temperature distributions obtained for MDR1 and for the $400\ h^{-1}$Mpc box, being skewd toward hotter temperatures. Even, comparing the exact solution and the linear approximation temperature distributions, there are more noticeable differences but those may be due to the approach used; in spite of those differences, both distributions look similar, with means near $0\ \mu$K and with the same range of temperatures This supports again the fact that for larger scales, the linear approximation and exact solution give almost the same results. From those results, we can also conclude that, as the Rees-Sciama effect needs more resolution at the smallest scales and the use of the exact solution, this could have changes in the temperature distributions.

Statistical property	MDPL-Exact	MDPL-Linear
$\overline{\Delta T}$ [μK]	-2.897×10^{-5}	-6.570×10^{-5}
σ [μK]	8.107	8.096
b_1	-0.168	-0.179
g_2	-0.458	-0.457

Table 3.3: Table with the statistical properties of the distribution of temperatures for MDPL simulation. It can be noticed that the statistical properties differ so slight between both solution regimes.

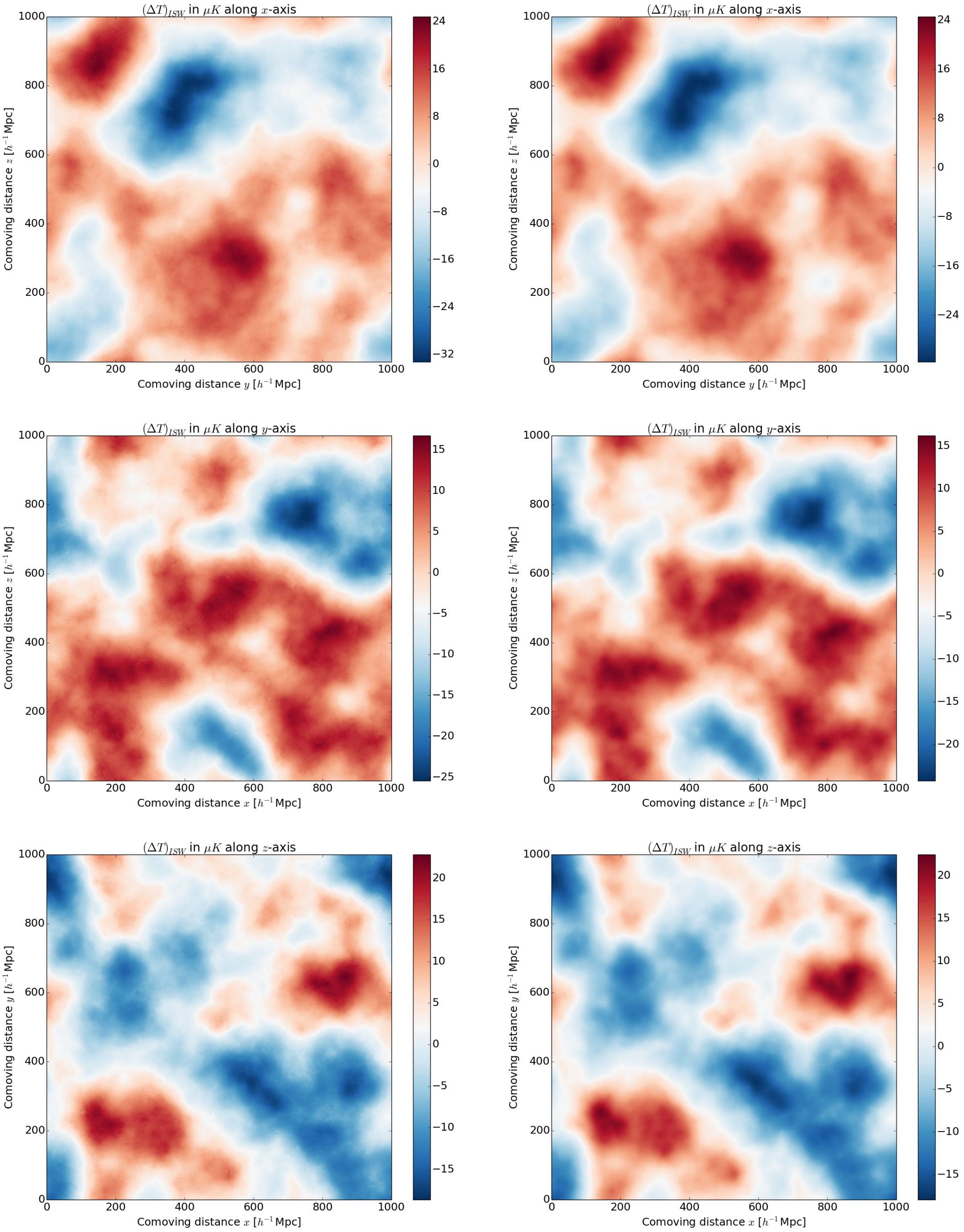

Figure 3.6: ISW maps obtained of MDPL simulation. Left panels correspond to the temperature fluctuation estimated through the exact solution, while right panels correspond to the linear approximation. Upper panels correspond to the integration along the x-axis as LOS; middle ones along y-axis as LOS and bottom ones along z-axis as LOS. As expected, the exact solution allows to resolve better the smallest of the scales, while the linear regime gives a good approximation to the general structure of the larger scales, while smoothing the smaller ones.

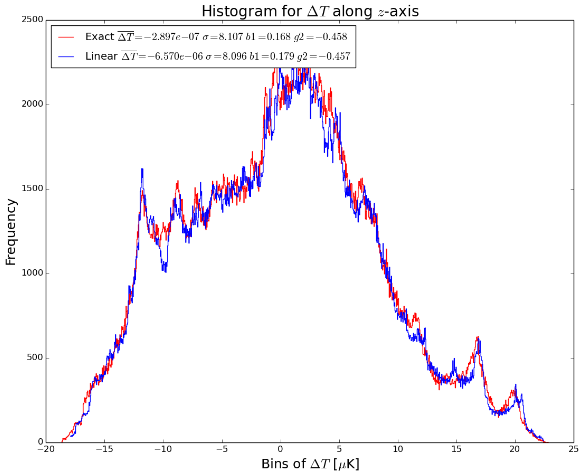

Figure 3.7: Histograms with the temperature distributions for MDPL simulation. Red line shows the distribution for the exact solution, while blue line for the linear approximation. Statistical properties and the behaviour of the distributions are very similar with only slight fluctuations, as expected due to the nature of each regime.

3.3.2 ISW Effect in the Linear Regime

Right panels of Figure 3.6 show the ISW maps along the different LOS for the MDPL simulation in the linear regime approximation for $\dot{\Phi}$. As seen in the previous simulations, the linear approximation gives a slight narrower range of temperatures than the exact solution, and shows an smoother structure due to the lack of knowledge about the momentum or velocity field, that acts at small scales. The ranges of temperatures and the range of values for $\Delta T/\Delta L$ for both regimes are shown alongside the ranges for the other simulations in Table 3.4.

For both ISW maps obtained from MDPL simulation we can see that the temperature ranges are in agreement with the the expected values from [13], and although some above the range of temperatures of MDR1, they are consistent and allow us to obtan an imprint on the temperature profile due to the presence of structures as a theoretical expectation in ΛCDM universes. Comparing the values of the mean ΔT and $\Delta T/\Delta L$ in Table 3.4 for both solution regimes we see that they are very similar in order of magnitude. If compared with the same mean values for MDR1 or the small simulation box of 400 h^{-1}Mpc, it can be noticed that for MDPL the mean values are nearer zero than for the other two simulations. Taking into account that MDR1 and the box of 400 h^{-1}Mpc are a ΛCDM - WMAP cosmology while MDPL has a ΛCDM - Planck cosmology, it can be noticed that the value of Ω_Λ could introduce slight changes, but the orders of magnitude in which such changes are introduced are so small that we may considere that in principle, there is no higher dependence on the cosmological constant density parameter.

Simulation	MDPL ($\Omega_{\Lambda,0} = 0.6922885$)	MDR1 ($\Omega_{\Lambda,0} = 0.73$)	400 h^{-1}Mpc ($\Omega_{\Lambda,0} = 0.742$)
ΔT_{Exact} [μK]	(∼-32.0, ∼24.0)	No Data	(∼-9.0, ∼8.0)
$\overline{\Delta T}_{\text{Exact}}$ [μK]	-5.97792×10^{-7}	No Data	-1.73864×10^{-5}
ΔT_{Linear} [μK]	(∼-30.0, ∼24.0)	(-40.0, ∼27.0)	(∼-9.0, ∼7.0)
$\overline{\Delta T}_{\text{Linear}}$ [μK]	2.48579×10^{-7}	1.30466×10^{-5}	-1.80528×10^{-5}
$(\Delta T/\Delta L)_{\text{Exact}}$ [μK hMpc^{-1}]	(∼-0.032, ∼0.024)	No Data	(∼-0.022, ∼0.02)
$\overline{(\Delta T/\Delta L)}_{\text{Exact}}$ [μK hMpc^{-1}]	-1.49448×10^{-9}	No Data	-4.34661×10^{-8}
$(\Delta T/\Delta L)_{\text{Linear}}$ [μK hMpc^{-1}]	(∼-0.03, ∼0.024)	(-0.04, ∼0.027)	(-0.022, 0.017)
$\overline{(\Delta T/\Delta L)}_{\text{Linear}}$ [μK hMpc^{-1}]	6.21449×10^{-10}	3.26165×10^{-8}	-4.51321×10^{-8}

Table 3.4: Ranges of temperature fluctuation ΔT in both regimes and ranges of change of temperature per length of unit $\Delta T/\Delta L$ also in both regimes. Those ranges are shown for the three simulations and are obtained as the overall maximum and minimum values of the ranges per axis. We show the value of Ω_Λ for each simulation in order to see how the density parameter of Dark Energy may affect the temperature range values; according to the mean value of ΔT and $\Delta T/\Delta L$ there is no high dependence on this parameter. In the case of MDR1 simulation, only the linear approximation values are known, and as in the two resolutions used the range of temperatures is the same, it is not necessary to show the results for both of them. It should be noticed that for the higher resolution of 1024 the cell size is 0.976 h^{-1}Mpc and for the resolution of 512 the cell size is 0.781 h^{-1}Mpc; as our resolutions allow us to resolve until scales of around ~ 1 h^{-1}Mpc, we have fair comparisons of the temperature fluctuations in all cases.

3.4 Temperature fluctuation along the LOS

Finally, for cosmological simulations we computed the temperature fluctuation along the LOS $\mathrm{d}T/\mathrm{d}r$, in the same way as Figure 2 of [6]. For this, we implemented different analysis for the MDR1 and MDPL simulations. For the MDR1 simulation we did a resolution analysis and for both, MDR1 and MDPL we performed a brief statistical analysis, as explained in subsection 3.4.2. This brief statistical analysis will help us to characterize the distribution of values for $\mathrm{d}T/\mathrm{d}r$.

In order to compute $\mathrm{d}T/\mathrm{d}r$ we take the values of $\dot{\Phi}$ in the simulation box, then we numerically integrate Equation 1.16 from back to front in each of the cells along the chosen LOS-axis. Along this LOS-axis, we began to integrate from the inner border of the last cell as the lower integration limit, with position $r_{in} = (\text{Box Size} - \text{Cell Size})h^{-1}$Mpc until the outer border of the cell with position $r_{out} =$ Box Size h^{-1}Mpc. After that, we divided by the step length and obtain the temperature fluctuation per unit length in one cell. Then, we performed the same procedure but varying the lower integration limit by the size of a cell until it reach $r_{in} = 0\ h^{-1}$Mpc while the upper limit remains the same, i.e. $r_{out} =$ Box Size h^{-1}Mpc. This was made for each pixel on the grid in the plane $z = 0\ h^{-1}$Mpc.

3.4.1 Resolution analysis for MDR1 simulation

In the first analysis we obtain the temperature fluctuation along the LOS $\mathrm{d}T/\mathrm{d}r$ along each of the three coordinate axes for the two resolutions, 512^3 and 1024^3 cells. Then we compare $\mathrm{d}T/\mathrm{d}r$ for both resolutions. As an example, we took an integration along the z-axis as LOS. A row-major ordering of the cells (for a detailed explanation of the indeces, see [35]) will give indeces in 3 dimensions to each cell in this block of as follows:

$$m = k + N_g(j + N_g\, i), \tag{3.1}$$

where N_g is the number of cells per axis and (i, j, k) are indeces corresponding to the position of the cell in (x, y, z) respectively and take values $i, j, k = 0, \cdots, N_g - 1$. If we take $i = j = 0$ and let k to vary we obtain the indeces of the block of cells along the z-axis as LOS that may have a projection over the cell with $m = 0$ in the xy plane. It is also possible to see that the cell $m = 0$ in the grid of $N_g = 512$ should correspond to the mean contribution of the blocks of cells that have a projection in the cells $m = 0,\ N_g - 1,\ N_g^2 - 1, N_g^2 - 1 + (N_g - 1)$ in the xy plane for $N_g = 1024$ grid.

Then, we compare the block of cells along the z-axis as LOS that has projection (in xy plane) in $m = 0$ for $N_g = 512$ with the four block of cells that has projection (in

xy plane) in the indeces $m = 0,\ N_g - 1,\ N_g^2 - 1, N_g^2 - 1 + (N_g - 1)$ for $N_g = 1024$. Finally, those comparisons must present the same behaviour because as the four cells in the $N_g = 1024$ grid are contained inside the big cell $m = 0$ for $N_g = 512$, so this big cell is an average of the behaviour of the 4 cells of $N_g = 1024$. This is true whatever the choosen coordinate axis as LOS. This can be seen in Figure 3.8 for some cells with $\mathrm{d}T/\mathrm{d}r$ taken along the x-axis, in Figure 3.9 for the y-axis as LOS and in Figure 3.10 for the z-axis as LOS.

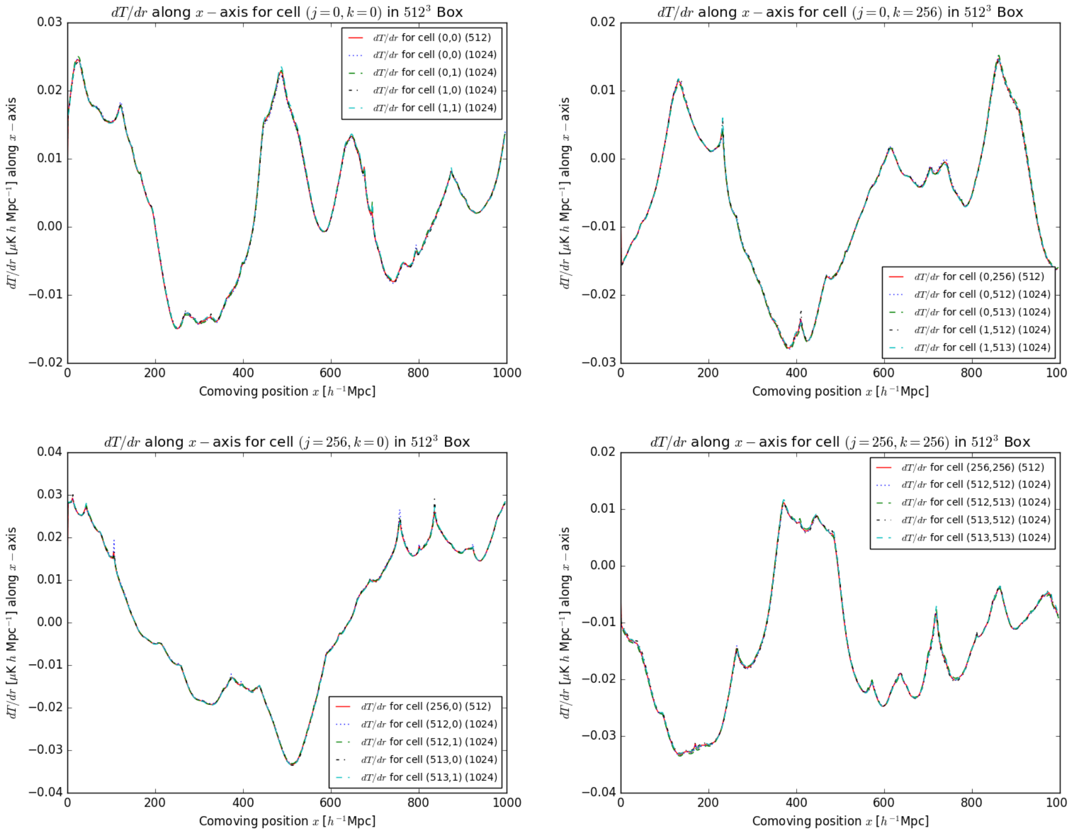

Figure 3.8: Comparison of the temperature fluctuation per unit of length $\mathrm{d}T/\mathrm{d}r$ for the two resolutions used in the MDR1 simulation (512^3 and 1024^3 cells). The integration was performed along the x-axis as LOS and then, the projection will be in the yz plane, that has index $i = 0$. In the upper-left panel we can see the $\mathrm{d}T/\mathrm{d}r$ for the block of cells that will be projected in the cell with $(j = 0, k = 0)$ if we see a map in the yz plane for $N_g = 512$ (the index i is 0 due to this projection). Then, the cell of the projection, according to Equation 3.1 will be $m = 0$ for $N_g = 512$. In the grid with $N_g = 1024$, the block of four cells that are inside the same block of $N_g = 512$ correspond to indeces $(j = 0, k = 0)$, $(0, 1)$, $(1, 0)$, $(1, 1)$. The other three panels have an analogous explanation.

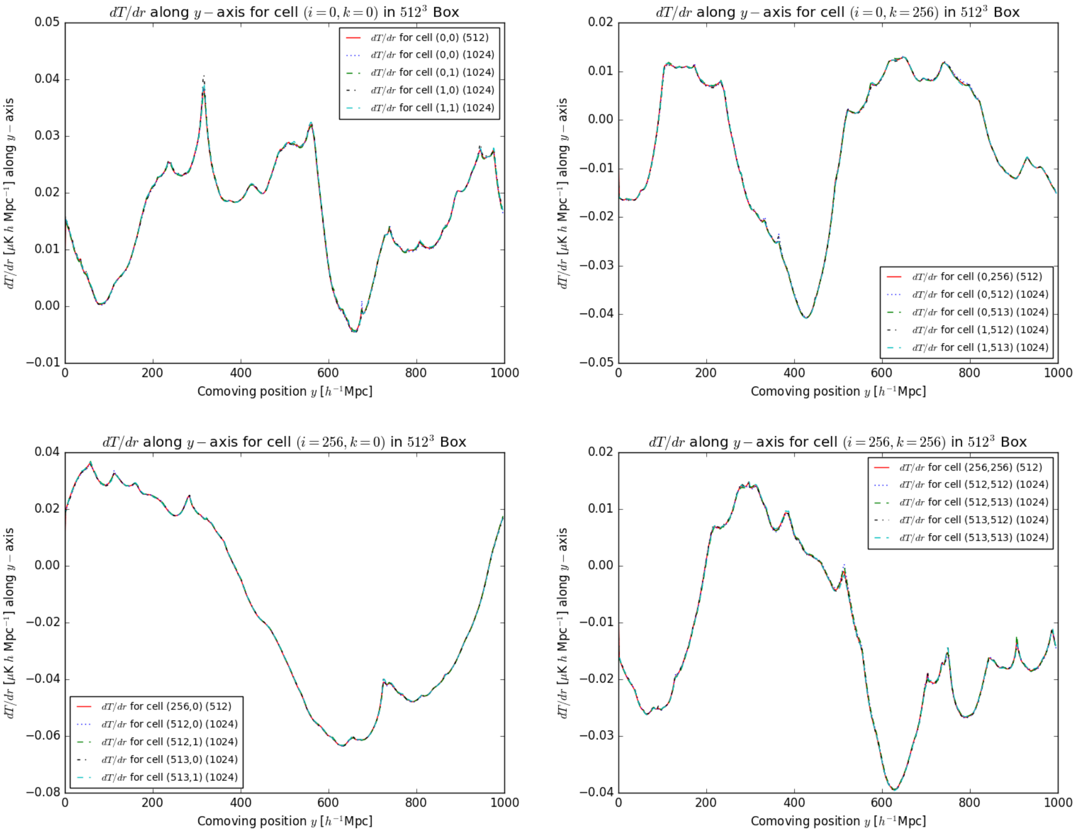

Figure 3.9: Comparison of the temperature fluctuation per unit of length $\mathrm{d}T/\mathrm{d}r$ for the two resolutions used in the MDR1 simulation (512^3 and 1024^3 cells). The integration was performed along the y-axis as LOS and then, the projection will be in the xz plane, that has index $j = 0$. In the upper-left panel we can see the $\mathrm{d}T/\mathrm{d}r$ for the block of cells that will be projected in the cell with $(i = 0, k = 0)$ if we see a map in the xz plane for $N_g = 512$ (the index j is 0 due to this projection). Then, the cell of the projection, according to Equation 3.1 will be $m = 0$ for $N_g = 512$. In the grid with $N_g = 1024$, the block of four cells that are inside the same block of $N_g = 512$ correspond to indeces $(i = 0, k = 0)$, $(0, 1)$, $(1, 0)$, $(1, 1)$. The other three panels have an analogous explanation.

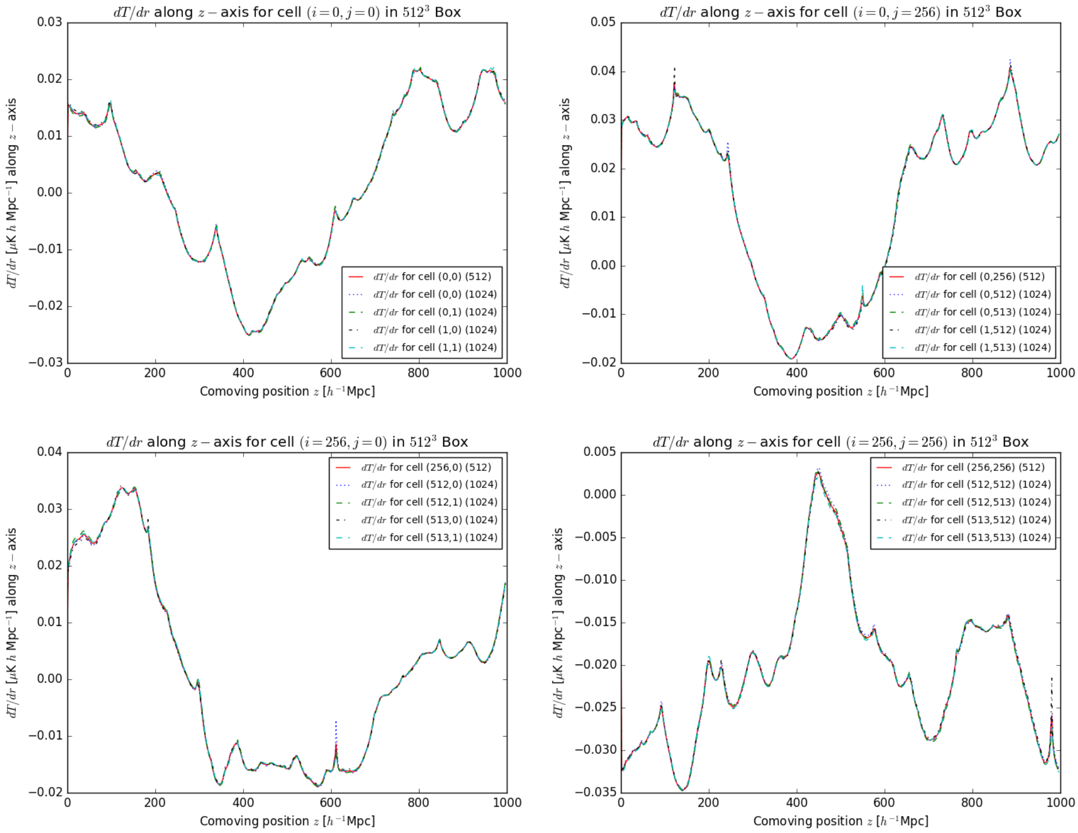

Figure 3.10: Comparison of the temperature fluctuation per unit of length $\mathrm{d}T/\mathrm{d}r$ for the two resolutions used in the MDR1 simulation (512^3 and 1024^3 cells). The integration was performed along the z-axis as LOS and then, the projection will be in the xy plane, that has index $k = 0$. In the upper-left panel we can see the $\mathrm{d}T/\mathrm{d}r$ for the block of cells that will be projected in the cell with $(i = 0, j = 0)$ if we see a map in the xy plane for $N_g = 512$ (the index k is 0 due to this projection). Then, the cell of the projection, according to Equation 3.1 will be $m = 0$ for $N_g = 512$. In the grid with $N_g = 1024$, the block of four cells that are inside the same block of $N_g = 512$ correspond to indeces $(i = 0, j = 0)$, $(0, 1)$, $(1, 0)$, $(1, 1)$. The other three panels have an analogous explanation.

From these figures it is possible to see that the resolution has no effect in the estimation of $\mathrm{d}T/\mathrm{d}r$ and indeed the result obtained with the resolution of 512^3 cells looks like the average behaviour of the 4 corresponding values obtained with the highest resolution of 1024^3 cells. Furthermore, we can see that the ranges of values that $\mathrm{d}T/\mathrm{d}r$ takes are in good agreement with those shown in Figure 2 of [6] in the spatial range of $0 - 1000\, h^{-1}$Mpc. The fact that the quantity $\mathrm{d}T/\mathrm{d}r$ is not affected by resolution is in agreement with our previous analysis of the distribution of temperatures for MDR1 in subsection 3.2.2 where we see that both resolutions share the same temperature distribution with very similar statistical properties and the same range of temperatures.

3.4.2 Mean $\mathrm{d}T/\mathrm{d}r$ for MDR1 and MDPL simulations

After performing the resolution test, we obtained the mean $\mathrm{d}T/\mathrm{d}r$ along each LOS. For this step, what we do can be seen again with an example: after knowing the complete data of $\mathrm{d}T/\mathrm{d}r$ for a certain LOS, as the z-axis, we know that the projection of the temperature must be seen in the xy-plane. Then for each position z (we can access to it through the indeces), we averaged the values of $\mathrm{d}T/\mathrm{d}r$ for the corresponding xy-plane. Then, we move to the next position in z, and continue averaging in the $\mathrm{d}T/\mathrm{d}r$ for the corresponding xy-plane, and so on. This allow us to obtain an average profile of $\mathrm{d}T/\mathrm{d}r$ for a certain LOS with the corresponding variance. This was performed for all the 3 coordinate axis for the MDPL simulation and the MDR1 simulation (with the two resolutions). As we saw in subsection 3.4.1, the resolution has no considerable effect on the estimation of $\mathrm{d}T/\mathrm{d}r$ so we will show only the results obtained for the highest resolution grid.

The mean $\mathrm{d}T/\mathrm{d}r$ for MDR1 simulation with 1024^3 cells is shown in Figure 3.11 as a red line with a red-shadowed region as the variance. Remember that for MDR1 the integrand of Equation 1.16 was obtained through the linear approximation given by Equation 2.31. It can be seen that the average behaviour of the temperature fluctuation per unit of length is near to zero, with a mean standard deviation of the order of ~ 0.0169 μK h Mpc^{-1} for the x-axis as LOS, ~ 0.0181 μK h Mpc^{-1} for the y-axis and ~ 0.0186 μK h Mpc^{-1} z-axis as LOS.

For MDPL simulation, the values of $\mathrm{d}T/\mathrm{d}r$ were computed in both regimes, the exact solution (Equation 2.30) and the linear solution (Equation 2.31). For the exact solution, the profile can be seen as the blue line in Figure 3.11 with the blue-shadowed region as the variance. Again, we can see a mean behaviour near zero for all the three LOS, with a mean standard deviation of ~ 0.0181 μK h Mpc^{-1} for the x and y-axes as LOS, and ~ 0.0172 μK h Mpc^{-1} for the z-axis. For the linear approximation shown as the yellow line in the same figure, the behaviour is almost the same as obtained in the exact regime,

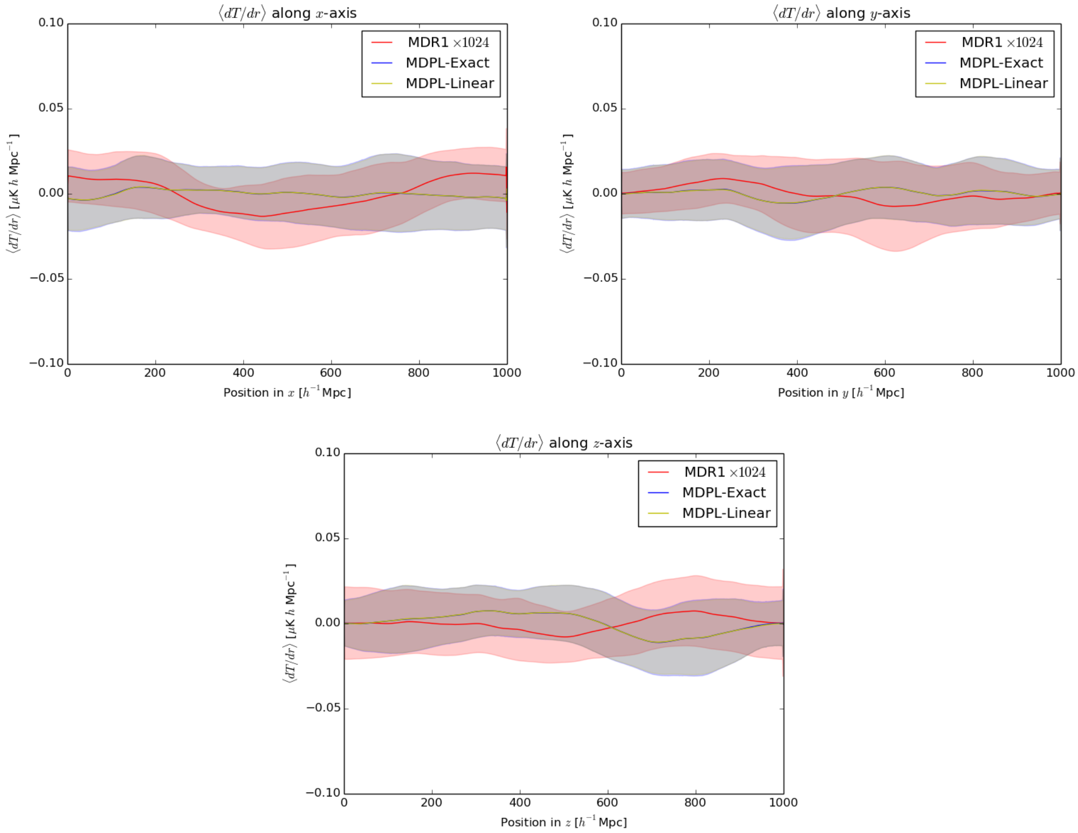

Figure 3.11: Average $\mathrm{d}T/\mathrm{d}r$ for all the LOS in the MDR1 simulation with a resolution of 1024^3 cells and MDPL simulation. The red line represents the mean value that $\mathrm{d}T/\mathrm{d}r$ takes for the MDR1 simulation while the red-shadow region shows the variance of this distribution. In this case, the values of $\mathrm{d}T/\mathrm{d}r$ were computed in the linear aproximation (Equation 2.31). For MDPL, the exact solution is shown as the blue line and the blue-shadowed region, while the linear approximation is the yellow line with a yellow-shadowed region. The overlapping for both regimes in MDPL is almost complety, but the variance of the linear approximation (yellow) is slightly below the variance for the exact solution.

but the mean standard deviations are some below: ~ 0.0178 μK h Mpc^{-1} for the x and y-axes and ~ 0.0169 μK h Mpc^{-1} for the z-axis as LOS. It can be noticed that the variances for the linear approximation are almost the same as for the exact solution, so a complete overlapping of both variance regions is appreciated, making the yellow-shadowed region of the linear approximation to lay just above the blue region.

The general behaviour of these plots shows that the temperature fluctuations along each axis are very near to zero, so the structures along the path of the photons perturb slightly the photons energy (or temperature), making such kind of contributions to the ISW effect very small. The fact that those contributions have means very near to zero is in agreement with the estimated means of the complete temperature fluctuation shown in the temperature distributions (remember Figure 3.5 for MDR1 and Figure 3.7 for MDPL). In addition, we can see that the linear approximation contributes almost in the same order of magnitude than the exact solution, so this linear growth of structures may be considered the main responsible for an ISW signal which is an expected result due to the large-scale nature of this phenomenon. Then, the exact solution will contribute mainly at the smallest scales, allowing to obtain a Rees-Sciama signal, but giving fewer information to the ISW signal amplitude.

The plots presentend in this section will help us as a comparison with the ISW effect computed for the observational data. When the ISW signal will be computed and, furthermore, the $\mathrm{d}T/\mathrm{d}r$ for the observational data, we may compare if the mean of those fluctuations are larger (in absolute value) than the obtained in this section or if the fluctuation is too small that is inside the variance of the $\mathrm{d}T/\mathrm{d}r$ for the data of the simulations.

3.4.3 Skewness and kurtosis of $\mathrm{d}T/\mathrm{d}r$ for MDR1 and MDPL simulations

Additional to the mean temperature fluctuation per unit of length $\mathrm{d}T/\mathrm{d}r$ and its corresponding variance shown in subsection 3.4.2, we computed for each plane higher statistical moments such as the skewness (b_1) and the kurtosis (g_2) to have some insight in the distribution of $\mathrm{d}T/\mathrm{d}r$ in each plane for all the LOS used.

3.4.3.1 Skewness and kurtosis for MDR1 simulation

As the MDR1 simulation was analized with the linear approximation (Equation 2.31), so we would expect that the behaviour of each distribution of $\mathrm{d}T/\mathrm{d}r$ is near gaussian. In Figure 3.12 we show the skewness for each LOS in the MDR1 simulation with 1024 cells per axis; there can be seen the fluctuation of the skewness for each plane near to zero. The peaks in this figure tell us that in the plane at those depths (in the corresponding LOS) we can find that the distribution of $\mathrm{d}T/\mathrm{d}r$ has a larger tail through positive values, while the valleys in the figure will indicate that a certain plane will have a distribution with a larger tail for the negative values. In general, it can be seen that for the three LOS, almost all the values of the skewness are concentrated in the range $-0.5 < b_1 < 0.5$ so the distribution of $\mathrm{d}T/\mathrm{d}r$ values are nearly symmetric, with only few regions with $0.5 < |b_1| < 1.0$ indicating a moderately skewed distribution for those planes.

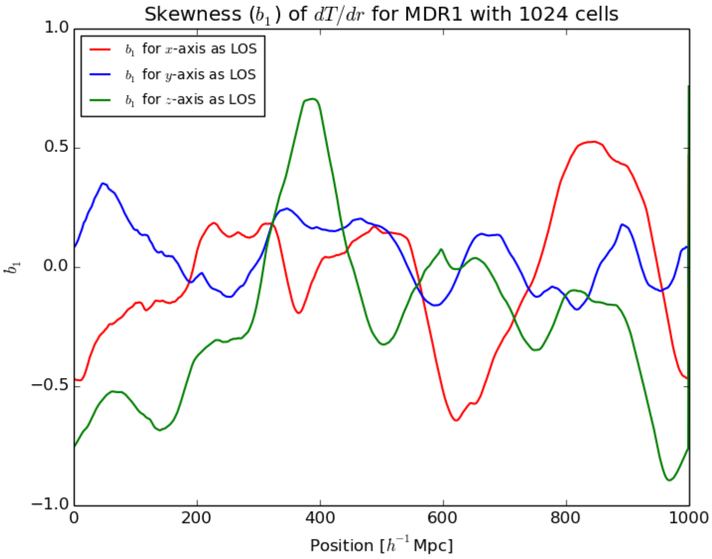

Figure 3.12: Skewness of the distribution of $\mathrm{d}T/\mathrm{d}r$ for each plane along the three different LOS used. This was obtained for the MDR1 simulation with 1024 cells per axis in the linear approximation. It can be seen a fluctuation of the skewness around 0, which is the expected value for a gaussian distribution.

We used GSL to compute the statistical moments of those distributions, so the kurtosis in the library is normalized to be 0 for a gaussian distribution (the expected value for a gaussian distribution without this “normalization” is 3). For MDR1 simulation, the kurtosis (g_2) in each plane for the different LOS can be seen in Figure 3.13. Again, it can be seen that the kurtosis values fluctuate around 0 with some peaks indicating that in this certain plane the distribution of $\mathrm{d}T/\mathrm{d}r$ have a pronounced peak near the mean value obtained in Figure 3.11 (red line), while the negative values correspond to planes with less pronounced peaks.

In order to understand the link between Figure 3.11, Figure 3.12 and Figure 3.13 let us show and example. Taking the red line of the bottom panel from Figure 3.11, we know that this is the mean behaviour of $\mathrm{d}T/\mathrm{d}r$ along the z-axis (i.e. the mean behaviour of the distribution of temperatures in certain xy-planes or z-planes). Taking for example a value of $z = 200\ h^{-1}$Mpc, we will see that the mean value of the distribution of $\mathrm{d}T/\mathrm{d}r$ for this plane $z = 200\ h^{-1}$Mpc is $\langle \mathrm{d}T/\mathrm{d}r \rangle \sim 0\ \mu\mathrm{K}\ h\ \mathrm{Mpc}^{-1}$ with a standard deviation $\sigma \sim 0.0186\ \mu\mathrm{K}\ h\ \mathrm{Mpc}^{-1}$. Then, according to the blue line in Figure 3.12 which gives the skewness for the z-planes, we can see that for $z = 200\ h^{-1}$Mpc we have $b_1 \sim -0.1$, so the distribution of values for $\mathrm{d}T/\mathrm{d}r$ in this particular plane is skewed to the negative values, but still nearly symmetric. Finally, the blue line of Figure 3.13 that gives the kurtosis for the z-planes indicates us that for the plane $z = 200\ h^{-1}$Mpc, $g_2 \sim -0.4$, so this distribution is platykurtic, i.e. have thinner tails than a gaussian distribution. So, using those 3 figures we can give a general characterization of the distribution of values for $\mathrm{d}T/\mathrm{d}r$ in a chosen z-plane; this holds for the three integration axis.

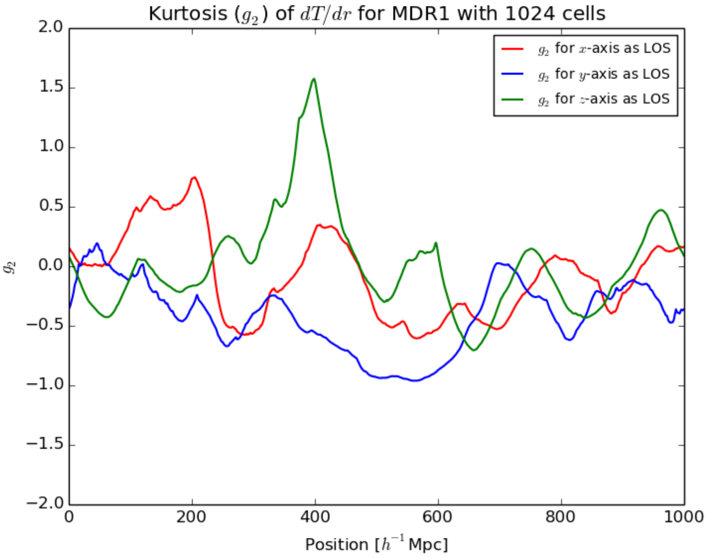

Figure 3.13: Kurtosis for the distribution of $\mathrm{d}T/\mathrm{d}r$ for each plane along the three different LOS used. This was obtained for the MDR1 simulation with 1024 cells per axis in the linear approximation. It can be seen a fluctuation of the kurtosis around 0, which is the expected value for a gaussian distribution (according to the normalized computation of GSL).

3.4.3.2 **Skewness and kurtosis for MDPL simulation**

For the MDPL simulation, we compare each solution (exact solution of Equation 2.30 and the linear approximation of Equation 2.31) for each integration along the different LOS. In Figure 3.14 we can see the skewness for all the LOS in the two regimes. It can be seen how the linear regime has an analogous behaviour as in the case of MDR1 simulation, while the exact solution presents some kind of “noise” but the general behaviour is modulated by the profile found with the linear approximation. Those peaks and valleys that form the pattern of noise are due to the non-linear effects present in the exact solution: the use of the velocity field; furthermore, the high resolution used to compute the $\dot{\Phi}$ field alongside with the non-linear effects produce this noisy pattern. The interpretation of these profiles is analogous as in the case shown in subsubsection 3.4.3.1, and we can also see that, in general, the majority of values of the skewness are in the range $-0.5 < b_1 < 0.5$, indicating a near symmetric distribution of values for $\mathrm{d}T/\mathrm{d}r$. Only few regions has a moderately skewed behaviour, characterized by $0.5 < |b_1| < 1$.

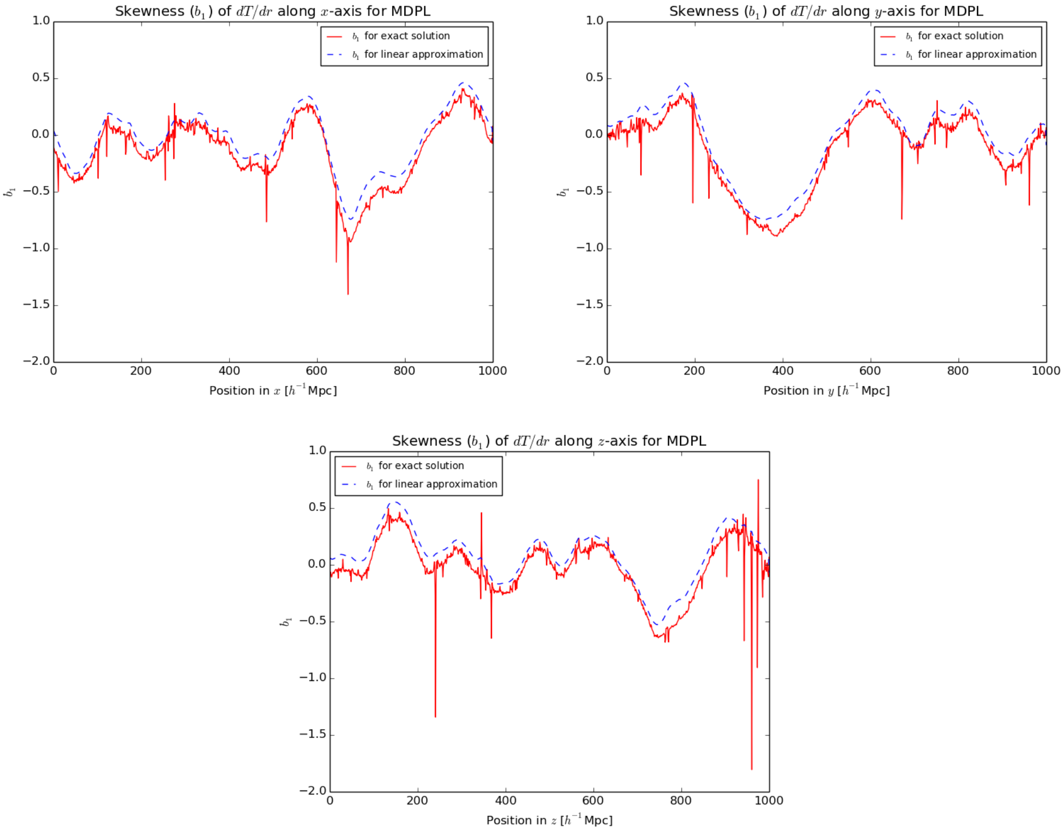

Figure 3.14: Skewness of the distribution of $\mathrm{d}T/\mathrm{d}r$ for each plane along the three different LOS used. This was obtained for the MDPL simulation with 1024 cells per axis in both regimes: the linear approximation and the exact solution. It can be seen a fluctuation of the skewness around 0, which is the expected value for a gaussian distribution.

In the case of the kurtosis, the curves obtained in the exact solution are more anomalous that those obtained for the skewness. Figure 3.15 shows the feature of the kurtosis in both regimes at the left panels, and can be seen how the curve for the exact solution presents a noiser profile than the skewness, with higher peaks, while the linear approximation looks to modulate this noisy curve, as can be seen in the right panels of the same figure where a zoom has been made. In the right panels is evident that the behaviour of the kurtosis in the linear approximation is similar to the kurtosis of MDR1 simulation, and although the curve representing the exact solution is highly noisy, it is indeed modulated by the curve of the linear approximation. The interpretation is similar as the given to Figure 3.13 and from that we can infer that the majority of the regions present values of $g_2 < 0$, indicating that the distribution in those planes has thinner and shorter tails maybe without prominent peaks, while there are special regions with peaks of $g_2 > 0$, i.e., regions where the values of $\mathrm{d}T/\mathrm{d}r$ have a distribution with a fatter and longer tails and maybe with a prominent peak. According to these results, the distribution of $\mathrm{d}T/\mathrm{d}r$ in certain planes is not completely gaussian, which would have been the expected result.

3.5 Summary of results

The results obtained in this chapter can be summarized in the following items:

- **Effects of the Mass-assigment scheme (MAS) on the estimation of the temperature field:** Although in the previous chapter we found that the MAS has an effect on the estimation of the density field, and also on the $\dot{\Phi}$ field in a small degree, the effect on the temperature field can be neglected. When computing the difference $\Delta T_{TSC} - \Delta T_{CIC}$, we found that it is of the order of $10^{-9}\Delta T_{CIC}$ for the exact solution and $10^{-10}\Delta T_{CIC}$ for the linear approximation. With those results we assure that the MAS does not have important contribution to the temperature field because the integration implies a linear combination of positive and negative values of $\dot{\Phi}$, which are compensated to produce the same temperature ranges in spite of the MAS.

- **Effects of the resolution on the estimation of the temperature field:** According to results from subsection 3.2.2 we achieved the characterization of the distribution of temperatures for MDR1 simulation with two resolutions: 512 and 1024 cells per axis. According to this characterization we found that the resolution has a negligible effect on the estimation of the temperature field. The range of temperatures, standard deviation and larger statistical moments are very similar, and although for the resolution of 1024 cells the mean is one order of magnitude smaller than for the resolution of 512 cells, both are basically zero if compared with the wider range of temperatures, which is seven order of magnitudes larger than the means. Then, we found a negligible effect on the ISW estimation due to the resolution used. We support this conclusion with the results obtained in subsection 3.4.1, in which we compute the temperature fluctuation along the line of sight for MDR1 simulation in both resolutions. As explained in subsection 3.4.1 the behaviour of $\mathrm{d}T/\mathrm{d}r$ for the lower resolution of 512 should be considered as a mean behaviour of $\mathrm{d}T/\mathrm{d}r$ for the higher resolution of 1024, which is the result found and shown in Figure 3.8. Due to the structure of those curves, we see that the fluctuations of $\mathrm{d}T/\mathrm{d}r$ for 1024 are very small and around the curve for 512.

- **Effects of the regime of the solution (exact or lineal) on the estimation of the temperature field:** According to results from section 3.1 we found that both, the exact solution and the linear approximation have basically the same contribution at the larger scales. As mentioned in the previous chapter, the exact solution is associated with a local evolution of the smallest structures due to the contribution of the velocity field. This local contribution will allow to understand the temperature fluctuation at smallest scales, i.e. the Rees-Sciama effect. This contribution is suppresed with the use of the linear approximation, but at larger scales we obtain nearly the same behaviour. Taking algo into account the size of the spots, either cold or hot spots, of around $100 - 200$ h^{-1}Mpc of diameter, we conclude that indeed our signal is due to an ISW effect.

  When characterizing the temperature distribution for the exact solution and for the linear approximation, we can see that both distributions are similar, with means very near to zero and statistical moments very alike. This fact support our conclusion about that linear approximation produces a good estimation of large scale fluctuations (ISW effect) if compared with the exact solution, but if we are interested in small scale fluctuations (as Rees-Sciama effect) the use of the exact solution becomes mandatory.

  Those results are supported for a larger cosmological simulation as the MDPL, which are shown in section 3.3. In this case, we found spots with sizes of ~ 200 h^{-1}Mpc and even larger (our ISW signal). For the exact solution, the granularity of the maps is evident and associated with smaller-scales, but for the linear approximation this information is suppresed. The characterization of the temperature distribution for both regimes is similar, but is different if compared with the temperature distribution for the simulation of 400 h^{-1}Mpc. In spite of this fact, the results for the MDPL support our previous conclusions.

- **Effects of the cosmological constant on the estimation of the temperature field:** With the results summarized in Table 3.4, we can see that the mean behaviour of $\overline{\Delta T}$

for MDPL is of the order of 10^{-7} μK, while for MDR1 and the box of 400 h^{-1}Mpc is of the order of 10^{-5} μK, but due to the large range of values of ΔT, this means can be considered as zero, so the value of the density parameter for the cosmological constant will not influence too much the estimation of the temperature fluctuations. This is supported when computed the mean of the temperature fluctuation per unit of length $\overline{\Delta T/\Delta L}$, for which we also see that in the case of MDPL, the value is two orders of magnitude smaller than for the other two simulations, but again the ranges of values for $\Delta T/\Delta L$ are larger enough so we can consider those differences as negligible.

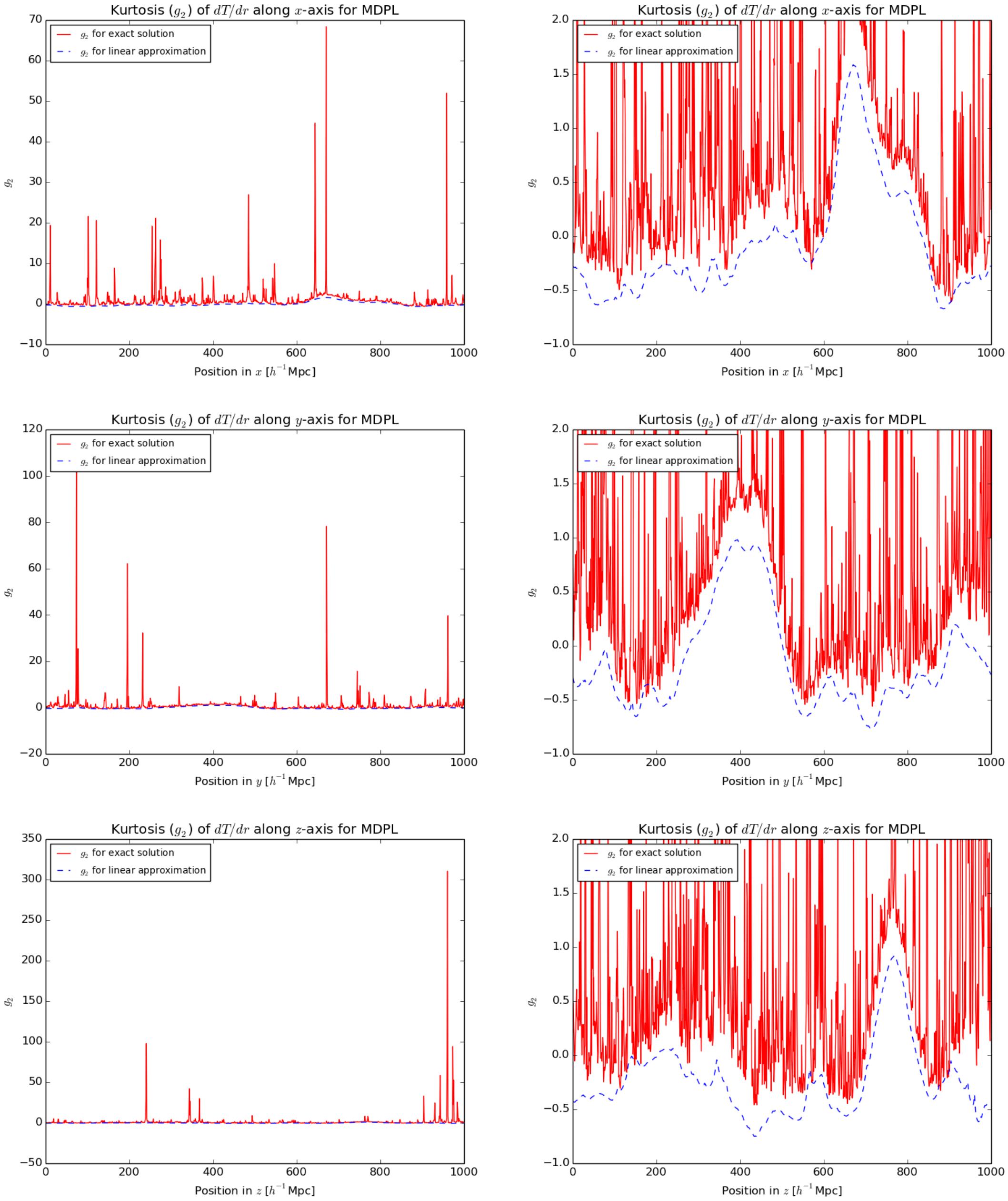

Figure 3.15: Kurtosis for the distribution of $\mathrm{d}T/\mathrm{d}r$ for each plane along the three different LOS used. This was obtained for the MDPL simulation with 1024 cells per axis in the linear approximation. A global view can be seen in the left panels, and a zoom of the same plots is shown in the right panels. Upper panels correspond to integration along x-axis, middle ones to y-axis and bottom ones to z-axis. The noise pattern in the exact solution shows very high peaks, while the linear approximation looks to modulate the noisy curve. The zoom plots at the right reassert the statement about the modulation.

CHAPTER

4

ISW Effect from Observational Data

This chapter comprises the work done with the data from a galaxy redshift survey with the aim to estimate the ISW effect due to the density field of the survey. First, the method with which the observational data was manipulated is described. Then, we integrate along coordinate axes of the box that contains the data in the same way as in the previous chapter. Finally, a radial integration is performed and visualized as Mollweide projections to resemble actual CMB maps to estimate the corresponding cross-correlation function between our ISW-estimation and observations from CMB surveys, alongisde with the angular power spectrum of this correlation. These results are compared with the results obtained from control experiments that come from cosmological simulations in order to characterize the amplitude of the ISW signal associated to observations.

4.1 Halo-Based Method and Estimation of Fields Inferred from Observations

To estimate the ISW signal from the density field of a cosmological simulation, we just need to use a mass assignment scheme, such as the Cloud-in-Cell (CIC) or the Triangular-Shaped-Cloud (TSC) on the synthetic discrete dark-matter particles. When the density field is calculated, it is possible to use the Poisson equation in the Fourier space and then compute the full gravitational potential and its time derivative.

For the observational data the approach may be different, and it should be reminded that one of the possible facts that causes the inconsistencies between the works of different authors, even working with the same data sets, could be the assumptions made in the galaxy bias used to estimate the density field. The galaxy bias pretends to relate the amount of baryonic matter observed with the possible amount of dark matter that host such amount of baryonic matter. In other words, what we can see in the observations is just the baryonic matter that composes the galaxies, but not the amount of underlying dark matter; for this reason, several models for galaxy bias were constructed in order to estimate such relation.

In this work we will implement a different approach, that consist in use of the so-called Halo-Based Methods (HBM) [24], [25]. Such a method has the advantage to be bias-free and does not assume *ad hoc* parameters in the manipulation of the observational data. Before implementing the HBM, it is neccesary to begin with the galaxy distribution from a survey like the Two Micron All-Sky Survey (2MASS). From this survey, haloes of each galaxy are identified through a method described in [25]. In this method, the halo hosting each galaxy group is identified and its characteristics such as virial radius and its mass are estimated. Then, through an iterative method based on the Friends-of-Friends (FoF), the population of haloes is modified. The mass of the haloes is also modified iteratively. When this step is finished, the result is a catalogue of haloes that host the observed galaxies, with their positions, radius an masses.Once the haloes are identified from the galaxy distribution and the corresponding halo catalogue is created, the reconstruction of the density field $\rho(x)$ may be performed, i.e. here begins the implementation of the Halo-Based-Method, as described in [24].

Theoretically, the cosmic mass distribution can be modelled as a smooth continuous function of the coordinates [24]. But this cosmic mass distribution must be inferred from the galaxy distribution, which is a distribution of discrete objects that are considered as tracers of the cosmic mass distribution. The majority of methods used to reconstruct the cosmic mass distribution infer it by smoothing the discrete data of the galaxy distribution on a grid and convolve it with a given smoothing kernel [24]. As those reconstructions are based on the distribution of galaxies, and they may be biased tracers of the cosmic mass distribution, assumptions on the shape and functional dependence of the bias factor are needed [24]. The Halo-Based Reconstruction Method uses the haloes insted of the galaxies to perform the reconstruction procedure, while simultaenously enables the inclusion of environments on the mass distribution around these haloes.

In this method, it is assumed that the cosmic mass is distributed in haloes following a given mass density profile. Here, it is supposed that the density distribution $\eta(r, M)$ in and around a halo of given mass M is a function of the distance r to the centre of the halo and of the halo mass M. Also, spatial coordinates and masses of a set of dark mater haloes are given by a known function $\Psi(\mathbf{r}_i, M_i)$, where $\mathbf{r}_i$ and M_i are the individual coordinates and masses of the ith halo, respectively, i.e. the halo catalogue computed before. Then, the mass density field around the ith halo is defined by the convolution of $\eta(r, M)$ with $\Psi(\mathbf{r}_i, M_i)$ in the following way:

$$\rho_i(\mathbf{r}_i, M_i) = \eta(r, M) \otimes \Psi(\mathbf{r}_i, M_i), \tag{4.1}$$

where the function $\Psi(\mathbf{r}_i, M_i)$ as mentioned before comes from the catalogue of identified haloes. The typical mass distribution in a halo of mass M and its surroundings, $\eta(r, M)$, is computed from cosmological simulations. The total mass distribution $\rho(\mathbf{r})$ arising from a complete set of haloes is defined as:

$$\rho(\mathbf{r}) = \hat{\Sigma}\rho_i(\mathbf{r}_i, M_i). \tag{4.2}$$

For well-isolted haloes, the operator $\hat{\Sigma}$ will represent a summation of the density profiles at the different positions of the haloes. Well-isolated haloes means that their domains do not overlap. The domain of a halo represents the unique region of the universe that is closest to the halo than to any other. But, as the domains of the haloes are going to overlap , the operator $\hat{\Sigma}$ has to be defined as the operation that composes the mass density distribution in and around haloes depending on the extension of the domain of the haloes and the environment where they are located [24].

The final result of the reconstruction of the density field is a set of particles with known position and mass per unit of volume, distributed in a set of haloes in an analogous way as in a cosmological simulation. As the method to create the haloes catalogue, before the application of the Halo-Based Method, makes use of volume-limited samples, the mean comoving density of groups as function of redshift show an almost constant behaviour as shown in Figure 8 in [25]. This allows us to use the estimated comoving density field from 2MASS survey without the need of take into account any redshift incompleteness.

With those methods for the identification of the haloes in a survey like the 2MASS and the reconstruction of the density field, it would be possible to obtain the gravitational potential and its time derivative in order to calculate the ISW signal in such data samples.

4.2 2MASS Reconstruction and 400h^{-1}Mpc box Reconstruction

In order to obtain the haloes catalogue to use into the Halo-Based Method, we use the Final Release of the Two Micron All-Sky Survey (2MASS) [17]. The reconstruction of the density field of 2MASS was made with a halo catalogue of 11523 galaxy groups with virial masses and virial radius estimated according to the method described in [25]. The groups have a distribution of galaxies that varies between 1 and $\sim$ 50 members with masses that varies in the range from $1.0 \times 10^{12.3}$ until $1.0 \times 10^{14.5}$ $h^{-1}M_{\odot}$. The catalogue was built with a volume-limited galaxy sample with an initial set of 14224 galaxies with a limit magnitude in $M_r = -23.0$ and a maximum redshift of $z_{max} = 0.0334$.

Using the Halo-Based Method (HBM) briefly described above, we obtained two reconstructed fields:

- *Reconstruction 1*: The first reconstruction consists in taking the simulation box of $400h^{-1}$Mpc and with the origin of coordinates at the centre of the box, we eliminated the simulation particles that are inside a sphere of radius of $\sim$ 90 h^{-1}Mpc. Then, the halo catalogue corresponding to the positions, radius an masses of the 2MASS galaxy discrete field is introduced into this sphere. Finally, the HBM iss performed to obtain the positions of simulation-like particles to use our Mass-Assignment Schemes (MAS) as with the previous cosmological simulations. The density field obtained after all these processes, which also contains the underlying density field associated to the galaxy groups from 2MASS, is what we called *Reconstruction 1*. Before the application of the MAS, this reconstruction is comprised by 142097062 dark-matter particles with the same masses of the particles of the simulation box of 400 h^{-1}Mpc.

- *Reconstruction 2*: The second reconstruction is comprised by 142910861 dark-matter particles obtained after applying the HBM into the 400 h^{-1}Mpc simulation box itself. From now on, this will be called *Reconstruction 2*. This reconstruction was made as a control reconstruction in order to obtain an ISW control-signal which must resembles the ISW signal obtained in subsection 3.1.1. The aim of this control experiment is first, to see how the HBM may influence the temperature ranges and structure of the ISW estimation and second, to have some control results to compare with those obtained from the first reconstruction, which will allow us to analyse the ISW signal associated with the 2MASS density field.

Figure 4.1 shows the halo catalogue corresponding to the 2MASS survey before the application of the HBM as a Mollweide projection obtained with HealPy[1] (the Python implementation of HealPix[2] tool for pixelation schemes) [11]. As the original 2MASS

---

[1] `http://healpy.readthedocs.io/en/latest/`

[2] `http://healpix.jpl.nasa.gov/`

data set is given in Celestial Equatorial coordinates, which was the coordinate system used to describe the positions of the particles inside the simulation box, we performed a coordinate change to Galactic coordinates, as shown in this figure. As we mentioned before, the 2MASS data set does not contain data in the galactic plane region, so we need to fill this gap and this is done with the synthetic particles of the simulation. This is an important remark because in the analysis we present in this chapter this synthetic particles in the galactic plane will have a contribution to cross-correlation functions and angular power spectra associated to those correlations.

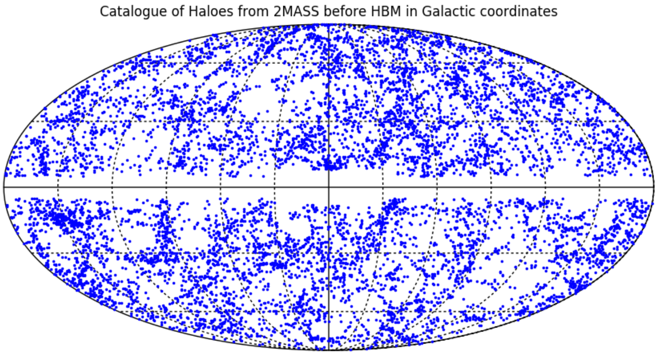

Figure 4.1: Halo catalogue of 2MASS survey particles before the implemetantion of the HBM method. A conversion from Celestial Equatorial to Galactic coordinates is done before performing the Mollweide projection of the sky. This map was obtained with HealPy library.

It is also worth to say that the step of introducing the 2MASS data into a regular geometry was made in order to make Fourier transforms easier and efficiently, without dealing with the geometry of the survey. This will allow us to use for the two reconstructions the same methodology as in cosmological simulations without the need to create new codes. According to this commentaries, it would be relatively easy for us to obtain the density contrast field $\delta(\mathbf{x})$ through a TSC MAS and from it, to obtain the gravitational potential $\Phi(\mathbf{x})$ and its time derivative $\dot{\Phi}(\mathbf{x})$. A final remark about the estimation of $\dot{\Phi}(\mathbf{x})$ field is important, because 2MASS survey does not allow to know the peculiar velocities of the surveyed galaxies, so we must use the linear approximation of Equation 2.31 to estimate the temporal change rate of the gravitational potential.

4.3 ISW along Coordinate Axes

In the same way as with the three cosmological simulations, we performed our methods to compute the $\dot{\Phi}(\mathbf{x})$ field in the linear approximation inside the box for both reconstructions using a grid resolution of 512^3 cells. After those steps, the ISW signal along the three coordinate axes can be computed for the two reconstructions. This is done with the aim to determine the influence of the 2MASS density field from *Reconstruction 1* in the ISW estimation and compare it with a previous known result. Also, this comparison allows us to characterize the mean behaviour of the temperature fluctuation along the line-of-sight $\mathrm{d}T/\mathrm{d}r$ to analyse the influence of the different density fields in the path of the photons.

The left panels of Figure 4.2 show the ISW effect in the box for the *Reconstruction 1* while the right panels show the estimation of the same effect for the *Reconstruction 2*. It is possible to see that structure and range of temperatures for the *Reconstruction 2* are the same as those previously obtained in the linear approximation for the simulation box of $400h^{-1}$ Mpc (as shown in Figure 3.1 for a CIC MAS). This is an obviously expected result, because the second reconstruction is basically the same simulation box but the mass density field is the result of the reconstruction technique; this shows that in principle the reconstruction method provides an appropriate density field to compute the ISW effect. According to this statement, the underlying density field of the *Reconstruction 2* is the same one of the simulation, so the gravitational potential and its time evolution fields are the same. For the result of *Reconstruction 1*, while the range of temperatures is very similar, reaching slightly colder values, the general structure has a notable change at the centre of the box, showing a colder region. This is due to the presence of the 2MASS underlying density field instead of the actual simulation density field. The fact that a cold spot appears at this position implies that the 2MASS density field is not as overdense as the density field of the complete data set of the simulation box.

From those results we can see that working with the *Reconstruction 2* will give a good insight of the expected behaviour of the simulation box. In the next step, we performed an statistical analysis of the temperature fluctuation along the LOS ($\mathrm{d}T/\mathrm{d}r$) to know the mean behaviour of this quantity along the 3 coordinate axes, as done for MDPL and MDR1 simulations (subsection 3.4.2).

The result for *Reconstruction 1* is shown as the red lines of Figure 4.3 while for *Reconstruction 2*, it is shown as the blue lines. Both results have a very similar behaviour, which is expected because the maps of the ISW effect for both reconstructions are very alike and both are due to realizations of the structures in a ΛCDM universe. The differences are more appreciated at the central positions with coordinate values between 100 h^{-1} Mpc and 300 h^{-1} Mpc. This region is the place where the 2MASS density field lies in *Reconstruction 1*, so it is in this region where the density fields are different, so differences in the temperature fluctuations at those places are also expected. The general structure is very similiar and even the standard-deviation region (the red and blue-shadowed zones) show more differences at the center. As the behaviour between both reconstructions is very similar, we conclude that the estimated signal due to the *Reconstruction 1* is in agreement with the theoretical expectation obtained with *Reconstruction 2*. As mentioned above, both density fields are realizations of ΛCDM universes, so even the mean behaviour of the $\mathrm{d}T/\mathrm{d}r$ produced by those density fields is expected to be very similar.

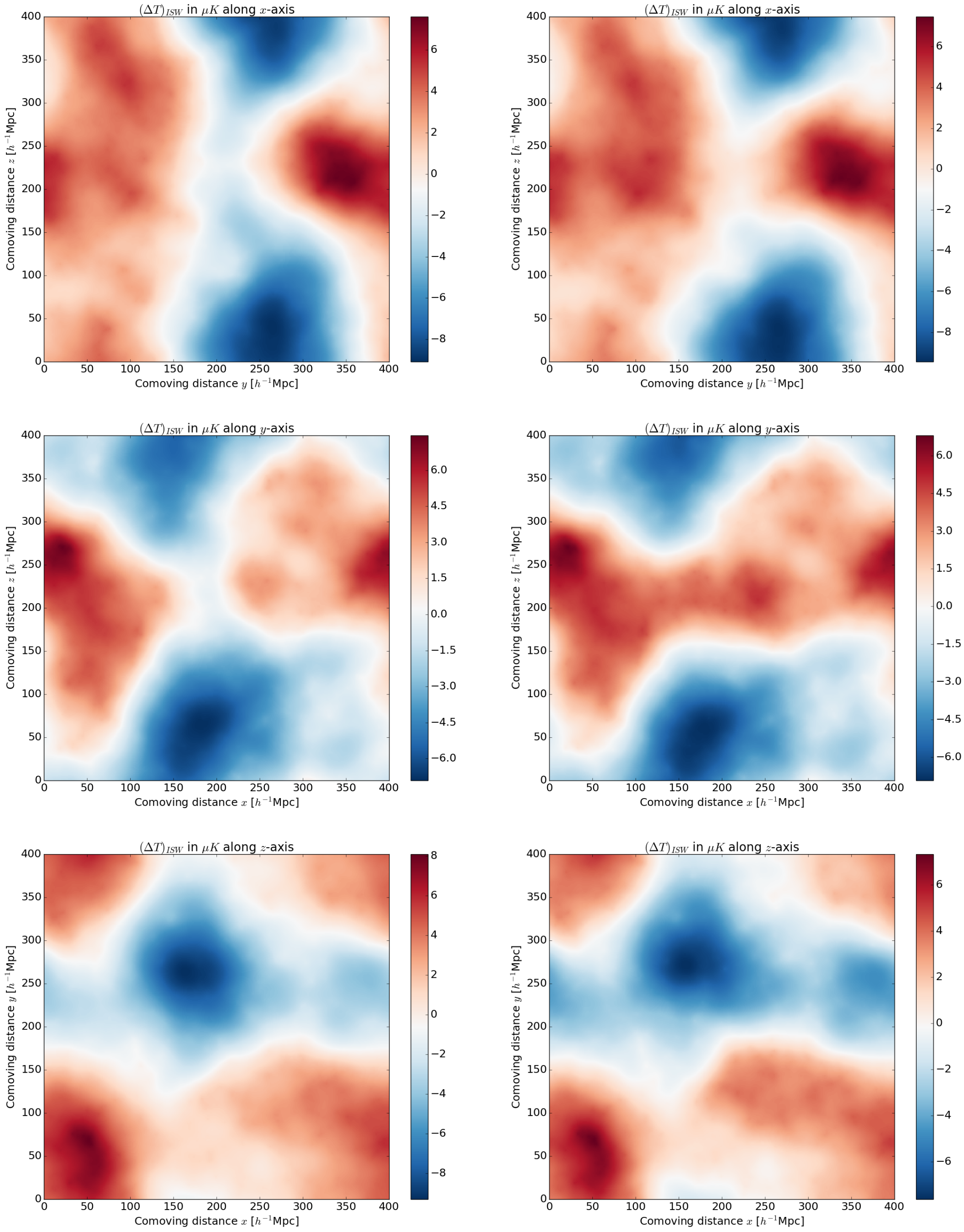

Figure 4.2: ISW effect along the 3 coordinate axes as Lines of Sight (LOS) for the reconstructions. The left panels corresponds to the estimation with the density field of *Reconstruction 1* (2MASS), while the right panels correspond to the signal associated to *Reconstruction 2*. Upper panels corresponds to the integration along the x-axis as LOS; middle ones along y-axis and bottom ones along z-axis as LOS. For *Reconstruction 1* the structure changes at the centre of the box, in which a colder region can be seen. This colder region is due to the presence of the 2MASS density field instead of the true density field of the simulation box.

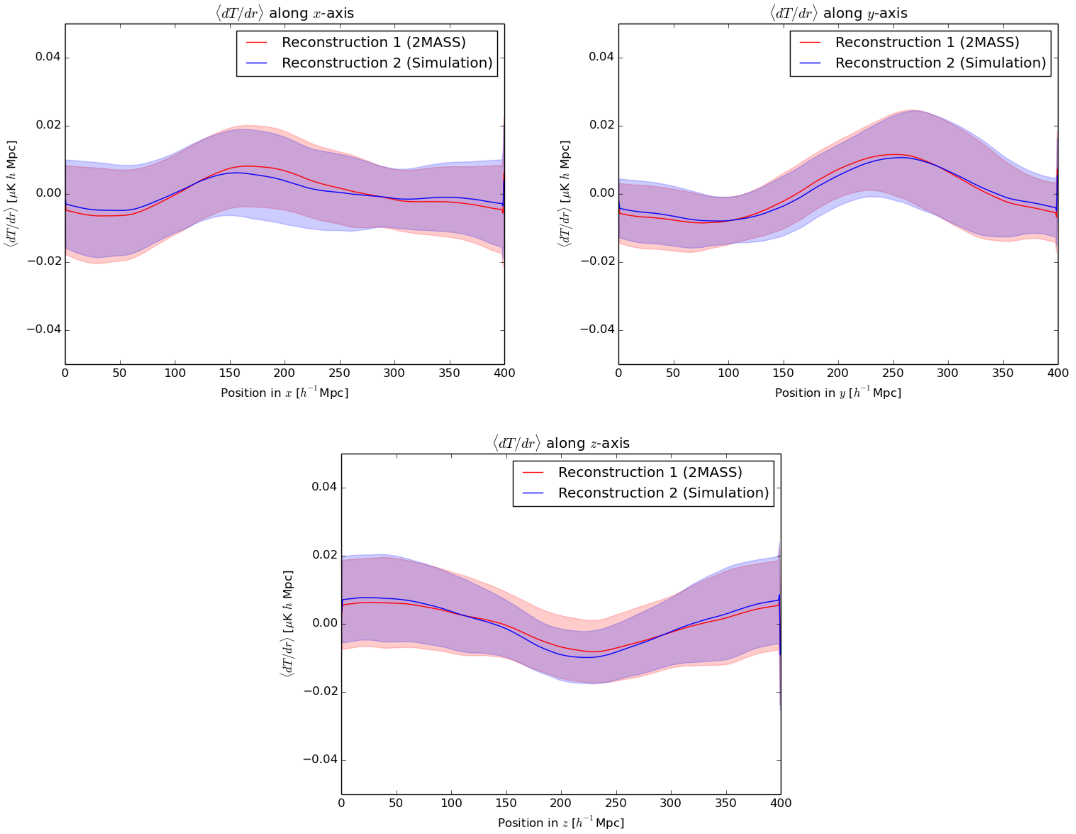

Figure 4.3: Mean temperature fluctuation $\mathrm{d}T/\mathrm{d}r$ along the three coordinate axes as LOS for both reconstructions. Red line is the mean $\mathrm{d}T/\mathrm{d}r$ for *Reconstruction 1* with its corresponding variance (red-shaded region). Blue line and blue-shaded region correspond to the same quantities for *Reconstruction 2*. The slight differences at the central part are due to the different underlying density fields.

4.4 Radial ISW Effect

After the integration along the coordinate axes as a control experiment to evidence if the reconstructions give us consistent results with the cosmological simulations, we estimate the ISW contribution for both reconstructions in a different way.

The procedure used for both reconstructions is described as follows: first, we took the $\dot{\Phi}(\mathbf{x})$ field obtained after applying our Fast-Fourier Transform algorithm in the cubical box and move our coordinate origin to the center of the box. Then, we create 100 million of radial rays with a given radius r_{ray} and angular coordinates $(\theta_{\text{ray}}, \phi_{\text{ray}})$ uniformly distributed on the sphere. So, the complete length of the ray can be know if computing the distance from the origin at the center of the box until the ending cartesian positions $(x_{\text{ray}}, y_{\text{ray}}, z_{\text{ray}})$ asociated with the radius r_{ray} and the angular coordinates $(\theta_{\text{ray}}, \phi_{\text{ray}})$ as a transformation from spherical to cartesian coordinates. Those angles $(\theta_{\text{ray}}, \phi_{\text{ray}})$ will be our declination and right ascension coordinates, respectively.

Then, we use the algorithm from [1] in order to make a ray tracing to know which cells are traversed by each ray and estimate the integral Equation 1.16. For each ray, we apply the mentioned algorithm in the following way: We move the coordinate origin to the center of the box, so the position $(L/2, L/2, L/2)$ will be our new origin $(0, 0, 0)$, being L the length of the box per side. Then, we use the parametric equation of a straight line:

$$(x, y, z) = (x_{0,\text{ray}}, y_{0,\text{ray}}, z_{0,\text{ray}}) + t(x_{\text{ray}}, y_{\text{ray}}, z_{\text{ray}}), \tag{4.3}$$

where $(x_{0,\text{ray}}, y_{0,\text{ray}}, z_{0,\text{ray}}) = (0, 0, 0)$ are coordinates of the vector that points at the initial point of the line and $(x_{\text{ray}}, y_{\text{ray}}, z_{\text{ray}})$ as the coordinates of the vector that points to the final point of the line, as mentioned before. With this equation, we assume for a first iteration that $(x, y, z) = (H, H, H)$, being $H = L/N$ as the size of each cell and N the number of cells per axis. So, we compute three different values for the parameter t, one for each equation corresponding to a cartesian coordinate. From those 3 values (t_x, t_y, t_z), we choose the one with its minimum value $t_{\text{min}} = \text{min}(t_x, t_y, t_z)$, and compute values for the intersection position between the first cell and the ray as

$$(x_f, y_f, z_f) = (0, 0, 0) + t_{\text{min}}(x_{\text{ray}}, y_{\text{ray}}, z_{\text{ray}}). \tag{4.4}$$

From those coordinates (x_f, y_f, z_f), only the coordinate associated with the t_{min} is the one that has a value of H, the other two coordinates must have smaller values. This new positions will give the intersection of the ray with the first cell of the grid and will allow us to compute the traveled distance inside this cell. We then compute Δr_m, which is the distance that the ray travels inside the cell m and store it in an auxiliar array as well as the value of $\dot{\Phi}_m$.

For the next iteration, we use again Equation 4.3 with the values of $(x, y, z) = (iH, jH, kH)$, where (i, j, k) are counters that begin from 1 and increase after each intersection. For example, we begin the first iteration with $(x, y, z) = (H, H, H)$; if the first intersection is with the x-axis, the counter i increases from 1 to 2, while j and k will remain 1, so in this case, for the second iteration we will use the values $(x, y, z) = (2H, H, H)$ in Equation 4.3. This is repeated until we reach the total length of the ray.

Once we have completed the arrays of Δr_m and $\dot{\Phi}_m$, the estimation of the ISW integral is performed as:

$$\Delta T(\hat{\mathbf{n}}) = \frac{2}{c^3}\overline{T}_0 \sum_{m=0}^{N_{\text{traversed}}} \dot{\Phi}_m \Delta r_m a, \tag{4.5}$$

with $N_{\text{traversed}}$ as the total number of cells that the ray traversed from the new origin at $(0, 0, 0)$ until the final position $(x_{\text{ray}}, y_{\text{ray}}, z_{\text{ray}})$.

4.4.1 Radial ΔT differences between reconstructions

In this section, we show the maps of the ISW effect obtained through our ray tracing integration along radial rays. The shown maps were created using HealPy, with the 100 million rays smoothed with a gaussian beam of 1 degree. It also must be taken into account that for all Mollweide projected maps of the ISW, we performed a coordinate change from the Celestial Equatorial coordinates (or right ascension and declination used in the ray tracing) to Galactic coordinates for visualization purposes; the center of the Milky Way must lie at the center of each plot, in the same way as in Figure 4.1. We use two different values for the N_{SIDE} parameter of resolution, $N_{SIDE} = 512$ and $N_{SIDE} = 2048$ in order to also have information about the contribution of the smaller scales, i.e. the Rees-Sciama effect. For clarity and brevity, only the maps with $N_{SIDE} = 2048$ are shown in this section.

For both reconstructions, we performed several integrations in order to make different comparisons between them. First, a complete integration of the rays from the origin until $r_{\text{ray}} = 200\ h^{-1}$Mpc was performed for the two reconstructions; in this case we obtained two ISW contributions, that we will call ΔT^{C}_{Rec1} (for the *Reconstruction 1* which contains the 2MASS density field) and ΔT^{C}_{Rec2} (for the *Reconstruction 2* with the reconstructed density field of the simulation) and we study the difference between both temperatures $\Delta T^{C}_{Rec1} - \Delta T^{C}_{Rec2}$. Here, the superscript C stands for a *complete* integration.

In Figure 4.4 we show the Mollweide projection of 3 maps, the upper one corresponds to ΔT^{C}_{Rec1} for the *Reconstrution 1*, in the middle, the value of ΔT^{C}_{Rec2} for the *Reconstruction 2*, and the bottom plot is the difference $\Delta T^{C}_{Rec1} - \Delta T^{C}_{Rec2}$. This plot shows us a similar structure for both reconstructions, with a big hot spot that serves as a division region for two cold spots. Comparing the temperature ranges from those two panels, we can notice that the temperatures from *Reconstrution 1* tend to be more negative than the temperature from *Reconstrution 2*. The negative temperatures are related with larger underdense regions on *Reconstrution 1*, which was a previous result according to Figure 4.2, where we see that at the center of the box for *Reconstrution 1* the underlying density field was not so overdense as the density field from *Reconstrution 2*.

The bottom plot shows the residual signal after a complete integration for the two reconstructions. In this comparison it can be seen a tendence to negative temperatures, which is due to the high contribution of negative temperatures from *Reconstrution 1*. Other comparisons we show later will give more information. It must be also taken into account that the range of temperatures is slightly lower than the obtained through an integration along the coordinates axis, which is expected because in this radial integral, the light ray is traveling on average half the way it would travel if compared with the integration along the coordinates axes. Indeed, the maximum and minimum temperatures for the radial integrals are nearly half the maximum and minimum values of the integrals along the coordinate axes.

The second case we studied is a complete integration of the *Reconstruction 1* to obtain ΔT^{C}_{Rec1} but the *Reconstrution 2* will be integrated from a radius of 90 h^{-1}Mpc until $r_{\rm ray} = 200$ h^{-1}Mpc, allowing to obtain ΔT^{F}_{Rec2}, where the superscript F stands for integration *from* those 90 h^{-1}Mpc. The difference of these two ISW contributions $\Delta T^{C}_{Rec1} - \Delta T^{F}_{Rec2}$ should give the estimation of the contribution to the ISW effect only due to the 2MASS density field. In Figure 4.5 it is shown the 3 Mollweide projected maps for this second case. The upper panel is the same as in the previous figure, an even the middle panel shows no great difference with the middle panel of the previous figure. Only a slight change in the temperature values indicating colder temperatures and lower hot temperatures, but the general structure is very similar if compared with Figure 4.4. The bottom panel shows more differences with the previous figure, but the two big hot spots and the two big cold spots seen before can be noticed. According to our procedure, this structure of the last panel should be the contribution only from the 2MASS density field, in which we can see a major contribution from voids, represented by the two cold regions. It can also be realized that the range of temperatures is very small even compared with the other radial integrals that we know, have half the temperatures obtained when integrated along the

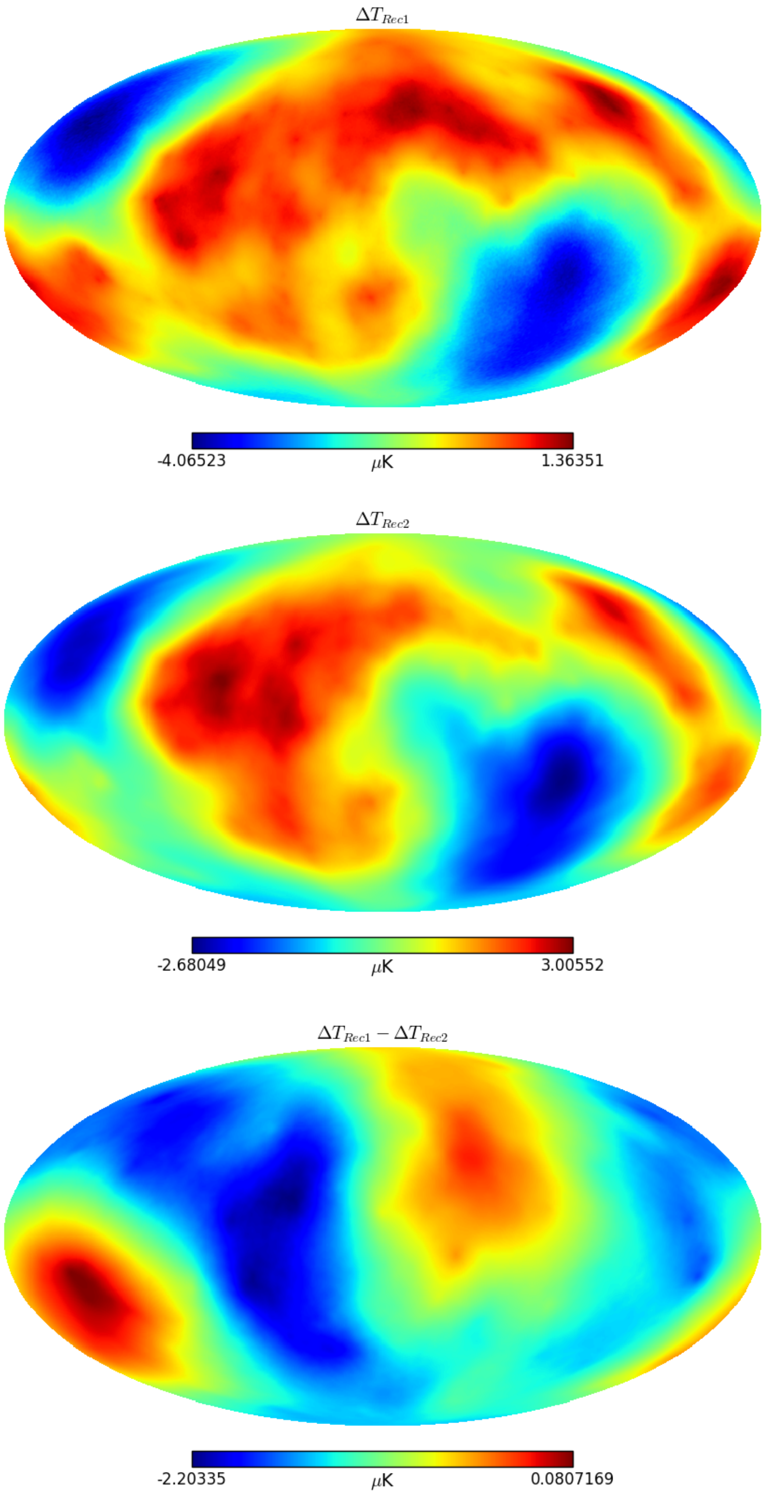

Figure 4.4: Mollweide projected maps obtained with HealPy, after a coordinate changing from Celestial Equatorial coordinates to Galactic coordinates. Upper panel shows ΔT^{C}_{Rec1} for the Reconstrution 1. Middle panel shows ΔT^{C}_{Rec2} for the Reconstrution 2, while the bottom panel corresponds to $\Delta T^{C}_{Rec1} - \Delta T^{C}_{Rec2}$.

axes of the box. This tells us that the contribution to the ISW signal due to our 2MASS sample is small, even tending to colder temperatures, i.e. it has a major contribution from voids than from overdense structures.

In the next case, both reconstructions were integrated from the origin until a radius of 90 h^{-1}Mpc, allowing us to obtain the contributions ΔT^U_{Rec1} and ΔT^U_{Rec2}; where the subscript U stands for integration until 90 h^{-1}Mpc. For *Reconstruction 1*, this integral gives the ISW contribution due only to the 2MASS density field. The resulting maps in Mollweide projection with Galactic coordinates is shown in Figure 4.6. The upper panel shows the actual contribution of the 2MASS density field, which can be compared with the bottom panel of Figure 4.5; from this comparison it can be noticed how both panels are very alike, with almost the same structure and temperature range. The slight differences may come from this fact: the HBM reconstruction method tries to mix the density field from 2MASS with the density field from the simulation, and the TSC mass assignment scheme will also spread the density field from 2MASS into the spatial regions corresponding to the simulation and vice versa. In spite of those little differences, we can assure that the actual structure and temperature range of the 2MASS-produced ISW effect is between those two discussed panels.

In Figure 4.6 it is also shown the contribution of the *Reconstruction 2* integrated until 90 h^{-1}Mpc in the middle panel. Obviously, the structure differs from the upper panel, because both signals are produced by different density fields. The difference between both signals is shown in the bottom panel, and although it has the same two hot regions, the rest of the maps shows signals of negative temperatures from the middle panel, so this remnant shows a mix of the two signals that have no relation between them and no further information can be extracted from it, as expected.

Finally, we estimated the temperature distribution and the statistical properties of those distributions for the two reconstructions integrated from the origin until 90 h^{-1}Mpc. Those distributions can be seen in Figure 4.7 and their statistical properties are summarized in Table 4.1. The aim is to obtain a fair comparison between our ISW estimation and a generic realization of the ISW effect in a ΛCDM universe. As it can be noticed, both distributions are very different, even with a contraty behaviour. While the ISW temperatures due the *Reconstruction 1* has a negative mean and an evident tendence to negative values, the ISW from *Reconstruction 2* has a positive mean with a tendence to positive values. This result is in agreement with the qualitative analysis from Figure 4.2, in which we found that the contribution at the central regions from the left panel of this figure (associated to *Reconstruction 1*) was dominated by underdensities. Those differences are

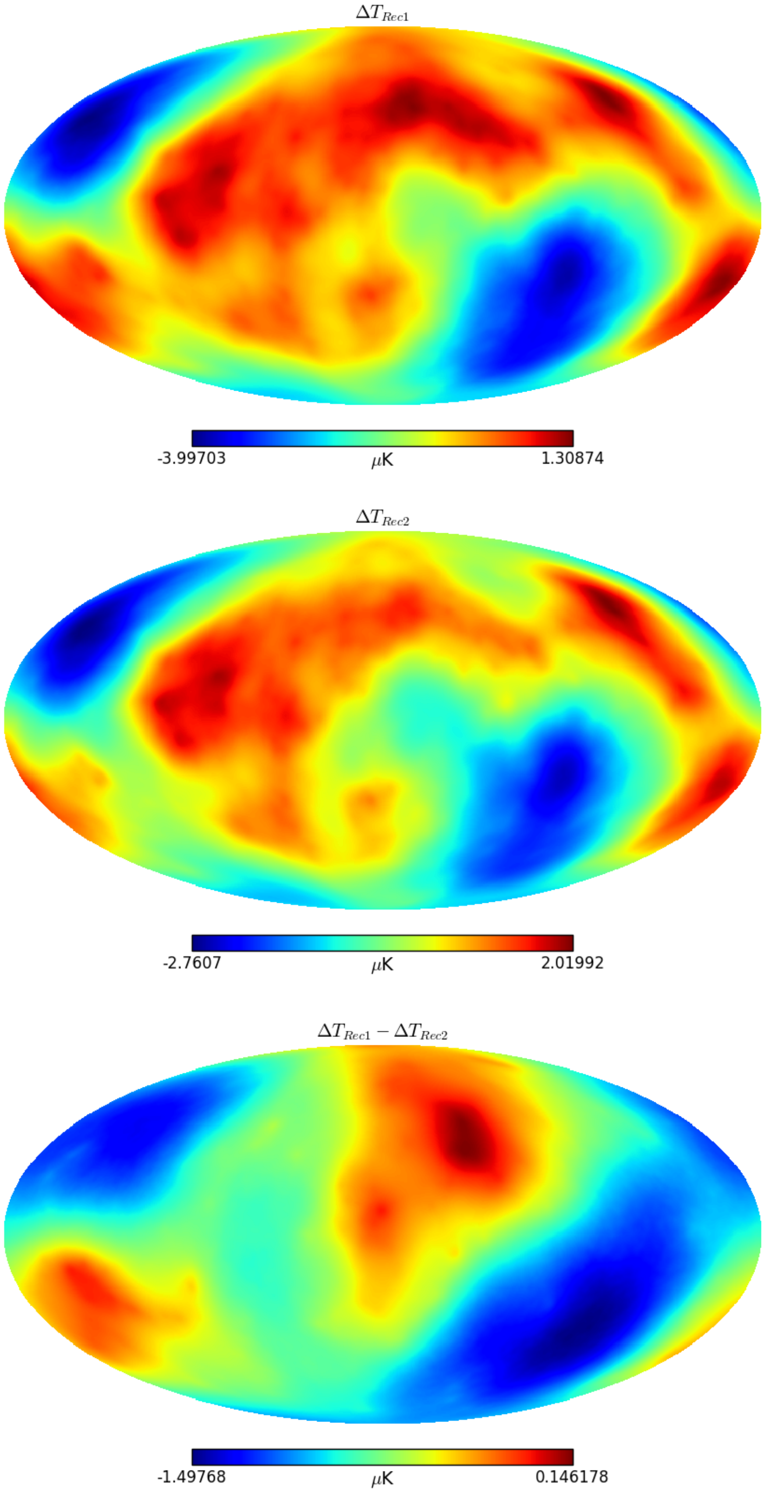

Figure 4.5: Mollweide projected maps obtained with HealPy, after a coordinate changing from Celestial Equatorial coordinates to Galactic coordinates. Upper panel shows ΔT^{C}_{Rec1} for the *Reconstrution 1*. Middle panel shows ΔT^{F}_{Rec2} for the *Reconstrution 2*, while the bottom panel corresponds to $\Delta T^{C}_{Rec1} - \Delta T^{F}_{Rec2}$. The structure of the bottom panel shoul be the contribution to the ISW effect due to the 2MASS density field.

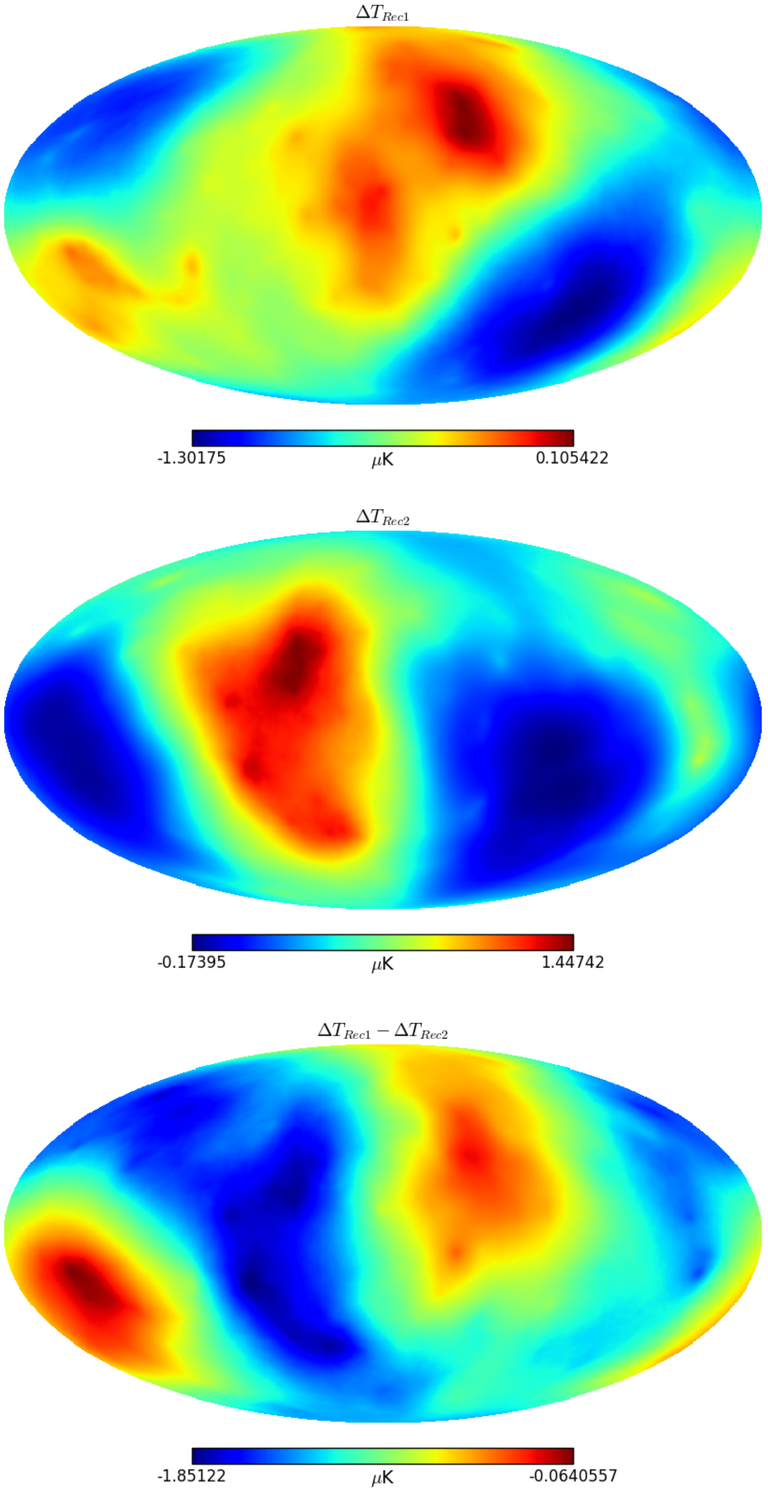

Figure 4.6: Mollweide projected maps obtained with HealPy, after a coordinate changing from Celestial Equatorial coordinates to Galactic coordinates. The upper and middle panels show the ISW contribution from reconstruction 1 and 2, respectively, both integrated from the origin until 90 h^{-1}Mpc; so the upper panel shows the 2MASS-produced ISW effect. A comparison of the upper panel with the bottom panel of Figure 4.5 tells us that the actual contribution of 2MASS to the ISW effect must be between those two maps.

due to the different underlying density fields that give rise to this ISW signal; as both reconstructions are integrated only until 90 h^{-1}Mpc, we can assure that both density fields are completely different. It should be reminded that both density fields are realizations of the structures in ΛCDM universes, and if we take into account the ranges of temperatures obtained in our previous study with cosmological simulations due to the ISW signal, we have that the ranges we found for those reconstructions agree with this ISW signal, but are narrower. Due to the large differences between both distributions and that is not possible to stablish a fair comparison, further analysis like a Kolmogorov-Smirnov test should be done; by time issues this kind of analysis must be done in a future.

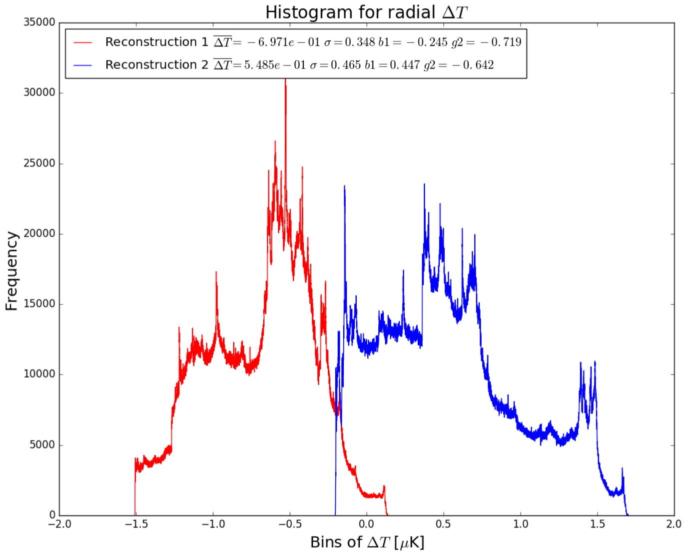

Figure 4.7: Histograms with the temperature distributions from both reconstructions integrated until 90 h^{-1}Mpc. Both distributions have noticeable differences and look to have a contraty behaviour.

Statistical property	Reconstruction 1	Reconstruction 2
$\overline{\Delta T}$ [μK]	-0.6971	0.5485
σ [μK]	0.348	0.465
b_1	-0.245	0.447
g_2	-0.719	-0.642

Table 4.1: Table with the statistical properties of the distribution of temperatures for both reconstructions integrated until 90 h^{-1}Mpc.

4.5 Cross-correlation and Angular power spectrum for 2MASS, WMAP and Planck

After the maps of the radial ISW effect are known, we extract these data from HealPy in order to estimate the 2-dimensional cross-correlation function $w(\theta)$ and the associated angular power spectrum coefficients C_ℓ. It is worth to remember that both quantities are related through a Legendre Transform, according to Equation 1.35 and Equation 1.36, where we will refer to $w(\theta)$ instead of $C(\vartheta)$. In order to compute both quantities, we use the PolSPICE[1] software [34] to obtain both the correlation function, $w(\theta)$, the angular power spectrum of this correlation, C_ℓ, and the covariance matrix $\mathbf{C}$ of the angular power spectrum, from which the diagonal $\mathbf{C}_{\text{diag}}$ gives the variance in the estimation of the C_ℓ, so the error ΔC_ℓ is given by the square root of this variance. The error in $w(\theta)$ is just an error propagation through Equation 1.35.

First, we perform an estimation of the auto-correlation function and the angular power spectrum for two CMB observational maps: for *WMAP* it was used the 9th year Internal Linear Combination (ILC) map, with a HealPy resolution of $N_{SIDE} = 512$; for *Planck* the full-mission Spectral Matching Independent Component Analysis (SMICA) [28] map at the HealPy resolution $N_{SIDE} = 2048$.

After this step, we performed the cross-correlation and the associated angular power spectrum between the ISW map from the *Reconstruction 1* integrated from the origin until the radius 90 h^{-1}Mpc with the WMAP 9th year ILC map at the resolution of $N_{SIDE} = 512$. Finally, the same procedure is done between the same ISW-*Reconstruction 1* map until 90 h^{-1}Mpc and the Planck SMICA map with the resolution of $N_{SIDE} = 2048$. This comparisons have the aim to find a correlation between our ISW estimation from *Reconstruction 1* and the observations, in order to determine if our ISW signal is detected in the observed data sets. In the case of Planck, further information can be extracted related with the Rees-Sciama effect at the smaller scales, as we will show in the next sections.

4.5.1 Auto-correlation and Angular power spectrum for WMAP and Planck

In this subsection we will show the results from the auto-correlation function and the associated angular power spectrum of the data from observations using PolSPICE software. This allows us to know the structure of the angular power spectra from the ob-

---

[1] `http://www2.iap.fr/users/hivon/software/PolSpice/`

servational CMB surveys. Knowing this structure allows to make a comparison with the cross-correlation power spectrum from our ISW-estimated maps to characterize the corresponding contribution due to our estimations and find if they share features with the angular power spectra from observations.

The 9th year WMAP ILC auto-correlation function is shown in Figure 4.8. This figure shows in the left panel the complete auto-correlation function $w(\theta)$ for $0^\circ \leq \theta \leq 180^\circ$ with the x-axis in logarithmic scale. The structure obtained in this plot is the same if compared with Figure 5. from [3] when no logarithmic scale is used. On the other hand, the angular power spectrum associated to this auto-correlation is shown in the right panel of Figure 4.8. In this spectrum only the first acoustic peak can be seen, although not complete. This may be an effect of the resolution used, in which small structures are not resolved. This fact does not affect too much our work, because we are dealing mainly with larger structures, which contribute to the power sepctrum at the small multipoles ℓ.

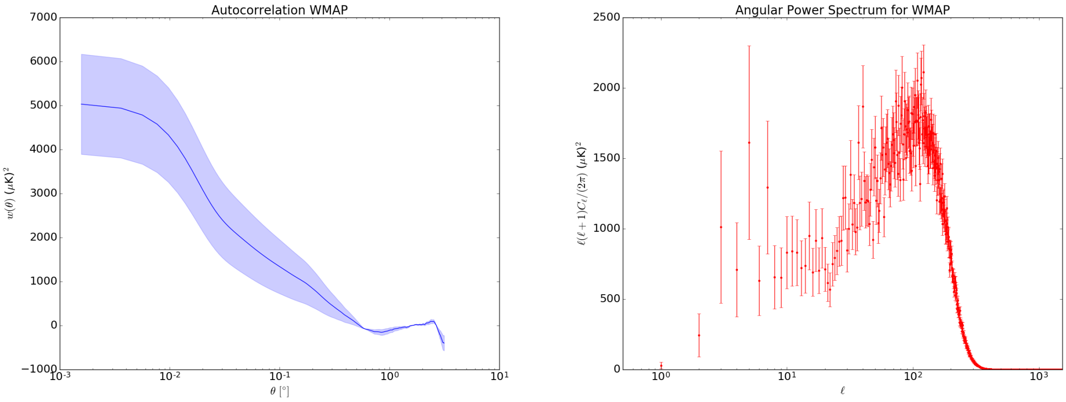

Figure 4.8: Auto-correlation function for the 9th WMAP ILC map. Left panel shows the auto-correlation function $w(\theta)$ for the complete domain $0^\circ \leq \theta \leq 180^\circ$. Right panel shows the Angular Power Spectrum for the 9th year WMAP ILC map. Only a contribution to the first acoustic peak is shown, although not complete, due to the resolution used.

In the case of the full-mission of Planck, the auto-correlation function is shown in the left panel of Figure 4.9. Here, there is a larger autocorrelation for small degrees than in WMAP, but the general structure, is almost the same, and taking into account that the variance (blue shaded region) is narrower.

The angular power spectrum for the Planck mission obtained with PolSPICE software (right panel of Figure 4.9) shows the complete and expected theoretical structure. It is possible to see how at large multipoles ℓ (i.e. the smallest structures) the baryonic acoustic oscillations are present with a small variance. At the small multipoles (largest

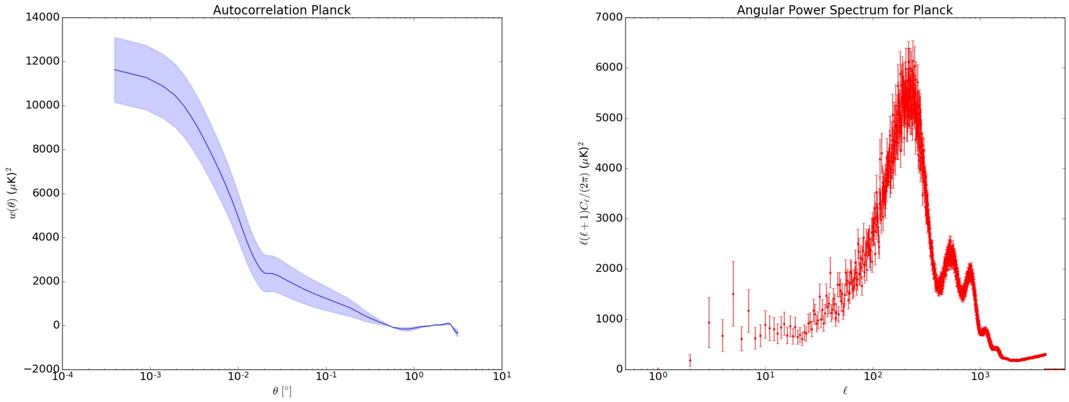

Figure 4.9: Autocorrelation function for Planck in the left panel. The structure is very similar to the obtained for WMAP, except that the autocorrelation takes higher values at small degrees for Planck. Also, the variance (blue-shaded) is narrower than for WMAP. Right panel shows the Angular Power Spectrum for Planck mission. Due to a higher HealPy resolution ($N_{SIDE} = 2048$), the smallest scales are very well described, showing the expected acoustic peaks.

scales) the variance increases significatively, in the same way as in Figure 4.8 for WMAP. When comparing the region of smaller multipoles ℓ of this figure with the right panel of Figure 4.8, it can be noticed that at small multipoles (largest scales), both figures present almost the same amount of power, with very similar variance (cosmic variance), which is the region in which the late integrated ISW effect should have its contribution.

4.5.2 Auto-correlation and Angular power spectrum for *Reconstruction 1*

Before the analysis between the observational data and our results from the reconstruction with HBM, we have estimated the angular power spectrum and the correlation function of the ISW signal from *Reconstruction 1*. The auto-correlation, shown in the top panel of Figure 4.10, looks to be very constant for all angles between 0° and 180° maintaining the estimated values above zero. In the case of the angular power spectrum, in the bottom panels of Figure 4.10, it can be seen that the smallest multipoles $\ell \leq 3$ have the largest variances, but for $\ell > 3$, the power spectrum drops to very low values, even below 0.01 $(\mu K)^2$. In the right panel there is a zoom of the low-multipoles regions in which can be noticed that in spite of the larger variances values, there is a contribution to the temperaure fluctuation on the largest scales. Although this signal is very small, we can assure that we have found the corresponding contribution due to the ISW effect.

For $\ell > 10^3$ the power rises again, achiving values of around $0.1\ (\mu K)^2$, but continues to be a small contribution. As this large multipoles correspond to the smallest of the structures, this rising values are associated to the temperature fluctuation due to a Rees-Sciama effect. In other words, in our 2MASS density field we also have found a perturbation on the temperatures that may be due to the Rees-Sciama effect, alongside with the ISW effect.

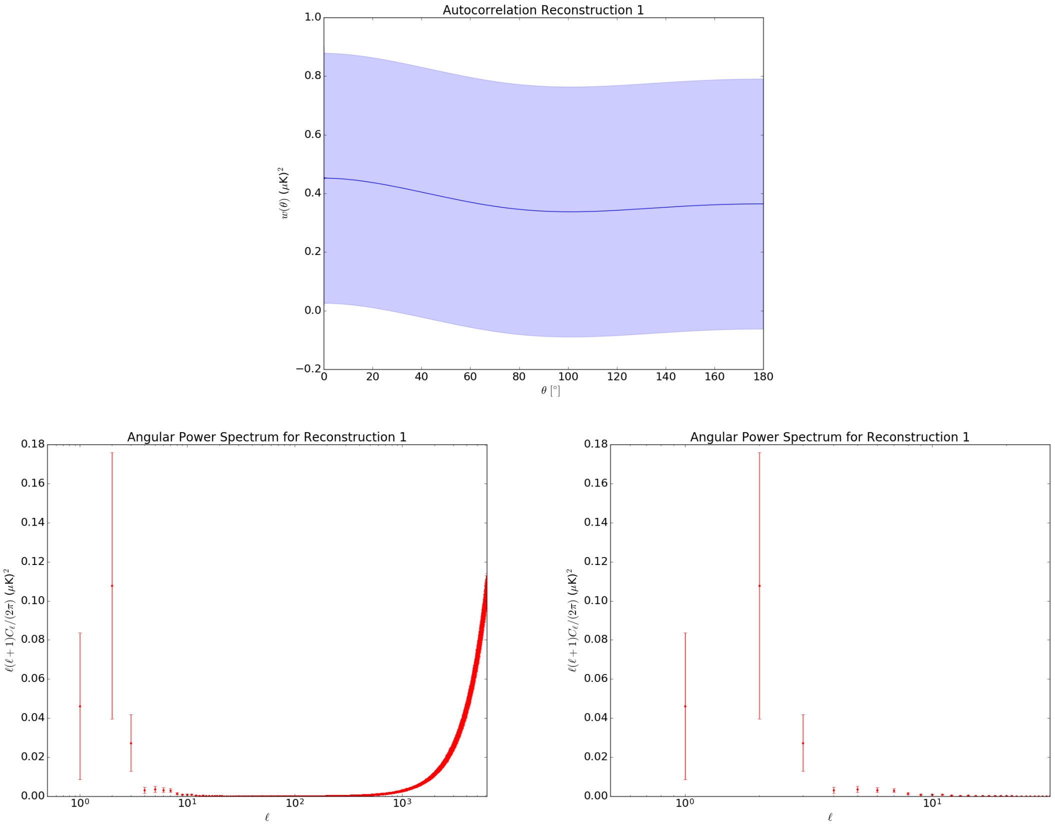

Figure 4.10: Top panel: Auto-correlation function of our estimation of ISW effect from *Reconstruction 1*. A nearly constant behaviour can be noted throughout all the angles between 0° and 180°. In the bottom panels, the angular power spectrum of our estimation of ISW effect from *Reconstruction 1*. Multipoles $\ell \leq 3$ have the highest variances, but for $\ell > 3$, the values drop to very low values, even below $0.01\ (\mu K)^2$, rising again for $\ell > 10^3$. We can notice the contribution of both, the ISW effect in the largest scales, and the temperature fluctuation due to the Rees-Sciama effect at to smallest scales.

4.5.3 Cross-correlation and Angular power spectrum between WMAP and ISW from *Reconstruction 1*

Then, we performed the cross-correlation between the 9th WMAP ILC map and the ISW map obtained from *Reconstruction 1* integrated within the radius of $90\ h^{-1}$Mpc, as mentioned in subsection 4.4.1. Two cross-correlations were performed, the first one using the complete maps; in the second estimation we take both maps, WMAP and the ISW from the *Reconstruction 1*, and make the temperatures in the range $|b| \lesssim 10^{\circ}$ equal to zero, so the will not have any contribution to the power spectrum from the galactic disk. Indeed, it should be reminded that *Reconstruction 1* contains at the region corresponding to the galactic plane a false signal due to the density field from the simulation. These regions must be also omitted in this analysis in order to obtain a more accurate measurement of the quantities of our interest.

For the first case, in which we take into account the complete map that includes the non-actual signal from the galactic plane, the cross-correlation function is shown in the left panel of Figure 4.11. This cross-correlation differs too much from the previously obtained from the observational data; indeed the estimated values are below zero. Even the variance region tells us that the estimation could reach negative values, so it looks like there is no correlation between our ISW map and the WMAP signal. This result is very much in disagreement with the results shown in Figure 7 from [13], where it can be seen that their estimated values for the ISW auto-correlation are above zero. On the other hand, the angular power spectrum (left panel of Figure 4.12) shows negative values at the smallest multipoles, which also suffers from cosmic variance. For $\ell \geq 4$ the values of the power spectrum of the correlation takes positive values and a small contribution to the ISW auto-power spectrum can be seen, but fluctuates around zero and decreases so rapidly, so for $\ell \gtrsim 30$ the power is completely null. Again, comparing with the ISW auto-power spectrum from [13] in their Figure 7, they obtain nearly to zero values for $\ell \sim 100$, and for $\ell \leq 30$ their contribution is of the order of $\sim 30\ (\mu\mathrm{K})^2$. Taking into account the great amount of variance for those low multipoles, our auto-power spectrum can be neglected and considered only part of this variance.

From those two results, our conclusion is that the 2MASS density field used in this work is a small survey with not enough depth to obtain a non-negligible contribution to the late integrated ISW effect. Further, this survey comprises only a local region, so the largest structures can not be complete surveyed. This conclusion will be supported by the results of the cross-correlation function and the angular power spectrum between the same ISW-estimated temperature from *Reconstruction 1* and Planck, shown in subsection 4.5.4.

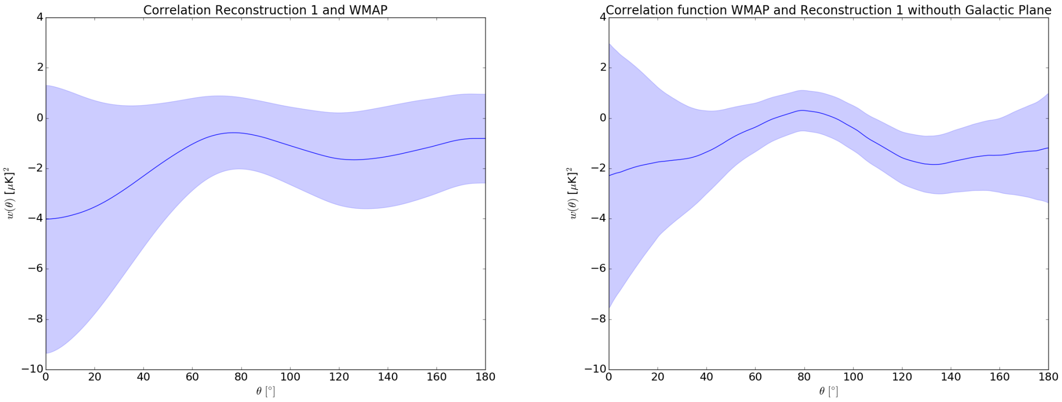

Figure 4.11: Left panel: Cross-correlation function between the ISW map from the *Reconstruction 1* and WMAP. As the estimated values are below zero, it seems that no correlation between those two data sets can be obtained. In the right panel, it is shown the cross-correlation function between our ISW estimate from *Reconstruction 1* and WMAP, both data sets without galactic plane. Again, due to the negative values obtained, there is no correlation between both data sets.

Now we discuss the second case, in which we omitted the signal for both data sets (WMAP and our ISW estimation) in the region of the galactic plane. The cross-correlation function can be seen in the right panel of Figure 4.11, and again, the estimated values are below zero. Even taking into account that the temperature contribution in the galactic plane is assumed as zero, no direct correlation can be obtained between both data sets. This negative cross-correlation means that hot (cold) spots in our ISW estimation are not related with the hot (cold) spots found in WMAP, but instead of that the relation may be with the cold (hot) spots of WMAP.

Finally, the angular power spectrum, shown in the right panel of Figure 4.12, shows that only the multipole $\ell = 4$ presents a higher value over zero, but with larger variance if compared with the left panel. The rest of the multipoles continue with a similar behaviour, fluctuating around zero, with a very negligible contribution to the corresponding angular scales; although the fluctuation is not suppressed so quickly as before, continuing until $\ell \sim 200$. So, contrary to the work in [13], we could not find any cross-correlation between the ISW signal induced by 2MASS and WMAP survey.

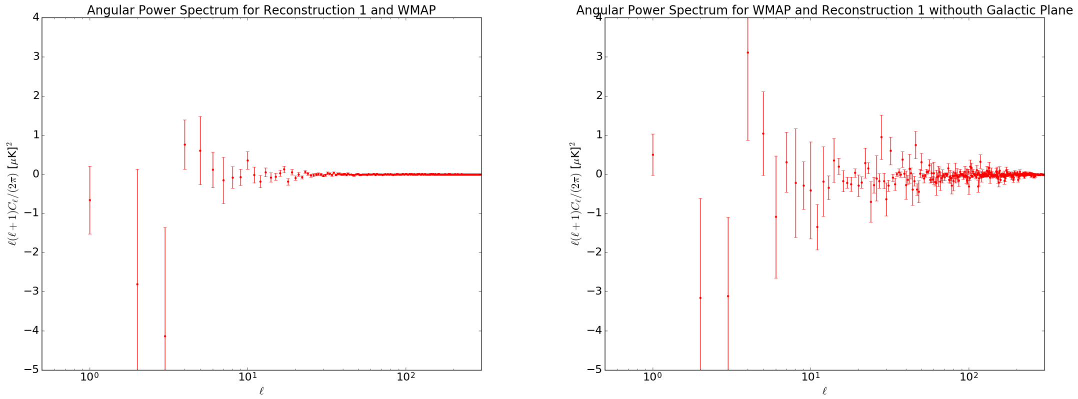

Figure 4.12: In the top panel, the angular power spectrum obtained for the comparison between the ISW map from the *Reconstruction 1* and WMAP. It can be noticed how for $\ell \gtrsim 30$ the power is almost zero. For $\ell < 30$, there is not enough power so it can be considered that our ISW estimate has a negligible contribution to the actual power from WMAP. The right panel shows the angular power spectrum between our ISW estimate from *Reconstruction 1* and WMAP, both data sets without galactic plane. The contribution to the power spectrum continues to fluctuate around zero, making it almost negligible.

4.5.4 Cross-correlation and Angular power spectrum between Planck and ISW from *Reconstruction 1*

As for the 9th WMAP data set, we performed the same comparison to obtain the cross-correlation and the angular power spectrum of the correlation between the Planck data set and our ISW estimated map. These comparisons are performed in the two cases mentioned in the last section: using the whole maps in the data sets and assuming that the temperatures at galactic plane ($|b| \lesssim 10°$) are zero in the two data sets. These comparisons were performed in order to analyse how the resolution may affect our estimation on the ISW effect and even to have a possible estimation on the Rees-Sciama effect. For that last effect which is given at higher multipoles, according to [30] even with data from Planck mission it would not be possible to obtain an estimative of the power contribution in the angular power spectrum due to the Rees-Sciama, because even at those small scales, the variance continues to be high enough to hide any contribution from this non-linear effect. We would like to study if using our method to obtain the ISW contribution through the density field from an Halo-Based Method we could obtain some contribution at small scales or reassert the statement found in [30].

Results of the cross-correlation function for the first case, using the complete maps in both data sets are shown in the left panel of Figure 4.13. Again, most of the values are below zero, and only a slight peak reaching $w(\theta) \sim 0.5\ (\mu K)^2$ for θ between $60°$ and $100°$. For angles $\theta < 30°$, all values fall below zero. Again, it looks like no correlation can be found between our ISW data set and Planck mission, even taking into account the larger resolution of the data sets.

Looking at the corresponding power spectrum of the correlation in the left panel of Figure 4.14, and taking into account that we have not neglected the temperatures at the galactic plane region, it can be noticed that, in general, the behaviour and structure of this spectrum is very similar to Figure 4.12. For Planck, only the contribution for $\ell = 1$ has, strangely, a very small variance, but multipoles $\ell = 2$ and $\ell = 3$ have the higher variances of the samples, as in the spectrum for WMAP. For $\ell \geq 4$ it can be seen that the contribution in the power increases a bit, but fluctuates around zero, decreasing almost complete for $\ell \sim 30$, which is the same behaviour found in WMAP.

In the second case, in which we assume that temperatures in the galactic plane are zero in both data sets, the cross-correlation and the angular power spectrum can be seen in right panels of Figure 4.13 and Figure 4.14, respectively. For the cross-correlation, the peak between $60° < \theta < 100°$ increases almost twice to reach a value very near to $w(\theta) \sim 1\ (\mu K)^2$. The rest of the values, continue to fall below zero, so the same result is found here. In the case of the angular power spectrum without galactic plane, the result

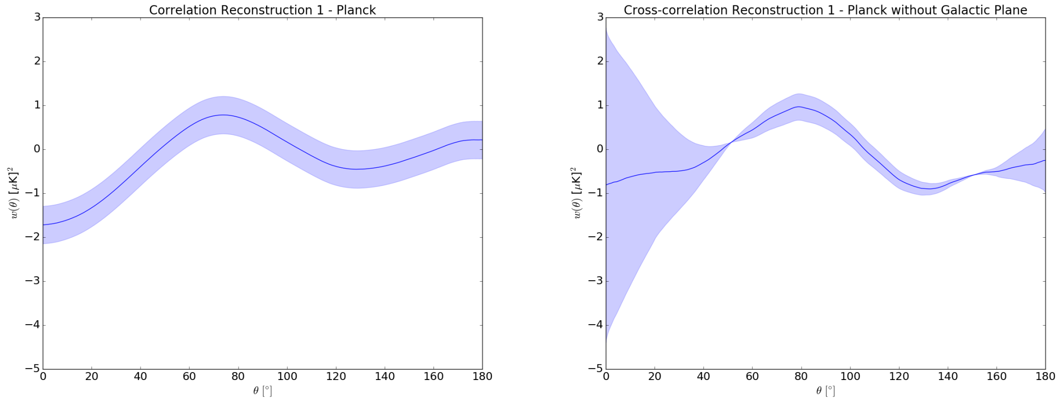

Figure 4.13: Left panel: Cross-correlation function between Planck and our ISW estimate. Most of the values are below zero, but a slight peak can be seen in θ between 60° and 100°. Again, it looks like no correlation can be found between our ISW data set and Planck mission in spite of this slight peak and the resolution used. The right panel shows the cross-correlation function of Planck and our ISW estimation without the contribution to the temperatures in the region of the galactic plane. The same peak for $60^\circ < \theta < 100^\circ$ is notable, but as the rest of the values are below zero, our conclusion about no correlation is maintained.

is basically the same found for WMAP; the only difference is that the variance decreases slightly in Planck, but for small multipoles it continues to be large enough and the power low enough to make the total contribution negligible.

Those results using the Planck mission data, being so similar to those obtained with WMAP reassert our discussed conclusion: using the 2MASS density field alone, it is not possible to have enough large structures that span enough redshift range to obtain a non-negligible ISW contribution. Even, it was also noticed that with Planck data at higher multipoles, the power spectrum lacks from any structure that can allow to estimate a contribution from Rees-Sciama effect. For that reason, we performed a logarithmic bining of our data between $\ell = 10^{2.8}$ until the maximum that PolSPICE allows us with our Planck data ($\ell \sim 6000$) to study the power of Rees-Sciamma at high multipoles. In Figure 4.15 it can be seen how all the bins of multipoles fluctuate around zero taking both positive and negative values, as seen throughout all our previous analysis; in this plot we ommited the error bars by clarity on the figure, but the majority of the symmetrical error bars are below $|0.05|\ (\mu K)^2$. It can be noticed how the power is concentrated inside the range $|\ell(\ell+1)C_\ell/(2\pi)| < 0.05\ (\mu K)^2$, and even below this range, for both cases, using the complete map (upper panel) and assuming as zero the contribution inside the galactic plane (right panel). According to the analysis made in [30] about their Figures 5 and 6, they found an upper limit for the Rees-Sciama power spectrum for $\ell > 10^{2.8}$ of

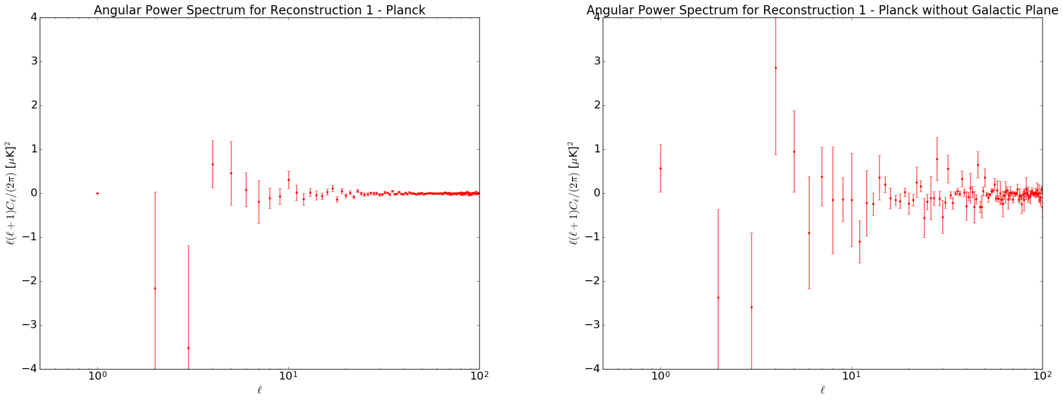

Figure 4.14: Left panel: Angular power spectrum for the correlation between Planck and our ISW estimate. This spectrum has almost the same behaviour as the WMAP spectrum in Figure 4.12, in which a fluctuation around zero is seen for the lowest multipoles, with the highest variances, and decreases rapidly to zero for $\ell > 30$. In the right panel, the angular power spectrum of Planck and our ISW estimation without the contribution to the temperatures in the region of the galactic plane. The structure is almost the same that the obtained for WMAP without galactic plane.

around their $\Delta_T \sim 0.2\mu K$, i.e. $\ell(\ell+1)C_\ell/(2\pi) \sim 0.04\ (\mu K)^2$. A further analysis in this paper, they stated that even with data from Planck mission, the estimation is well below the cosmic variance, so the Rees-Sciama effect is too small to be detected with this probe. From our results, due to the our upper limit very similar to the limite found by [30], we cannot state that we have a detection of the Rees-Sciama effect.

In spite of this last result, the angular power spectrum associated to the auto-correlation for *Reconstruction 1* (Figure 4.10) have shown that indeed there is a contribution on the largest values of ℓ (smallest structures) associated with the imprint of underlying density field from 2MASS, i.e. with our 90 h^{-1}Mpc 2MASS sample we obtained the corresponding Rees-Sciama contribution, although as discussed before, the nowadays available data from CMB surveys do not have enough resolution in order to sample those contributions at smaller scales.

4.6 Summary of results

In this chapter we studied the ISW effect and the Rees-Sciama effect due to the presence of a density field associated with the 2MASS observations. We used a Halo-Based Method [24] in order to reconstruct the dark-matter density field infered from the galaxies catalogue that the 2MASS survey provides (*Reconstruction 1*). Another reconstruction

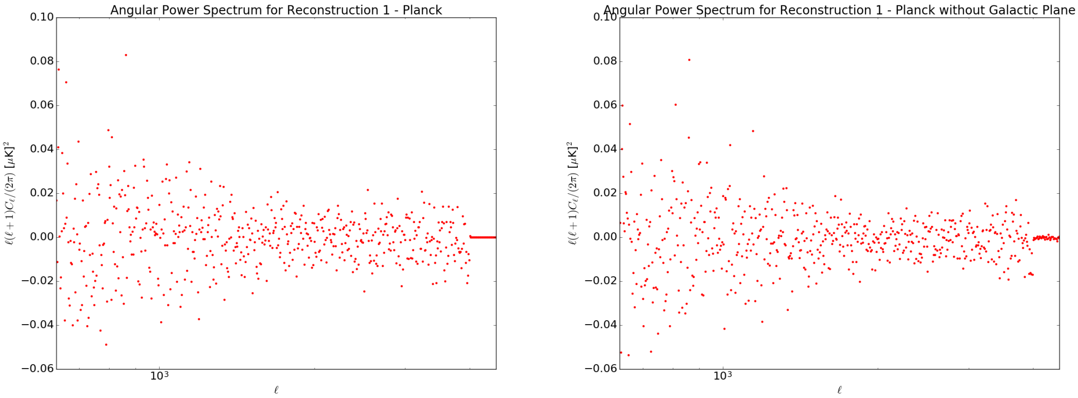

Figure 4.15: Angular power spectrum binned with 700 bins in the range $10^{2.8} \geq \ell \lesssim 6000$ for the comparison between Planck and our ISW estimation. Upper panel corresponds to the complete maps and right panel to the maps without contribution to the temperatures in the region of the galactic plane. In both panels, the power is below $|\ell(\ell+1)C_\ell/(2\pi)| < 0.05\ (\mu K)^2$, so we cannot state for a detection of the Rees-Sciama effect in our analysis.

was performed, but using the synthetic data from the simulation box of $400\ h^{-1}$Mpc (*Reconstruction 2*). With these two reconstructions, we performed two experiments: first, the integration along the three coordinate axes as in the previous chapter; second, radial integrations assuming the observer at the center of the box that will resemble the observed CMB maps using a Mollweide projection with HealPy. Furthermore, with results from the second experiment and using PolSPICE software we are able to study the cross-correlation functions and the associated angular power spectra between the estimated ISW effect induced by 2MASS and CMB surveys. Those power spectra allows to study both, the large scale fluctuations due to the ISW effect and the small scale temperature fluctuations due to the Rees-Sciama effect. The results from this chapter are summarized in the following items:

- **ISW effect from integration along the three coordinate axis:** When perfoming an integration along the 3 coordinate axes using the linear approximation (Equation 2.31) for the solution of $\dot{\Phi}$, we obtained the maps shown in Figure 4.2. The left panel (*Reconstruction 1*) shows in the central regions of the maps a slight different structure compared with the right panel maps. For the first reconstruction although at the center it looks like the ISW effect has a main contribution due to underdense regions, it shows that our reconstruction technique provides an appropriate density field to compute the ISW effect. When studying the temperature fluctuation along the line of sight ($\mathrm{d}T/\mathrm{d}r$) and comparing the results from both reconstructions, we found that *Reconstruction 1* provides a very similar behaviour than the obtained with the *Reconstruction 2* even at the central region, where both density fields are different. This indicates that the temperature fluctuation due to the 2MASS density field is in agreement with the signal expected in ΛCDM universes, which is expected because both density fields are realizations of the structures that may be found in a ΛCDM universe.

- **Radial integration of the reconstructions:** Radial integration is also performed for both reconstrucions; we put the observer at the center of the box and generate 100 million rays distributed in the sphere. The radial integrations are performed in three ways: first, a complete integration from the origin until a radius of 200 h^{-1}Mpc was done for both reconstructions; second, *Reconstruction 1* was integrated completely, but *Reconstruction 2* was integrated from 90 h^{-1}Mpc until 200 h^{-1}Mpc. In this second case, the difference between $\Delta T^C_{Rec1} - \Delta T^F_{Rec2}$ will give the actual contribution of the ISW due to the 2MASS density field. The third integration case was integrated within a radius of 90 h^{-1}Mpc, which in the case of *Reconstruction 1* the signal ΔT^U_{Rec1} will also give the signal due to the 2MASS density field. Indeed we see that the difference $\Delta T^C_{Rec1} - \Delta T^F_{Rec2}$ for the second case and the signal ΔT^U_{Rec1} from the third case are very similar and the actual behaviour of the ISW effect induced by the 2MASS density field must lie between both maps. This contribution tends to colder temperatures which, in agreement with the result discussed in the previous item, indicates that the temperature fluctuation due to 2MASS is dominated by underdense regions.

  Finally, we characterized the temperature distribution of the signals ΔT^U_{Rec1} and ΔT^U_{Rec2}. Both distributions are quite different, showing that for *Reconstruction 1* the tendency is to negative values (as described before) while *Reconstruction 2* has a tendency towards positive values. This behaviour is due to the two different underlying density fields. In spite of these noticeable differences, the range of temperatures are in agreement with the expectation in ΛCDM , but narrower due to the small integration domain. We may conclude that our 2MASS sample with a radius of 90 h^{-1}Mpc is not depth enough to have a good estimative of the ISW effect in our Universe, so a more complete survey should be used in order to have better results.

- **Cross-correlation and angular power spectrum at large-scales (ISW effect):** Once the radial integrations were perfomed, we used this information in order to compute the auto-correlation and angular power spectrum of the temperature field from the *Reconstruction 1* integrated within the radius of $90\ h^{-1}$Mpc, which are shown in Figure 4.10. At the lower multipoles (largest scales) it can be noticed that although the contribution is small and the error bars are very large, we found that due to the 2MASS density field there is indeed a contribution to the temperature fluctuation at larger scales, i.e. the density field from our 2MASS sample has a non-negligible contribution to the ISW effect.

Then we performed the cross-correlation and associated power spectra between the temperature field from our ISW estimation and the temperature fields from the ILC 9th year WMAP survey and the SMICA Planck survey map. In general we found no correlation between the ISW signal from the 2MASS density field and the CMB surveys; this means that there will be no direct relation between our estimation and the observations, i.e. hot (cold) spots in our estimated maps will not correspond spatially with hot (cold) spots in the CMB surveys but maybe with the cold (hot) spots from the survey. This result holds if we avoid the signal from the galactic disk region. Furthermore, those results are supported by the angular power spectra associated with the cross-correlations. For the power spectra, it was found that for the smaller multipoles ($\ell < 4$) have negative values, while for ($\ell \geq 4$) the contribution fluctuates around zero and decreases very rapidly to zero. Then, for larger scales it can be noticed that there is a contribution to the temperature field, but the structure does not resembles the known power spectrum for the observations and it looks like no relation between our ISW estimative and the CMB surveys could be found.

- **Cross-correlation and angular power spectrum at small-scales (Rees-Sciama effect):** When studying the angular power spectrum of the auto-correlation for *Reconstruction 1* integrated within the radius of $90\ h^{-1}$Mpc (Figure 4.10) at the larger multipoles (small scale structures) it can be noticed that the power rises from zero to values of the order of $0.1(\mu\mathrm{K})^2$. This rising is given for $\ell \geq 10^3$, which means that the smallest scales in the 2MASS survey have a non-negligible contribution to the temperature field associated with the Rees-Sciama effect.

  For the power spectrum associated to the cross-correlation between our ISW signal and the WMAP ILC map, we found that for those larger multipoles, the contribution is basically zero due to the resolution used ($N_{SIDE} = 512$). If the galactic plane contribution is neglected, the largest multipoles have a slightly larger contribution, but for a better analysis, the results for Planck are studied. The cross-correlation and the associated angular power spectrum betwen the ISW signal and Planck (using a resolution of $N_{SIDE} = 2048$) offers more information in the larger multipoles (small scales). This contribution is more remarkable when avoiding the galactic disk region. Indeed, the signal we found is of the order of 0.05 $(\mu\text{K})^2$ even with the error bars. According to [30], they found that the Rees-Sciama power should be of around $\sim\ 0.04(\mu\text{K})^2$, but this signal is below the cosmic variance in this small-scales region and even the Planck survey resolution is not enough to measure such a signal. Our results are in agreement with this statement, so in order to measure the actual contribution due to the Rees-Sciama effect we need surveys in the future with enough resolution in such scales. In spite of this results, we can assure that our 2MASS sample contributes both to the large-scale temperature fluctuations (ISW effect) and to the Rees-Sciama effect in the smallest scales.

CHAPTER

5

Effects of the Linear and Exact Solution of $\dot{\Phi}(\mathbf{x})$ on the Estimation of the Angular Power Spectrum

With the aim to quantify the effects of the linear and exact solutions of $\dot{\Phi}(\mathbf{x})$ field in the ISW estimation and its angular power spectrum, we performed a similar comparison of the cross-correlation function and the associated correlation-power spectrum between data from observations (WMAP and Planck missions) and the estimation to the ISW effect using the MDPL density field. For that reason, a radial integration of the $\dot{\Phi}(\mathbf{x})$ field for MDPL was performed in the same way it as done for the Reconstructions from the Halo-Based Method in the last chapter. In this new case, the radial integration was done for both, the linear approximation to $\dot{\Phi}(\mathbf{x})$ due to the linear growth of structures (Equation 2.26) and the exact solution (Equation 2.25) which takes into account the peculiar velocity field.

In the following, we will show for each regime (linear approximation or exact solution) the corresponding cross-correlation and correlation spectrum with WMAP and Planck missions taking into account that the ISW from the integration of $\dot{\Phi}(\mathbf{x})$ for the MDPL simulation is performed until two different depths: first, an integral from the origin at the center of the simulation box until a radius of $100\ h^{-1}$Mpc; for the second case the integral was made from this same origin until a radius of $500\ h^{-1}$Mpc. These two different upper limits in the integral allows us to understand the different contributions to the power spectrum due to the travel of a light ray through more or less structures.

5.1 Angular Power spectrum for MDPL

As a previous analysis, we obtained the angular power spectrum associated with the auto-correlation for the MDPL simulation in both regimes for the solution of $\dot{\Phi}$. In Figure 5.1 the angular power spectra for both radial integrations in the two solution regimes are shown. As expected, the integration until $500\ h^{-1}$Mpc (red and green curves), as is associated with a larger travel of the photons through more structures, the a larger contribution to the power spectrum can be appreciated; for the integration until $100\ h^{-1}$Mpc (blue and cyan curves) have a very little contribution, of the same order of magnitude as the auto-correlation of *Reconstruction 1* in Figure 4.10 at the previous chapter. It can be noticed that the exact solution and linear approximations have basically the same behaviour, but the linear approximation shows a slight smaller contribution to the power spectra than the exact solution. Although it is not shown in the figure, there is also a very hardly noticeable larger contribution in some smaller scales for the exact solution for $500\ h^{-1}$Mpc; while in the linear approximation the power spectrum for $500\ h^{-1}$Mpc decreases to zero more rapidly.

5.2 Cross-correlation and Angular power spectrum in Linear approximation

The case we will study in this section corresponds to the ISW effect from MDPL simulation in the linear approximation with WMAP and Planck missions. The ISW effect induced from MDPL is compared for the two depths presented before, $100\ h^{-1}$Mpc and $500\ h^{-1}$Mpc using the linear approximation to $\dot{\Phi}$.

5.2.1 MDPL simulation integrated until $100\ h^{-1}$Mpc

Performing the radial integration of the $\dot{\Phi}(\mathbf{x})$ field of the MDPL simulation in the linear approximation and finding the correlation spectrum with WMAP (Planck), gives the correlation spectrum shown in the right panel of Figure 5.2. For both cases, WMAP (cyan curve) and Planck (green curve), the correlation spectrum has almost the same behaviour for $\ell > 2$, with the only difference that WMAP presents larger values of variance (not

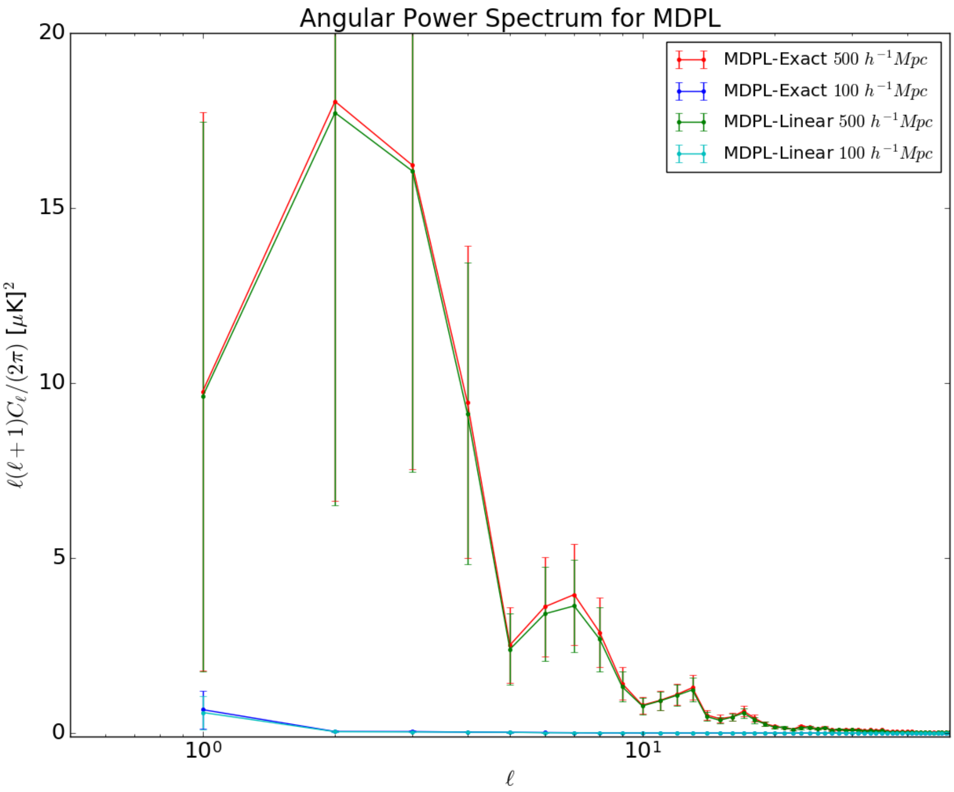

Figure 5.1: Angular power spectrum associated with the auto-correlation function for the MDPL simulation. Blue (cyan) curve is associated with the radial integration until 100 h^{-1}Mpc with the exact (linear) solution. Red (green) curve is associated with the integration until 500 h^{-1}Mpc in the exact (linear) solution of $\dot{\Phi}$.

shown for clarity). If this spectrum is compared with Figure 4.12 or Figure 4.14, it can be noticed that the range of values in the vertical axis are higher for MDPL than for the reconstruction, but still in the same order of magnitude. This difference is due to the slightly larger integration domain in MDPL than in the reconstruction.

In the case of the angular cross-correlation function (left panel in Figure 5.2), although we do not show it for clarity, there is an overlapping between the variances regions for WMAP and Planck. This overlapping is given for angles $\theta < 90°$, while for angles $\theta > 90°$ the differences are considerable but not shown here. At low angles, the variance for WMAP is very high, but contains the estimated value of Planck. It can also be noticed a gap of around $\sim 3(\mu\mathrm{K})^2$ between the estimated values of WMAP and Planck.

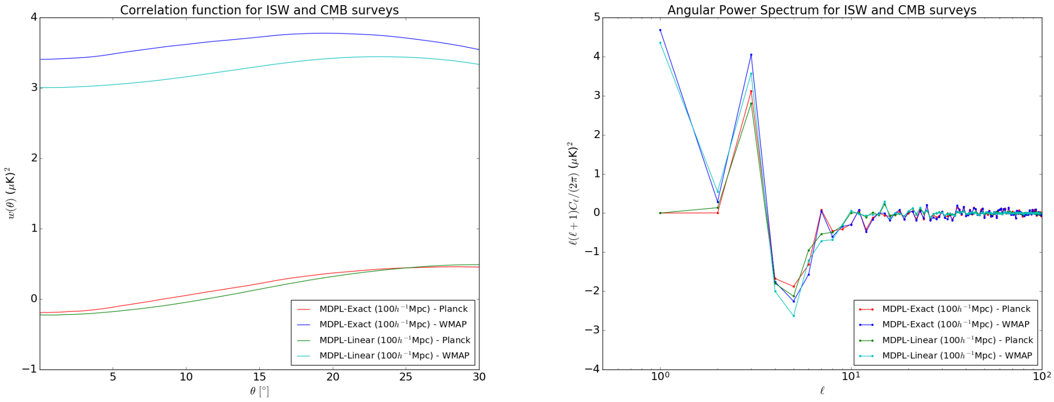

Figure 5.2: Cross-correlation function and correlation-power spectrum for MDPL integrated until $100\ h^{-1}$Mpc with WMAP and Planck. This integration was done for both regimes in the solution of $\dot{\Phi}$. Left panel shows the cross-correlation function with red (green) curve for Planck-MDPL using the exact (linear) solution and the blue (cyan) curve for WMAP-MDPL using the exact (linear) solution. The same color code holds for the correlation spectrum in the right panel. It can be noticed for the power spectrum that while linear approximation decays to zero for $\ell > 30$, the exact solution presents a slight higher contribution, which is associated with the evolution of the smallest structures due to the presence of the velocity field in this exact solution.

5.2.2 MDPL simulation integrated until $500\ h^{-1}$Mpc

For the case of the integration domain between the origin until $500\ h^{-1}$Mpc for MDPL, the angular power spectrum between MDPL and WMAP or Planck is shown in the right panel of Figure 5.3. A notable difference with the linear spectrum shown in Figure 5.2 is the range of values in the y-axis, which is wider in this case, due to a largest integration domain, allowing rays to pass through more structures, and then contributing more to temperature and to the power of the spectrum (the error bars have also a notable increase, but we do not show them by clarity). The estimated values increase up to 10 times the estimated power for the integral until $100\ h^{-1}$Mpc. This is, obviously, an expected behaviour, due to the contribution of even more and more structures to the temperature estimate.

The corresponding cross-correlation is shown the left panel of the same figure. In this case at the smallest degrees, we obtain that the variances present an increase of up to 10 times the estimated variances for the $100\ h^{-1}$Mpc case (variances not shown here), but in this small-angles region the gap continues to be of around $\sim 3(\mu\mathrm{K})^2$. Although we do not show the complete range of values for θ, in this case the overlapping is given up to $\theta \sim 120°$, a region from which the variance region becomes narrower. The fact that the overlapping on the variance region is maintained until an upper angle may be due to a higher contribution of the structures along each ray in a largest path. We expect that for even wider integration domains, the overlapping should be maintained until even higher angles, but we do not have an enough big data set to prove this hypothesis. It is important to notice that the cross-correlation values become negative for the integraion until $500\ h^{-1}$Mpc for both CMB surveys, while for $100\ h^{-1}$Mpc only Planck shows this negative cross-correlation.

5.3 Cross-correlation and Angular power spectrum in the Exact solution

In this section, results correspond to the ISW effect from MDPL simulation obtained through the exact solution and the corresponding cross-correlation and correlation spectrum with the WMAP and Planck surveys. The ISW effect induced from MDPL is compared for the two aformentioned depths of $100\ h^{-1}$Mpc and $500\ h^{-1}$Mpc.

5.3.1 MDPL simulation integrated until $100\ h^{-1}$Mpc

In the same way as in subsection 5.2.1, the radial integral from MDPL was performed until $100\ h^{-1}$Mpc but using the exact solution for $\dot{\Phi}$. This correlation spectrum is shown in the right panel of Figure 5.2 and is very similar to the linear case with only few differences: in the exact solution, the variances (not shown here) of the lowest multipoles are larger, but for multipoles larger than $\ell \sim 30$, for which the linear approximation showed no power, in the exact solution there is a small increase in this power until multipoles $\ell \sim 200$ for WMAP (blue curve), and even until larger multipoles for Planck (red curve), although we do not show this region in the mentioned figures. We may conclude that for multipoles $\ell > 30$, i.e. in the smaller scales, the exact solution plays an important role in the estimation of the contribution of the temperature fluctuations in those scales. As we have mentioned in previous chapters, the linear approximation offers a good estimative of the contribution to the temperature fluctuation at larger scales, with a very similar behaviour than the exact solution, but the information of the smallest scales is erased in the linear approximation, which is evident in the lack of power for smaller multipoles $\ell < 30$.

In the case of the cross-correlation function, at the left panel of Figure 5.2, there is not too much to be said, because the behaviour is basically the same as for the linear approximation. Furthermore, in this analysis the cross-correlation plays no important role because we are interested in the contribution to the temperature fluctuation according to the scales. The cross-correlation function will tell us if there is a direct relationship between the temperature fluctuation due to MDPL and those found in the CMB surveys; such a relation will, obviously, not be found here because we are comparing two different realizations of the CMB in ΛCDM universes, one due to the MDPL contribution and the other the one found in our Universe.

5.3.2 MDPL simulation integrated until $500\ h^{-1}$Mpc

For the radial integration of $\dot{\Phi}(\mathbf{x})$ field in the exact regime until $500\ h^{-1}$Mpc from MDPL simulation and its comparison with the observational surveys, the correlation power spectrum presented in the right panel of Figure 5.3 shows a similar behaviour than the case for linear approximation. Just a slight increase in the power for the largest multipoles can also be noticed, but due to the wider range in the y-axis, this contribution is hardly noticeable. In this case, the difference between solution regimes is not as notable as for the integration until $100\ h^{-1}$Mpc, because the larger integration domain will make that all scales will contribute even more to the power spectrum; in spite of this, there is indeed a slight increase in the power at larger multipoles (small scales) for the exact solution regime.

Finally, the cross-correlation (left panel of Figure 5.3), as in the case of $100\ h^{-1}$Mpc, has almost the same behaviour than in the linear approximation case, in which the departure between both estimated values is given for $\theta > 120°$. Besides, the range at the vertical axis is just a bit larger than in the linear approximation, but with no more noticeable differences.

Although the contribution at low multipoles in the correlation power spectrum looks to be so small, and even using Planck data the Rees-Sciama contribution is below the cosmic variance according to [30], the use of the exact solution for the estimation of the $\dot{\Phi}(\mathbf{x})$ field could be an important tool. As this exact solution to $\dot{\Phi}(\mathbf{x})$ makes use of the peculiar velocities of the haloes, and those velocities are well related to the local evolution of the smallest of the structures, taking into account this small contribution could allow to obtain a better estimation of the Rees-Sciama temperature, which also contributes to the power of the correlation spectrum at larger multipoles. If with future galaxy surveys it is possible to create methods to estimate the peculiar velocities of the galaxies, or the velocities of the host haloes, this information with the help of a future CMB survey with higher resolution than Planck would allow to study in greater detail the Rees-Sciama effect.

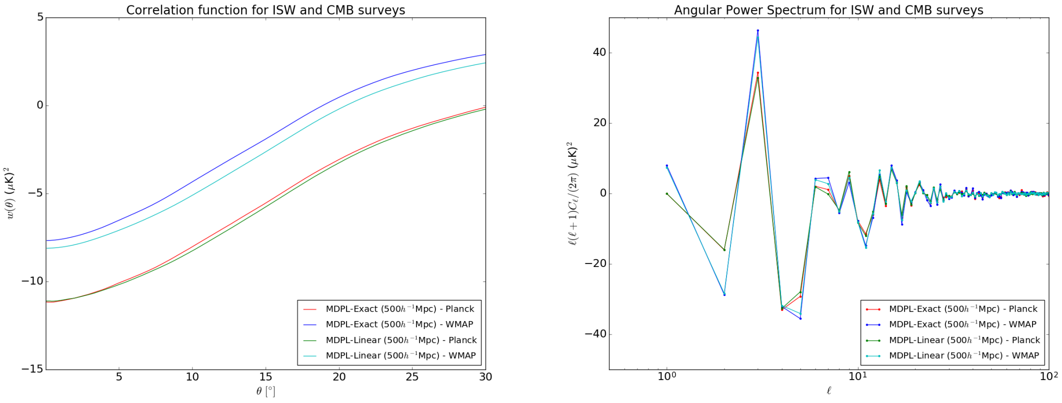

Figure 5.3: Cross-correlation function and correlation-power spectrum for MDPL integrated until $500\ h^{-1}$Mpc with WMAP and Planck. This integration was done for both regimes in the solution of $\dot{\Phi}$. Left panel shows the cross-correlation function with red (green) curve for Planck-MDPL using the exact (linear) solution and the blue (cyan) curve for WMAP-MDPL using the exact (linear) solution. The same color code holds for the correlation spectrum in the right panel. It can be noticed for the power spectrum that while linear approximation decays to zero for $\ell > 30$, the exact solution presents a slight higher contribution, which is associated with the evolution of the smallest structures due to the presence of the velocity field in this exact solution.

CHAPTER

6

Discussion and Conclusions

In this chapter, we discuss the results and conclusions obtained throughout this work. Our first results concerned the effects of the Mass-assigment scheme (MAS) in the estimation of the density field and their influence in the estimation of the gravitational potential and its time derivative, as shown in chapter 2. We see how both MASs give different results for the density field, but for the $\dot{\Phi}$ field those results do not differ as much as for the density field; indeed the distributions are very similar regardless the MAS used, allowing us to conclude that the use of CIC or TSC would give very similar estimations of the underlying fields. Obviously the choice of the TSC rather than the CIC MAS is evident, due to the smoother fields that TSC provides.

Extending the analysis of the effects of the MAS in the estimation of the ISW effect, as shown in chapter 3, we conclude that the influence of the MAS in the computation of the temperature field could almost be neglected. We find no larger differences between the ISW signal from a CIC and the ISW from a TSC. We state that this feature is due to the fact that being the ISW signal an effect integrated along the line of sight, the contributions due to different structures are compensated between them. In other words, although CIC provides more positive (and more negative) values for $\dot{\Phi}$, those contributions are compensated in the same way as if the structures are estimated with a TSC MAS, which gives smoother values; this effect is due to the linear combination of values of $\dot{\Phi}$ when the integration is performed.

Another important result is related with the effects of the resolution. As shown for the MDR1 simulation, the computation of the underlying fields as $\dot{\Phi}$ using different resolutions also have little effect on the estimation of the temperature fluctuation of the ISW effect. We discussed that the distribution of temperatures for two different resolutions are so similar that in the case of a large-scale effect, as the ISW effect, the resolution plays no important role. On the other hand, resolution allows to obtain a more detailed view of the small-scale structures and then of the small-scale effects such as the Rees-Sciama.

For our theoretical expectation of the ISW signal in a ΛCDM universe, the results from chapter 3 obtained only for the 3 cosmological simulations used are summarized in Table 3.4. We obtained an estimated value for the ISW contribution of the order of $|\Delta T_{ISW}^{Sim}| \simeq 7\ \mu$K for the smallest of the simulations (cubical box of $400\ h^{-1}$Mpc), which is translated in a temperature fluctuation per unit of length of $|\Delta T_{ISW}/\Delta L| \sim 0.02\mu$K hMpc^{-1}. For the two MultiDark simulations (cubical boxes of $1000\ h^{-1}$Mpc) the estimated contribution increases until the order of $-40\ \mu$K $< \Delta T_{ISW} < 27\ \mu$K, which is in agreement with previous works [13]. The temperature fluctuation per unit of length for those MultiDark simulations are of the order of $-0.04\ \mu$K hMpc^{-1} $< \Delta T_{ISW}/\Delta L <$ $0.027\ \mu$K hMpc^{-1}, which is in agreement with the result for the previous simulation box. Given these results and the restricted variance regions of the $\langle \mathrm{d}T/\mathrm{d}r \rangle$ plots, we can ensure that we find a good estimation of the ISW effect at least using synthetic data sets, which represent slightly different ΛCDM universes. Then, theoretically in a ΛCDM universe it should be possible to detect this kind of gravitational redshifting in the expected orders of magnitude [13]. We also characterized the behaviour of the mean temperature fluctuation per unit of length $\langle \mathrm{d}T/\mathrm{d}r \rangle$. From this characterization, we found that the distribution of values differs from a gaussian distribution, which is the expectation according to the principles in which the concordance cosmological model is based, but such mean behaviour fluctuates around zero, which is expected because both underdense and overdense regions must contribute to this effect in the same way.

When using a data set of galaxies from a redshift survey as the 2MASS, the approach is somewhat different. First, it is necessary to estimate the density field that hosts the galaxies of the survey. This is done when applying an iterative method to construct the halo catalogue and then, the Halo-Based Method (HBM) (as described in section 4.1) to estimate the underlying density field. Two reconstructions are obtained with the HBM, both inside the simulation box of $400\ h^{-1}$Mpc. In the first reconstruction the central synthetic data is changed by the 2MASS haloes (*Reconstruction 1*) and the second one corresponds to the HBM applied to the complete synthetic data set of the simulation box of $400\ h^{-1}$Mpc (*Reconstruction 2*), as a control experiment. First of all, integrations along the coordinates axes, as done for the 3 cosmological simulations, are perfomed. Also, the integration to find $\langle \mathrm{d}T/\mathrm{d}r \rangle$ along the coordinates axes is used. Results obtained in these part (see Figure 4.3) are consistent with previous results using numerical cosmological simulations (chapter 3). The mean values and the variances in both cases fluctuate very near to zero, and the signal due to the *Reconstruction 1* is very similar to the generic signal from *Reconstruction 2*. This is an expected result because, in spite of the fact that both signals are due to different density fields, those fields are different realizations of the structures in a ΛCDM universe, so the mean behaviour of the temperature fluctuations must be similar. This result allows us to conclude that the HBM provides an appropriate density field, consitent with a ΛCDM universe, in order to compute correctly the ISW temperature fluctuation.

In order to observe the actual contribution of the ISW due to our estimated 2MASS dark-matter density field, we change the integration approach. We move the origin to the center of the simulation box and integrate with 100 million radial rays uniformly distributed in a sphere; this is performed for both reconstructions: the density field with 2MASS infered through HBM and to the synthetic density field of the simulation. We integrated in different domains, so we can extract different ISW signals: the complete synthetic ISW estimation, the spurious signal due to the combination of 2MASS plus the synthetic density field and the contribution due only by 2MASS. The corresponding maps are projected in Galactic coordinates with the help of the pixelation library HealPy. Those results also tell us that the contribution due only to the 2MASS density field is very small; this temperature fluctuation must lie in the range of $-1.5\,\mu$ K $< \Delta T_{ISW}^{2MASS} < 0.15\,\mu$ K. We hypothesized that this small signal is due to the small depth of the 2MASS survey, which only allows to know the local structures. In order to obtain a better estimation, more complete and larger data sets that spans to larger redshift depths must be used, taking into account that the ISW effect is given nearly since $z < 2$.

To finish with the data associated to observations, the auto-correlation and the corresponding angular power spectrum for the *Reconstruction 1* was computed, alongside with the cross-correlation function and the correlation-spectrum between the 2MASS-induced ISW effect and the 9th year WMAP ILC and Planck SMICA maps is studied with PolSPICE software. Those two CMB observational sets allow us to compare both the ISW effect and a possible estimation of the Rees-Sciama effect through an analysis with Planck data. In this case, the cross-correlation functions do not allow to conclude about a direct correlation between our estimated ISW effect and the observational maps; fact that is also evident in the correlation-power spectra because we found that the power takes negative and positive values and fluctuates around zero, decreasing very rapidly. According to those correlation-power spectra, although at small multipoles ℓ there is a contribution to the power spectrum, the variances are to large and the power itself is too small that we cannot conclude about a good detection of the ISW effect in the 2MASS data set related with any of the CMB surveys. In spite of this result, there is an actual contribution to the ISW effect due to the local density field of 2MASS survey, which is found when studying the smaller multipoles of the angular power spectrum of the auto-correlation for *Reconstruction 1*. This contribution is very small due to the depth of the sample used, as discussed before.

When studying the same power spectrum at the smaller multipoles (smaller scales) we found that for the angular power spectrum of the auto-correlation for *Reconstruction 1* the smallest scales have a non-negligible contribution, even comparable in order of magnitude with the contribution at the largest scales. This is associated with a Rees-Sciama signal in our 2MASS sample; so in spite of the small contribution to the power spectrum, with our 2MASS density field we have obtained both contributions, at larger scales the ISW signal and the Rees-Sciama effect for the smallest scales. When studying the cross-correlation and the corresponding power spectrum with Planck, we again found no correlation, but at the larger values of the multipole ℓ we reaffirmed the conclusions from the work of [30]. This means, at larger multipoles in which the Rees-Sciama effect must be presented, even data from Planck survey are not enough to detect such effect, because the signal is still below the cosmic variance at those multipoles.

Finally, an study about the influence of the approach to compute the $\dot{\Phi}(\mathbf{x})$ field into the angular power spectrum was done. According to previous works, in order to compute $\dot{\Phi}(\mathbf{x})$ using Fast-Fourier Transforms, it is possible to use and exact solution in which the peculiar velocity field must be taken into account (see Equation 2.25). This approach has a disadvantage which consists in the fact that in observational surveys it is not easy or even not possible to extract information about the peculiar velocities from galaxies or haloes that host those galaxies. For that reason, an approximation based on the linear growth of structures should be used (Equation 2.26), as introduced by [6]. In order to compare the results given by both approaches and their influences in the angular power spectrum, the $\dot{\Phi}(\mathbf{x})$ field from the MultiDark-Planck (MDPL) was used again, as we have computed it in both approaches. The same radial integration with 100 million random radial rays is applied, and the Mollweide-projected map is obtained. We compared this maps with the WMAP and Planck maps to find the cross-correlations and correlation-power spectrums. Furthermore, for the two approaches in MDPL-$\dot{\Phi}(\mathbf{x})$ field, two integration domains were used: one of $100\ h^{-1}$Mpc, similar to the distance domain of the observational data, and the second of $500\ h^{-1}$Mpc, comprising a total diameter equal to the complete size of the MDPL simulation. From cross-correlation functions, not too much information should be obtained, because it is expected that the ISW maps from MDPL should not share information with the CMB measurements in our Universe. From the correlation-power spectrums, it can be noticed that the power in the spectrum increases for a larger integration domain, which is expected due to a large amount of structures photons have to pass through. Also, although all spectra fluctuate around zero and decreases rapidly to zero, the linear approximation decreases even more rapid than the exact solution spectrum. In the exact solution there is a small contribution to the power at the larger multipoles, which is due to the fact that peculiar velocities are well associated with small structures, as they influence the evolution of the structures at those scales. This fact can have a considerable effect in future estimates of the Rees-Sciama effects, because if future surveys allows to measure the CMB temperatures with even more resolution than Planck, the Rees-Sciama can be estimated well above the cosmic variance. It also imposes a challenge to galaxy surveys in the way that methods to have good estimates of the peculiar velocites of galaxies or their associated dark matter haloes should be developed to help to improve the estimation of the $\dot{\Phi}(\mathbf{x})$ field and maybe, in a future, obtain the actual contribution of the Rees-Sciama effect in the power spectrum.

6.1 Outlook

We expect to use a larger galaxy survey, such as the Sloan Digital Sky Survey, that spans larger redshift-depths to estimate the underlying density field and use the same proposed method in this work to estimate a possible contribution of the late Integrated Sachs-Wolfe effect. We expect that, given the larger the survey, the temperature contribution should be higher, and cross-correlation functions and correlation-power spectra should behave similar to the observed CMB sky. This will allow to give further and stronger conclusions about the ISW effect and its possible detection, constraining even more the values of cosmological parameters and allowing to know even more their influence in the evolution of our Universe.

CHAPTER

7

Appendix

7.1 Fields from MDPL Simulation

In this appendix, we show the maps of the estimated fields for the MultiDark-Planck (MDPL) simulation. Using a CIC MAS with a resolution of 1024 cells per axis, the estimated density contrast field is shown in Figure 7.1. In this figure, it is possible to appreciate the structures that comprise the simulation. After applying our algorithm that makes use of Fast-Fourier Transforms (FFT), the estimated gravitational potential field can be shown in Figure 7.2. It can be noticed how the most negative values of Φ are associated with the most overdense regions of Figure 7.1, while positive values of Φ correspond to underdense or even void regions. The high resolution used in this simulation allows to obtain a detailed view of the smallest scales, even inside the most larger ones.

The estimated time derivative of the gravitational potential $\dot{\Phi}$ estimated using the exact solution (Equation 2.25) is shown in the left panel of Figure 7.3. It can be appreciated that the positive values of $\dot{\Phi}$ correspond to the most negative values of Φ (i.e., overdense regions). This means that overdense regions tend to evolve more rapidly than underdense regions. Those underdense regions are associated with zero or negative values of $\dot{\Phi}$. The estimation of $\dot{\Phi}$ using the approximation based on the linear growth of structures (Equation 2.26) is shown in the right panel of Figure 7.3. The main difference with the estimation with the exact solution is that the linear approximation smooths the structures at the smallest scales, but the global structure at larger scales is very similar in both regimes.

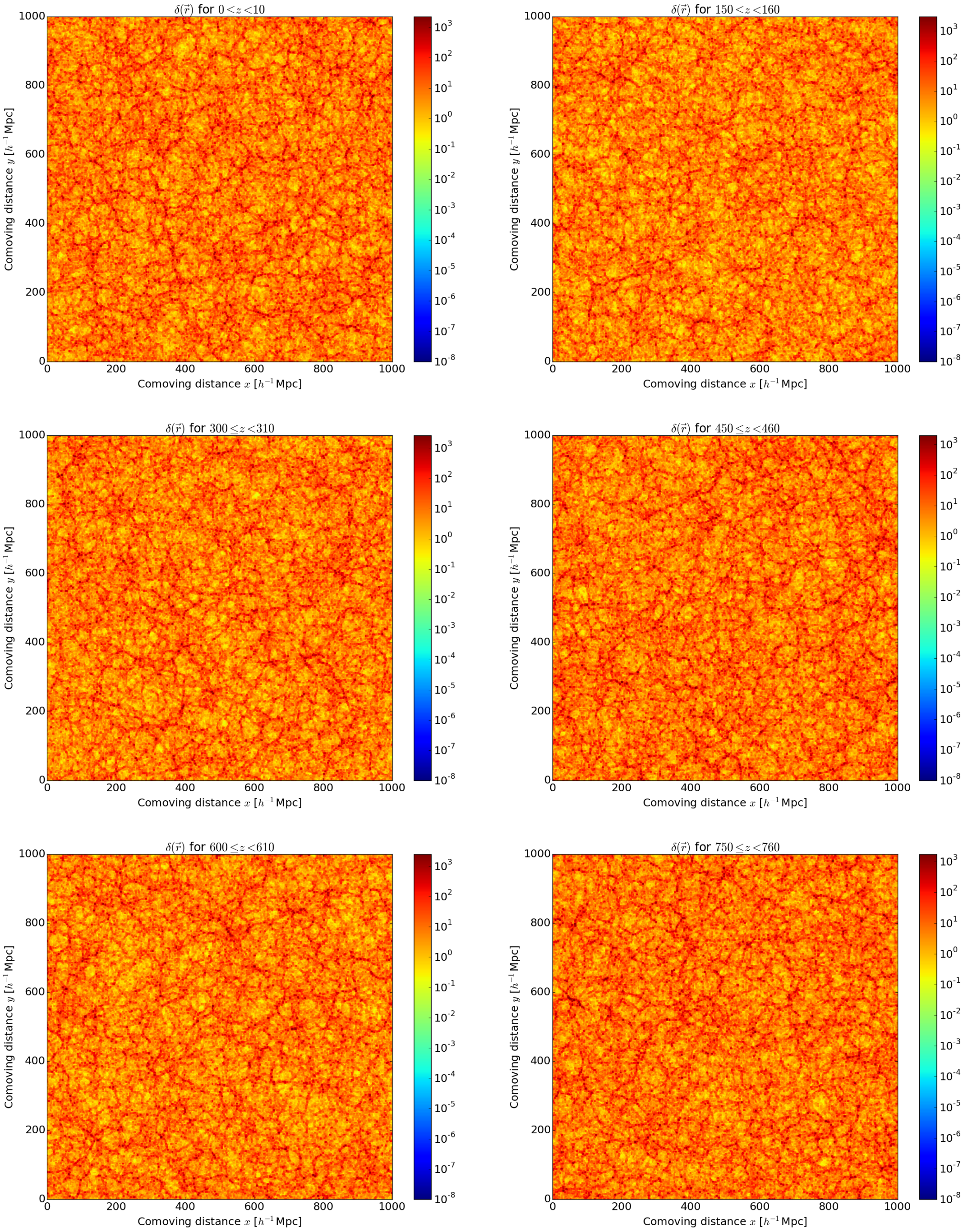

Figure 7.1: Maps of the density field of *MDPL* simulation in logarithmic scale: $\log_{10}\left[\delta(\mathbf{x})+1\right]$. Slices at different depths; from top to bottom and left to right: $0-10\,h^{-1}$ Mpc, $150-160\,h^{-1}$ Mpc, $300-310\,h^{-1}$ Mpc, $450-460\,h^{-1}$ Mpc, $600-610\,h^{-1}$ Mpc and $750-760\,h^{-1}$ Mpc.

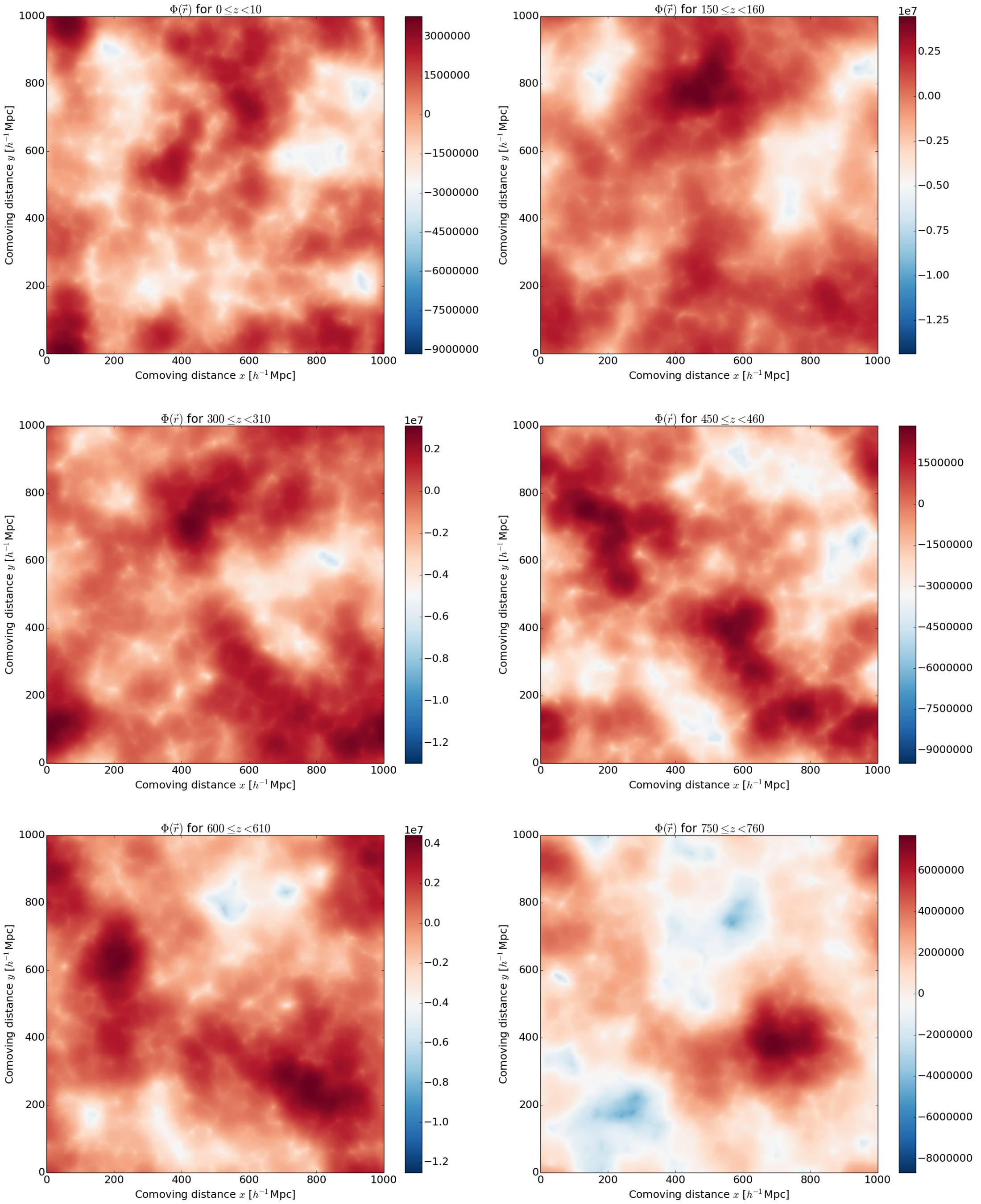

Figure 7.2: Gravitational potential maps for the *MDPL* simulation. From top to bottom and left to right: $0 - 10\, h^{-1}$ Mpc, $150 - 160\, h^{-1}$ Mpc, $300 - 310\, h^{-1}$ Mpc, $450 - 460\, h^{-1}$ Mpc, $600 - 610\, h^{-1}$ Mpc and $750 - 760\, h^{-1}$ Mpc. Units $[\Phi] =$ Internal length^2 Internal time^{-2}.

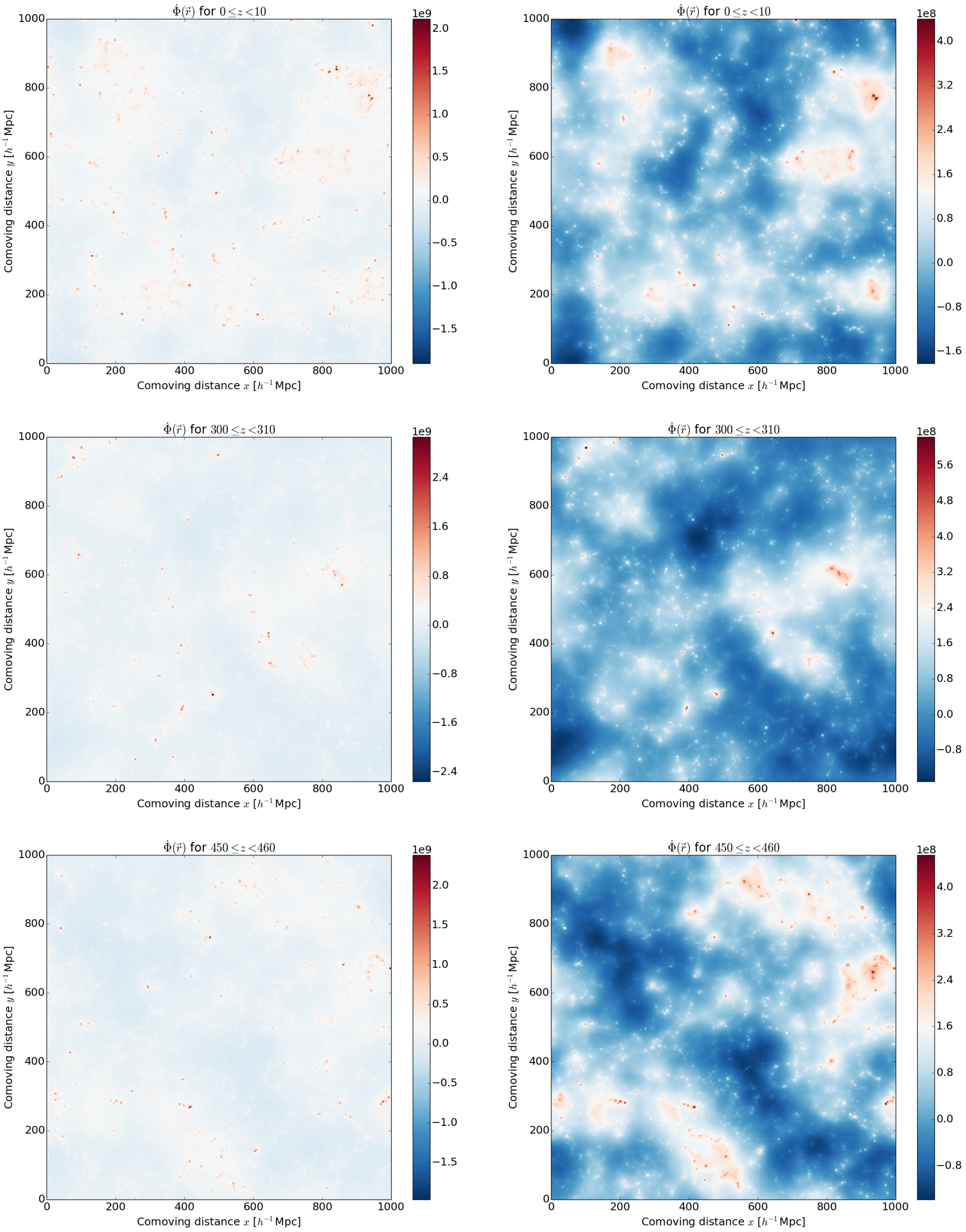

Figure 7.3: Maps of $\dot{\Phi}$ for the *MDPL* simulation. Left panel shows $\dot{\Phi}$ in the exact solution, while the right panel corresponds to the linear approximation. From top to bottom: $0 - 10\,h^{-1}$ Mpc, $300 - 310\,h^{-1}$ Mpc and $450 - 460\,h^{-1}$ Mpc. Units $[\dot{\Phi}] =$ Internal length^2 Internal time^{-3}.

Bibliography

[1] *J. Amanatides and A. Woo, "A Fast Voxel Traversal Algorithm for Ray Tracing"*, Computer Graphics Forum, 1987. Blackwell Publishing Ltd and the Eurographics Association. 112

[2] Cabré Anna, Pablo Fosalba, Enrique Gaztañaga, and Marc Manera. Error analysis in cross-correlation of sky maps: Application to the integrated sachs-wolfe detection. *Monthly Notices of the Royal Astronomical Society*, 381:1347–1368, 2007. ISSN 00358711. 2

[3] C.L. Bennett, R.S. Hill, G. Hinshaw, D. Larson, K.M. Smith, J. Dunkley, B. Gold, M. Halpern, N. Jarosik, A. Kogut, E. Komatsu, M. Limon, S.S. Meyer, M.R. Nolta, N. Odegard, L. Page, D.N. Spergel, G.S. Tucker, J.L. Weiland, E. Wollack, and E.L. Wright. Seven-year Wilkinson Microwave Anisotropy Probe (WMAP) Observations: Are There Cosmic Microwave Background Anomalies? *apjs*, 192:17, February 2011. doi: 10.1088/0067-0049/192/2/17. 121

[4] F. Bernardeau, S. Colombi, E. Gaztañaga, and R. Scoccimarro. Large-scale structure of the Universe and cosmological perturbation theory. *Physics Reports*, 367(1-3): 1–248, 2002. ISSN 03701573. doi: 10.1016/S0370-1573(02)00135-7. 47

[5] Anna Cabré et al. Cross-correlation of WMAP 3rd year data and the SDSS DR4 galaxy survey: new evidence for Dark Energy. *Monthly Notices of the Royal Astronomical Society*, 372:5, 2006. 2

[6] Yan Chuan Cai, Shaun Cole, Adrian Jenkins, and Carlos S. Frenk. Full-sky map of the ISW and Rees-Sciama effect from Gpc simulations. *Monthly Notices of the Royal Astronomical Society*, 407:201–224, 2010. ISSN 00358711. doi: 10.1111/j.1365-2966.2010.16946.x. 11, 12, 44, 62, 89, 93, 146

[7] Bradley W. Carrol and Dale A. Ostlie. *An Introduction to Modern Astrophysics*. Pearson International, second edition, 2007. ISBN 0-321-44284-9. 1, 7, 8, 10, 11, 16

[8] K. Dolag et al. Simulation techniques for cosmological simulations. *Space Science Review*, 134:229–268, 2008. 35

[9] Caroline L. Francis and John A. Peacock. Integrated Sachs-Wolfe measurements with photometric redshift surveys: 2MASS results and future prospects. *Monthly Notices of the Royal Astronomical Society*, 406:2–13, 2010. ISSN 00358711. 3

[10] Tommaso Giannantonio et al. Combined analysis of the integrated sachs-wolfe effect and cosmological implications. *Physical Review D*, 77:1–24, 2008. ISSN 15507998. doi: 10.1103/PhysRevD.77.123520. 2

[11] K.M. Górski, E. Hivon, A.J. Banday, B.D. Wandelt, F.K. Hansen, M. Reinecke, and M. Bartelmann. HEALPix: A Framework for High-Resolution Discretization and Fast Analysis of Data Distributed on the Sphere. *apj*, 622:759–771, April 2005. doi: 10.1086/427976. 106

[12] B. R. Granett, M. C. Nyrinck, and I. Szapudi. An imprint of super-structures on the microwave background due the tue integrated Sachs-Wolfe effect. *Astrophysical Journal*, 683, 2008. 3

[13] Benjamin R. Granett, Mark C. Neyrinck, and István Szapudi. A Map of the Integrated Sachs-Wolfe Signal from Luminous Red Galaxies. *The Astrophysical Journal*, 701:414–422, 2009. iv, 3, 74, 81, 85, 87, 124, 125, 144

[14] R. W. Hockeny and J. W. Eastwood. *Computer simulation using particles*. IOP, 1988. ISBN 0-85274-392-0. 38, 40, 41, 45, 77

[15] Peter Hoyng. *Relativistic Astrophysics and Cosmology*. Springer, New York, first edition, 2006. ISBN 978-1-4020-4521-9. 17, 19

[16] Wayne Hu and Scott Dodelson. Cosmic microwave background anisotropies. *Annual Review of Astronomy and Astrophysics*, 40:171–216, 2002. 2

[17] J.P. Huchra, L.M. Macri, K.L. Masters, T.H. Jarrett, P. Berlind, M. Calkins, A.C. Crook, R. Cutri, P. Erdoğdu, E. Falco, T. George, C.M. Hutcheson, O. Lahav, J. Mader, J.D. Mink, N. Martimbeau, S. Schneider, M. Skrutskie, S. Tokarz, and M. Westover. The 2mass redshift survey—description and data release. 199:26, April 2012. doi: 10.1088/0067-0049/199/2/26. 105

[18] Donghui Jeong. *Cosmology with high ($z > 1$) redshift galaxy surveys*. PhD thesis, University of Texas, 2010. 38, 40, 41, 77

[19] Anatoly Klypin, Gustavo Yepes, Stefan Gottlöber, Francisco Prada, and Steffen Heß. Multidark simulations: The story of dark matter halo concentrations and density profiles. *Monthly Notices of the Royal Astronomical Society*, 457(4):4340–4359, 2016. ISSN 13652966. doi: 10.1093/mnras/stw248. 68

[20] Hannu Kurki-Suonio. *Cosmological Perturbation Theory. Lecture.* University of Helsinki, 2012. 12, 13

[21] Alison L. Coil. Large Scale Structure of the Universe. Arxiv 1202.6633. pages 1–43, 2012. 3

[22] Ofer Lahav, Per B. Lilje, Joel R. Primack, and Martin J. Rees. Dynamical effects of the cosmological constant. *Monthly Notices of the ...*, 251:128–136, 1991. ISSN 0035-8711. 47

[23] H Mo, F van den Bosch, and S D M White. *Galaxy Formation and Evolution.* 2010. ISBN 0521857937. doi: 10.1017/CBO9780511807244. 7, 9, 13, 15, 16, 17, 20, 21, 22, 23, 24, 25, 26, 27, 28

[24] J. C. Muñoz Cuartas, V. Müller, and J. E. Forero-Romero. Halo-based reconstruction of the cosmic mass density field. *Monthly Notices of the Royal Astronomical Society*, 417(2):1303–1317, 2011. ISSN 00358711. doi: 10.1111/j.1365-2966.2011.19344.x. 104, 105, 129

[25] Juan C. Muñoz Cuartas and Volker Müller. Galaxy groups and haloes in the seventh data release of the Sloan Digital Sky Survey. *Monthly Notices of the Royal Astronomical Society*, 423:1583–1595, 2012. ISSN 00358711. doi: 10.1111/j.1365-2966.2012.20981.x. 104, 105, 106

[26] Juan Carlos Muñoz Cuartas. Studying star formation in evolving galaxies through simulations of formation of large scale structure in the universe. Master's thesis, University of Antioquia, 2008. 8, 9

[27] Seshadri Nadathur, Shaun Hotchkiss, and Subir Sarkar. The integrated Sachs-Wolfe imprint of cosmic superstructures: a problem for ΛCDM. *Journal of Cosmology and Astroparticle Physics*, 2012:042, 2012. ISSN 1475-7516. doi: 10.1088/1475-7516/2012/06/042. 2, 12

[28] Planck Collaboration, R. Adam, P.A.R. Ade, N. Aghanim, M. Arnaud, M. Ashdown, J. Aumont, C. Baccigalupi, A.J. Banday, R.B. Barreiro, and et al. Planck 2015 results. IX. Diffuse component separation: CMB maps. 594:A9, September 2016. doi: 10.1051/0004-6361/201525936. 120

[29] Francisco Prada, Anatoly A. Klypin, Antonio J. Cuesta, Juan E. Betancort-Rijo, and Joel Primack. Halo concentrations in the standard LCDM cosmology. 14(April):1–14, 2011. doi: 10.1111/j.1365-2966.2012.21007.x. URL `http://arxiv.org/abs/1104.5130http://dx.doi.org/10.1111/j.1365-2966.2012.21007.x`. 62

[30] N. Puchades, M. J. Fullana, et al. On the rees-sciama effect: maps and statistics. *Monthly Notices of the Royal Astronomical Society*, 370:1849–1858, 2006. 127, 128, 129, 133, 140, 146

[31] R. K. Sachs and A. M. Wolfe. Perturbations of a cosmological model and angular variations of the microwave background. *American Astronomical Society*, 1966. 11

[32] U. Sawangwit et al. Cross-correlating WMAP5 with 1.5 million LRGs: A new test for the ISW effect. *Monthly Notices of the Royal Astronomical Society*, 402: 2228–2244, 2010. ISSN 00358711. 3

[33] R. E. Smith, C. Hérnandez-Monteagudo, and U. Seljak. Impact of scale dependent bias and nonlinear structure growth on the integrated Sachs-Wolfe effect: Angular power spectra. *Physical Review D*, 80, 2009. 11, 42, 43, 44, 45, 62

[34] I. Szapudi, S. Prunet, and S. Colombi. Fast Analysis of Inhomogenous Megapixel Cosmic Microwave Background Maps. *apjl*, 561:L11–L14, November 2001. doi: 10.1086/324312. 120

[35] David Ricardo Valencia-Díaz. The late integrated sachs-wolfe effect in cosmological simulations. Bachelor's thesis, University of Antioquia, 2014. 89